Grounding structures for the EMC-protection of cabling and wiring

Document Version:
Publisher's PDF, also known as Version of Record (includes final page, issue and volume numbers)

Please check the document version of this publication:

• A submitted manuscript is the version of the article upon submission and before peer-review. There can be important differences between the submitted version and the official published version of record. People interested in the research are advised to contact the author for the final version of the publication, or visit the DOI to the publisher's website.
• The final author version and the galley proof are versions of the publication after peer review.
• The final published version features the final layout of the paper including the volume, issue and page numbers.

Link to publication

Download date: 04. Oct. 2023

Grounding structures for the EMC-Protection of cabling and wiring

M.J.A.M. v. Helvoort

GROUNDING STRUCTURES
FOR THE EMC-PROTECTION OF
CABLING AND WIRING

GROUNDING STRUCTURES
FOR THE EMC-PROTECTION OF
CABLING AND WIRING

PROEFSCHRIFT

ter verkrijging van de graad van doctor aan de
Technische Universiteit Eindhoven, op gezag van
de Rector Magnificus, prof.dr. J.H. van Lint,
voor een commissie aangewezen door het College
van Dekanen in het openbaar te verdedigen op
woensdag 29 november 1995 om 16.00 uur

door

MARINUS JOHANNES ADRIANUS MARIA VAN HELVOORT

geboren te 's Hertogenbosch

Dit proefschrift is goedgekeurd door de promotoren:

prof.dr.ir. P.C.T. van der Laan
en
prof.dr. A.G. Tijhuis

copromotor: dr. A.P.J. van Deursen

Contents

Summary

Electronic equipment should not suffer from or cause interference; therefore all equipment has to fulfill certain requirements both on the emission of, and the immunity to, electromagnetic disturbances. From Electromagnetic Compatibility (EMC) studies it is known that disturbances very often reach equipment via the cabling and wiring or are emitted by the cabling and wiring. The goal of the EMC-research, described in this thesis, is to obtain a linear and reciprocal protection of the cabling and wiring. The coupling of electromagnetic disturbances, in both directions, can be described with the transfer impedance.

To measure the transfer impedance of cables two methods are known from the literature: the triaxial method and the wire injection method. When both methods are compared, measurements show a discrepancy. A theoretical analysis leads to an explanation of these differences.

Throughout the thesis measurements are compared to extensive computer calculations of the transfer impedance.

The transfer impedance of cable shields is often too high and additional protection is necessary. Metallic cable trays are often used for mechanical protection. Field calculations and measurements show that they can also play a useful role for EMC-purposes. For non-magnetic trays simple expressions have been found, which describe the transfer impedance as function of geometry, frequency and material properties. In practice these formulas are also useful for shallow steel trays, also when trays are galvanized, as encountered most often. It is well known that steel behaves non-linearly for large currents, which can occur during lightning strikes or fault situations in high-power circuits. Therefore experiments have been performed to explore the limits of the linear description.

Above mentioned grounding structures have been successfully employed in several installations. In this thesis we restrict ourselves to a case study on our laboratory setup of a Gas Insulated Switchgear.

Samenvatting

Elektronische apparaten mogen elkaar niet storen; elk apparaat moet daarom voldoen aan eisen ten aanzien van de emissie van, en de immuniteit tegen elektromagnetische storingen. Uit Electromagnetic Compatibility (EMC) analyses blijkt dat die storingen zeer vaak via de bekabeling binnenkomen of daardoor worden geëmitteerd. Het EMC-onderzoek beschreven in dit proefschrift heeft tot doel een lineaire en reciproque bescherming van de bekabeling te bereiken. Zowel de inkoppeling als de uitkoppeling van de elektromagnetische storingen worden beschreven met behulp van het begrip transfer-impedantie.

Om de transfer-impedantie van kabels te meten zijn uit de literatuur twee methoden bekend: de triaxiale methode en de draadinjectie-methode. Metingen hebben aangetoond, dat wanneer beide methoden worden vergeleken, er een discrepantie blijkt op te treden. Deze verschillen konden door een theoretische analyse verklaard worden.

Door het hele proefschrift heen worden gemeten transfer-impedanties vergeleken met transfer-impedanties die volgen uit uitgebreide computerberekeningen.

In veel gevallen is de transfer-impedantie van kabelmantels te hoog en moet er een extra bescherming gebruikt worden. Metalen kabelgoten worden al vaak gebruikt voor mechanische bescherming. Veldberekeningen en metingen laten zien dat ze ook zeer bruikbaar zijn voor EMC-doeleinden. Voor goten van niet-magnetisch materiaal zijn eenvoudige formules gevonden, die een goede beschrijving geven van de transfer-impedantie als functie van de geometrie, de frequentie en de materiaaleigenschappen. Voor de veel voorkomende ondiepe stalen goten, al dan niet gegalvaniseerd, zijn deze formules in de praktijk ook nog zeer bruikbaar. Het is bekend dat staal zich niet-lineair gedraagt voor grote stromen, die kunnen voorkomen tijdens blikseminslagen of tijdens foutsituaties in energietechnische installaties. Derhalve zijn er experimenten uitgevoerd ter bepaling van de grenzen van de lineaire beschrijving.

De bovenstaande aardingsstructuren zijn met succes toegepast in diverse installaties. In dit proefschrift beperken we ons tot een case study aan onze laboratorium opstelling van gesloten schakelmateriaal.

Chapter 1

Introduction

Electronic equipment should operate reliably without electromagnetic interference; therefore all equipment has to fulfill certain requirements on the emission of, and immunity for, electromagnetic disturbances. Electromagnetic Compatibility (EMC) is the objective, which is only reached, when these requirements are met, and harmonic co-existence is possible. The official IEC (International Electrotechnical Commission) definition of EMC is [IEC 50(161-01-07)]:

> The ability of a device, equipment or system to function satisfactorily in its electromagnetic environment without introducing intolerable electromagnetic disturbances to anything in that environment.

From previous EMC studies it is known that disturbances very often enter equipment via the cabling and wiring, and are also emitted by means of the cabling and wiring [Goe 92, pp.18-19]. The emphasis of the EMC research in this thesis is on linear and reciprocal protection of the cabling and wiring: the same protective measures then reduce the emission as well as the susceptibility.

From a broad point of view EMC is already very old. It started with the lightning experiments of Benjamin Franklin in 1752. Lightning current is characterized by a short high peak and a long decaying tail. When lightning strikes a building, the energy in this tail can be responsible for fire. Lightning rods, with a low resistance, are used to reroute the lightning current and to prevent the outbreak of fire. The second step in the EMC evolution was the introduction of the protective earth or safety ground (around 1880), which protects humans against dangerous touch voltages between devices or between equipment and a conducting floor, in fault situations. In both these classical EMC applications an effective grounding only needs to be designed for low frequencies.

With the increasing use of vulnerable electronics and faster signal speeds, EMC is becoming more and more important, which is also demonstrated by the introduction of new regulations by governmental bodies (e.g. 89/336/EEC [EEC 89]). Nowadays fast disturbances can cause damage to electronics, or can corrupt computer data and digital communication; clearly grounding should be designed for a

large bandwidth. Earlier work at the Eindhoven University of Technology, which stressed the importance of current flow in closed loops [Laa 86, Laa 87, Hou 89, Hou 90, Deu 92], has led to a new definition of grounding published by van der Laan et al. in 1993 [Laa 93]:

> Grounding provides a set of interconnected paths for currents, designed to have a low transfer impedance, in order to keep the interference voltages at the terminals of sensitive equipment low.

In this definition different terminals may be considered, an actual signal input, a power supply input, but also signal outputs, which may be sensitive to disturbances and must be protected as well. The transfer impedance (Z_t) is the ratio of the interference voltage at a critical terminal and the disturbance current. Depending on the "input" voltage considered, we reduce the transfer impedance by an appropriate design of the "interconnected grounding paths". The metal structures used for this purpose are called "grounding structures" (GS). It should be noted that grounding in this definition mainly refers to all low voltage sides of circuits and does not necessarily involve a connection to "Mother Earth".

The counterpart of the transfer impedance is the transfer admittance (Y_t), the ratio of the current to a sensitive input caused by a disturbing voltage. The transfer admittance is important when the electric field at the grounding structure is significant. This is usually not the case, because the large bulk of grounded metal keeps the local electric field low. In addition for structures with a high optical coverage, such as a cable braid, the transfer admittance is so small that its effects can be neglected when compared to the effects of the transfer impedance. Because of these arguments, which are based on earlier observations in our group and on papers by Hoeft [Hoe 88] and Demoulin [Deg 93, pp.223-224], in this thesis only the transfer impedance Z_t is discussed.

In large industrial installations metallic cable trays are often used for the mechanical support of cabling and wiring. When the trays are properly interconnected and allow current flow, they can also be conveniently used as grounding structures. Already in the seventies studies have been performed on the transfer impedance of cable trays, though these reports were not intended for publication e.g. [Tay 75]. In 1990 van Houten, of our group, presented computer calculations on cable trays, under high-frequency conditions [Hou 90]. He verified his calculations with measurements at about 100 MHz on shallow and deep aluminum trays. In 1992/1993 Maciel, from the French EMC-group in Lille, presented the results of his study on shallow steel trays [Mac 92a, Mac 93]: he compared measurements between 10 kHz and 10 MHz with computer calculations, for which the tray was replaced by a large set (≈ 50) of parallel wires. In this model the skin effect is not taken into account.

A large part of this thesis is devoted to the transition of a tube as grounding structure, to a slotted tube, to a deep tray, to a shallow tray and to a plate.

The behavior of non-magnetic and ferromagnetic (steel) structures has been analyzed over a large frequency range (10 Hz - 10 MHz). Boundary Element Method (BEM) calculations [Oersted], which solve the complete skin effect problem, and analytic calculations, which are possible in certain limiting cases, are confirmed by measurements. In general the BEM approach is being used in various mathematical formulations [Bre 84, Kos 94]. Since the precise formulation used in the IES program [Oersted] is not known, extensive checks have been made.

In Chapter 2 of this thesis the basic concept of the transfer impedance is described. Chapter 3 discusses the transfer impedance of cables with a nearby return conductor and a non-central inner conductor. The difference between measurements in a triaxial setup and in a wire injection setup is explained. In the "cables" discussed, the shield is a copper tube, a slotted copper tube or a copper braid. In Chapter 4 simple formulas, which describe the transfer impedance of non-magnetic trays, are obtained from BEM calculations and measurements. These "engineering" expressions can be used as a guideline by designers of large installations. Chapter 5 discusses the differences between non-magnetic and ferromagnetic grounding structures; the engineering expressions obtained for non-magnetic trays can also be applied to shallow steel trays. Steel grounding structures show non-linear behavior for large currents. We explore the limitations of our assumption on linearity in Chapter 6. Finally Chapter 7 demonstrates the application of the transfer impedance concept to our laboratory Gas Insulated Switchgear (GIS) setup.

Chapter 3 has been partly published in the IEEE transactions on EMC [Hel 95b]. The results of Chapters 4 and 5 have been presented at the EMC Roma'94 conference [Hel 94a]. Chapter 6 has been presented at the EMC Zürich conference in 1995 [Hel 95a]. The results of Chapter 7, though with different diagnostics, have been published partly in Energietechniek [Hor 94b] and have been presented at the ISH'95 conference [Deu 95].

Chapter 2

The transfer impedance concept

The transfer impedance (Z_t) is defined as the ratio of the differential mode voltage and the disturbance current causing it; Z_t can be experimentally determined if we inject a current and measure the resulting voltage. The value of Z_t depends on the three-dimensional geometry of both the injection and the DM circuit. The transfer impedance concept is quite general and can also be applied to multi-conductor and multi-shield cables.

2.1 Introduction

In Fig. 2.1a a signal source is connected to a load R_l by only one signal lead (1). Ampère's law however tells us that the signal current has to flow in a closed loop. The ground lead (g), which is always present in one form or another, closes this loop. The area of the loop thus formed is often unknown and can be very large. Already a small time varying external magnetic field may cause a large disturbance voltage over R_l. An obvious and also the usual solution to this problem is to deliberately add a second lead (2), which reduces the area of the signal loop as is shown in Fig. 2.1b. However we now have two loops; the second loop, closed by the ground conductor (g), is in EMC terms known as the Common Mode (CM) loop.

We can try to open the CM loop (regulations often prescribe at least one connection to safety ground). When the loop is left open large voltages can be induced over the interruptions. In extreme cases this may result in flashovers, which cause new violent disturbances, and a closing of the loop. At higher frequencies parasitic capacitances (see Fig. 2.1c) automatically close the loop; at certain frequencies these capacitors may resonate with the self inductance of the CM loop, which can result in large CM currents, causing large disturbance voltages [Hel 94b]. Further complete insulation is often difficult to maintain in large systems, which makes the insulation concept expensive. We advocate therefore that the CM loops are deliberately closed and CM currents are allowed to flow according to the new definition of grounding given in the introduction of this thesis.
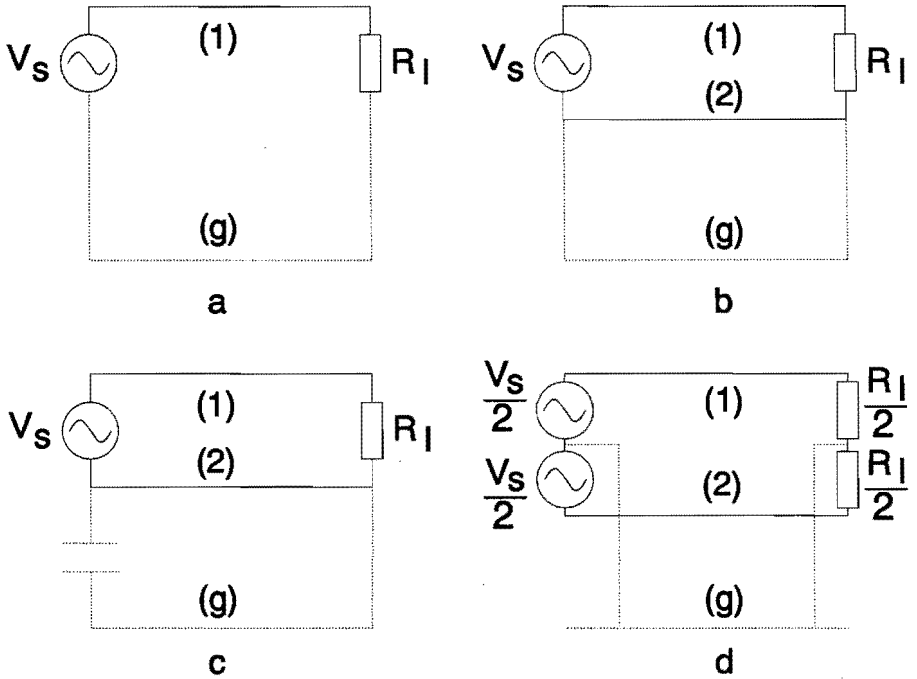
Fig. 2.1: Several possibilities for a signal connection: a: Only one lead between source v_s and receiver R_l; the signal current returns via an unknown (ground) conductor (g); b: Well designed unbalanced connection between source and receiver via leads (1) and (2); however a second loop is formed with lead (g); c: Unbalanced configuration with an interrupted second loop; parasitic capacitors however still close the loop; d: Balanced configuration taking into account other conductors (g).

2.2 Topology

In Fig. 2.1b we sketched a three-conductor configuration for unbalanced signal transport. In Fig. 2.2 we give a more general picture of signal transport between two black boxes. The latter picture is valid for balanced and unbalanced signals. If all significant currents between the two black boxes flow via two signal leads (1) and (2) and one ground lead (g), we have $i_1 + i_2 + i_g = 0$. This is a direct consequence of the continuity equation for currents, applied to the closed surface sketched in Fig. 2.2:

$$\oiint_S \left(\vec{J} + \frac{\partial \vec{D}}{\partial t} \right) \cdot d\vec{S} = 0 \tag{2.1}$$

where $\vec{J}$ is the total material current density, $\partial \vec{D}/\partial t$ the displacement current density and S the area of the closed surface. This continuity equation can be obtained from Maxwell's equations and is the foundation of Kirchhoff's current
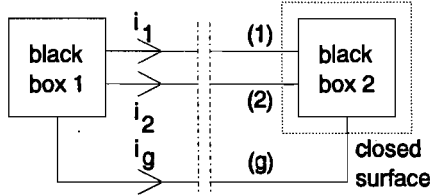
Fig. 2.2: Three-conductor topology for signal transport.

law [Ram 84, p.174]. In other words it says that currents flow in closed loops. For EMC analysis it is desirable to identify these loops [Hou 90, p.26].

In general for a n-conductor system $n-1$ independent loops can be defined. Thus for our three-conductor system we have two independent current loops, which can be freely chosen. In the previous section we already mentioned the Common Mode (CM) loop, formed by the signal leads (1) and (2) on one hand and by the ground lead (g) on the other hand. The Common Mode current (i_{cm}), often the disturbance current, can be measured with a current transformer around leads (1) and (2), or around the ground lead (g):

$$i_{cm} = i_1 + i_2 = -i_g \qquad (2.2)$$

This choice is quite generally accepted.

We also have to define how i_{cm} flows over the leads (1) and (2). This choice depends on the details of the second loop, which is usually named the Differential Mode (DM) loop. This DM loop and its input and output circuits can be balanced (Fig. 2.1d) or unbalanced (Fig. 2.1b). In both cases we prefer the output voltage v_l over the load resistor R_l to be equal to $R_l i_{dm}$.

In the *balanced* signal system leads (1) and (2) are symmetric with respect to the ground lead (g). Also the source and load are symmetric. For the voltage over the resistor we then find: $v_l = (i_1 - i_2)R_l/2$, which we would like to be equal to $i_{dm}R_l$. That completes the definition of the flow of i_{dm} and i_{cm} over the leads (1), (2) and (g):

$$
\begin{aligned}
i_{dm} &= (i_1 - i_2)/2 \\
i_1 &= i_{cm}/2 + i_{dm} \\
i_2 &= i_{cm}/2 - i_{dm} \\
i_g &= -i_{cm}
\end{aligned}
\qquad (2.3)
$$

In the *unbalanced* signal systems leads (1) and (2) are no longer symmetric, nor are source and load. The impedance of the loop formed by leads (2) and (g) is usually much smaller than the load R_l, especially in our grounding concept. A plausible choice is then to let i_{cm} flow over lead (2) only and not over lead (1). The
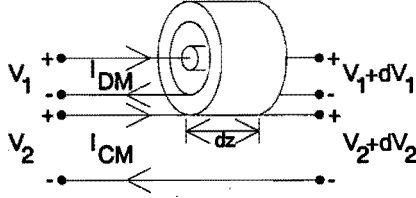
Fig. 2.3: Convenient definition of the CM and DM loops for unbalanced systems, illustrated with (a short element of) a coaxial cable above a ground plane.

Differential Mode loop then is the usual signal circuit (as intended in Fig. 2.1b), made up of the unbalanced signal source, the unbalanced receiver (R_l) and leads (1) and (2); $v_l = i_1 R_l = i_{dm} R_l$. With this choice the distribution of i_{cm} and i_{dm} over leads (1), (2) and (g) then is:

$$i_1 = i_{dm}$$
$$i_2 = i_{cm} - i_{dm} \qquad (2.4)$$
$$i_g = -i_{cm}$$

Because the grounding structures we describe later are typically part of an unbalanced system, in this thesis the latter choice for the distribution of i_{cm} and i_{dm} is used. The voltage v_l over the resistor is the same as the differential mode voltage (v_{dm}) defined by IEC 50(161-04-08); this is the same for balanced and unbalanced systems. As we have seen in the introduction (Chap. 1) the goal of our EMC research is to keep v_{dm} small.

Our definitions of Common Mode and Differential Mode are not often encountered in the literature, but in practice they are often tacitly assumed. They allow a simple definition of the transfer impedance (Z_t). Consider for example a coaxial cable above a ground plane. A disturbance current over the cable shield returns via the ground plane, but induces a interference voltage between the shield and inner conductor of the cable. In fact we have two coupled transmission lines of which an infinitesimally short element can be seen as a four-port network [Goe 92, p.124]. With our choice of the Common Mode and Differential Mode circuits, each loop coincides with one transmission line as is indicated in Fig. 2.3. In the frequency domain the transmission line equations then are as follows:

$$-\frac{dV_1}{dz} = Z_{11} I_{DM} + Z_{12} I_{CM} \qquad (2.5)$$

$$-\frac{dV_2}{dz} = Z_{21} I_{DM} + Z_{22} I_{CM} \qquad (2.6)$$

$$-\frac{dI_{DM}}{dz} = Y_{11} V_1 + Y_{12} V_2 \qquad (2.7)$$

$$-\frac{dI_{CM}}{dz} = Y_{21} V_1 + Y_{22} V_2 \qquad (2.8)$$

where I_{DM} and I_{CM} are the Fourier transforms of i_{dm} and i_{cm} respectively.

The coupling between both transmission lines is described by Z_{12}, Z_{21}, Y_{12} and Y_{21}. Linear passive networks are reciprocal, thus $Z_{12} = Z_{21}$ and $Y_{12} = Y_{21}$ [But 79]. By definition the transfer impedance and the transfer admittance per unit length are [Deg 93, p.222]:

$$Z_t' = -Z_{21} = -Z_{12} = \frac{1}{I_{CM}} \left(\frac{dV_1}{dz} \right)_{I_{DM}=0} \tag{2.9}$$

$$Y_t' = Y_{21} = Y_{12} = -\frac{1}{V_2} \left(\frac{dI_{DM}}{dz} \right)_{V_1=0} \tag{2.10}$$

These equations do not only apply to coaxial cables, but to wiring protected by grounding structures in general. As argued in the previous chapter we do not discuss the transfer admittance further and we concentrate on the transfer impedance.

A more general definition of the transfer impedance (Z_t) is the ratio of the total voltage showing up in the DM loop (with no signal source present) and the CM current:

$$Z_t = \left(\frac{V_{DM}}{I_{CM}} \right)_{I_{DM}=0} \tag{2.11}$$

where V_{DM} is the Fourier transform of v_{dm}. With this definition we can also describe local effects, such as coupling at interconnections of grounding structures (e.g. connectors) or the quality of the equipment housing (which can also be seen as a grounding structure [Hou 90, p.32]). When electrically short cables (length $l \ll$ wavelength λ) are considered the distributed Z_t' can be obtained from Z_t/l. In the following we will determine the transfer impedance Z_t' of grounding structures for wiring only for electrically short samples. We will also omit the prime; usually we will mean Z_t' when we write Z_t, but it will be clear from the context or from the dimensions; Z_t' is in $[\Omega\,\mathrm{m}^{-1}]$ and Z_t in $[\Omega]$.

A clear illustration of the combination of a distributed and a local transfer impedance is given in Fig. 2.4. A large CM current from a surge generator is sent over a copper tube. The tube is connected to an EMC-cabinet in which an oscilloscope measures the voltage v_{dm} induced in the loop formed by the tube and an inner conductor which is short-circuited at the far end. The transfer impedance of the tube proper is caused by a diffusion process of the current from the outside to the inside [Van 78, pp.117-123]; the CM current only causes delayed and strongly attenuated signals inside the tube. At the connection of the tube to the EMC-cabinet there is an imperfect contact between the tube and the backpanel. Local inductive coupling takes place through the remaining small gap and causes the sharp peak, with a shape proportional to $di_{cm}(t)/dt$, at the start of $v_{dm}(t)$. Within the transfer impedance concept there are two different approaches to reduce this peak. One is to lower the local Z_t; filling the small gap between tube and cabinet with indium gave good
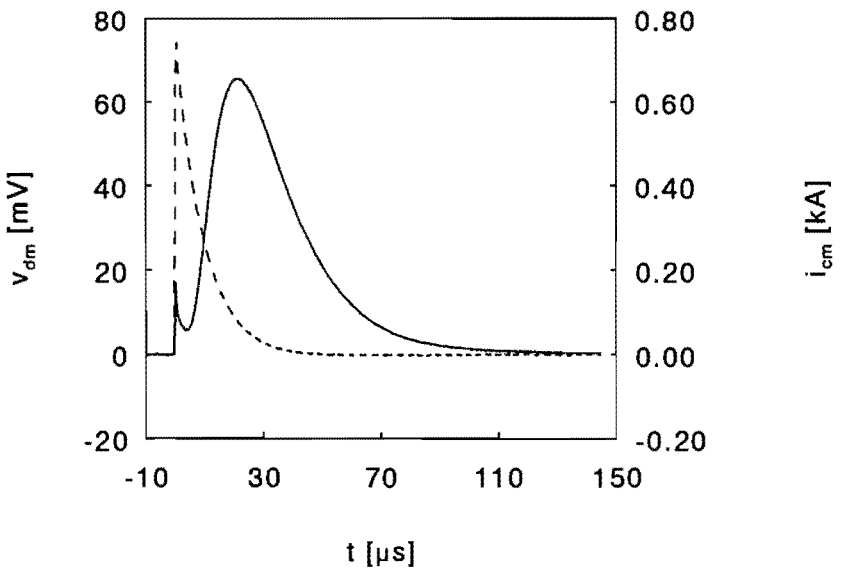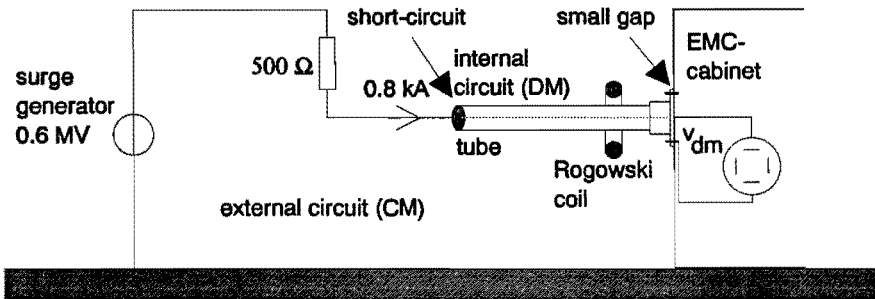
Fig. 2.4: Lightning surge current over a solid copper tube (2.2 m long) with a measurement wire on the inside. The transfer impedance of the tube itself is characterized by a slow diffusion process. The sharp peak at the start of the measured v_{dm} is caused by inductive coupling through a small gap between the EMC-cabinet and the tube. The solid line represents the voltage, the dashed line the common mode current over the tube.

results. The other approach is to divert the current away from the tube before it flows over the interconnection.

2.3 Geometrical properties

When the magnetic field is important for the coupling between two circuits, the three dimensional lay-out of both circuits and the current distribution in each circuit must be carefully regarded. Let us consider the three-lead configuration of Fig. 2.1b with a short-circuit instead of a signal source and R_l left open as is shown in Fig 2.5. The voltage $v_{dm}(t)$ is the line integral of the electric field $\vec{E}$ along the direct path between point 2 (positive) and point 1 (negative) and is given by:

$$v_{dm} = -\int_1^2 \vec{E} \cdot \vec{dl} = \mu_0 \iint_S \frac{d\vec{H}}{dt} \cdot \vec{dS} + \int_4^1 \vec{E} \cdot \vec{dl} \qquad (2.12)$$

where S is the surface enclosed by loop 1-2-3-4, $\vec{H}$ the magnetic field strength and μ_0 the permeability of vacuum. The path between 4 and 1 in the line integral of $\vec{E}$ in the right hand side has to be taken along the dotted line on the surface of the middle conductor. For long lengths l and wavelengths large compared to the cross-sections of the circuit the problem simplifies to two dimensions.
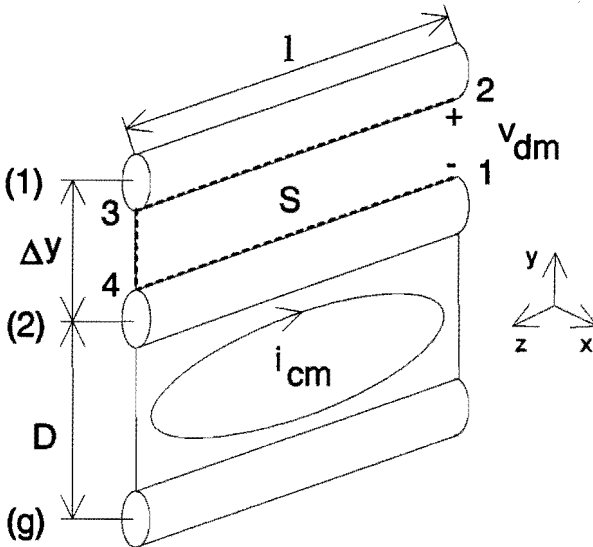
Fig. 2.5: Coupling mechanisms between the common mode current i_{cm} and the differential mode voltage v_{dm}; i_{cm} causes an electric field over path 1-4, and induces a flux in the loop 1-2-3-4.

For linear systems the transfer impedance $Z_t(\omega)$ can be defined as the ratio of $V_{DM}(\omega)$ and $I_{CM}(\omega)$ per unit length (as discussed in the previous Section), with V_{DM} and I_{CM} the Fourier transforms of v_{dm} and i_{cm} respectively:

$$Z_t = \left(j\omega\mu_0 \int_1^2 H_x dy + J_z/\sigma \right) / I_{CM} \tag{2.13}$$

in which σ is the conductivity (the reciprocal of the resistivity ρ) of conductor (2) and J_z the current density at the surface of conductor (2) along the dotted line 4-1. One can rewrite Eq. 2.13 as a combination of an impedance $Z_s = E_z/I_{CM}$, related to the local internal fields in the metal, and a mutual inductance M, per unit length, related to the outside magnetic field:

$$Z_t = Z_s + j\omega M \tag{2.14}$$

For a thin round wire Z_s equals the internal impedance Z_w, which is approximated by [Kad 59, p.11]:

$$Z_w = \begin{cases} R_0 & \text{for } r < \delta \\ R_0(1+j)(\frac{r_w}{2\delta} + \frac{1}{4}) & \text{for } r > \delta \end{cases} \tag{2.15}$$

where $R_0 = 1/\pi r_w^2 \sigma$ is the DC resistance per unit length, r_w the radius of the wire and $\delta = \sqrt{2/\omega\mu\sigma}$ the skin depth, with $\mu = \mu_0\mu_r$ the total permeability and μ_r the relative permeability. When the radii r_1, r_2 and r_g of the leads (1), (2) and (g) are small compared to the distances D and Δy, the mutual inductance M can be derived from "$H = I/2\pi r$":

$$M = \frac{\mu_0}{2\pi} \left\{ \ln\left(\frac{\Delta y}{r_2}\right) - \ln\left(\frac{D+\Delta y}{D}\right) \right\} \tag{2.16}$$

For two wire cables the distance Δy is typically a few millimeters, so when D is about twenty centimeters or more, the contribution of the second logarithm to the mutual inductance can be neglected, thus:

$$M = \frac{\mu_0}{2\pi} \ln\left(\frac{\Delta y}{r_2}\right) \tag{2.17}$$

and a typical value for M is 0.4 μH/m. At high frequencies the transfer impedance is dominated by the mutual inductance.

Now consider the case that conductor (2) is not a wire, but a solid tubular shield with outer diameter (o.d.) $2r_2$ and that the distance D is large, as in Fig. 2.4. The CM current through the shield is then roughly axially symmetric; there is no magnetic field inside the tube, therefore $M = 0$. The transfer impedance is

determined by the electric field on the inside wall of the shield only. An analytic expression is given by Schelkunoff [Sch 34] and Kaden [Kad 59]:

$$Z_t = R_0 \frac{kd}{\sinh(kd)} \qquad (2.18)$$

where $k = (1 + j)/\delta$ is the eddy current constant and $R_0 = 1/2\pi\sigma r_2 d$, about equal to the DC-resistance of the shield per unit length.

2.4 Measurement setup

The previous section shows that the transfer impedance not only depends on the three-dimensional layout of the DM loop and on the properties of the GS, but also on the layout of the CM loop. The measurement setup should be such that the measured transfer impedance is the value which is applicable to most practical situations. For cables there are two accepted measurement setups described in the literature; the triaxial setup [Van 78, p.163] and the wire injection method [Eic 88].

In the *triaxial* setup a cable is coaxially mounted inside a wide tube as shown in the inset of Fig. 2.6. As an example the measurement results of an RG-214/U and an YMvKas cable, which are used in the demonstration project described in Chapter 7, are shown in the same figure [Hor 94a]. At one end the DM voltage is measured between the cable shield and inner conductors, while at the other end the shield and inner conductors are short-circuited. The CM current is injected at the short-circuited end of the cable, flows over the shield towards the other end and returns via the wide tube to its source.

In the *wire injection* method the configuration is almost the same, but now the current returns via an injection wire instead of the tube. This wire is mounted directly against the cable under test as is shown in Fig. 2.7a (the cable in this picture is a solid copper tube with a lead inside). Measurement examples can be found in Chapter 3, e.g. Fig. 3.3.

In the triaxial setup the current over a cable shield is distributed symmetrically, while in the wire injection setup the injection wire influences the current distribution on the shield and can add an additional magnetic field inside the shield. When the transfer impedance is studied of cables which are used in cable bundles, the wire injection method can give more realistic values than the triaxial method, as will be discussed in Chapter 3.

For more general grounding structures, such as plates and cable trays (Chapters 4, 5 and 6), it is reasonable to assume that the CM current does not return nearby and therefore the wire injection method is not very realistic. On the other hand when a grounding structure without an axial symmetry is placed inside a tube, the
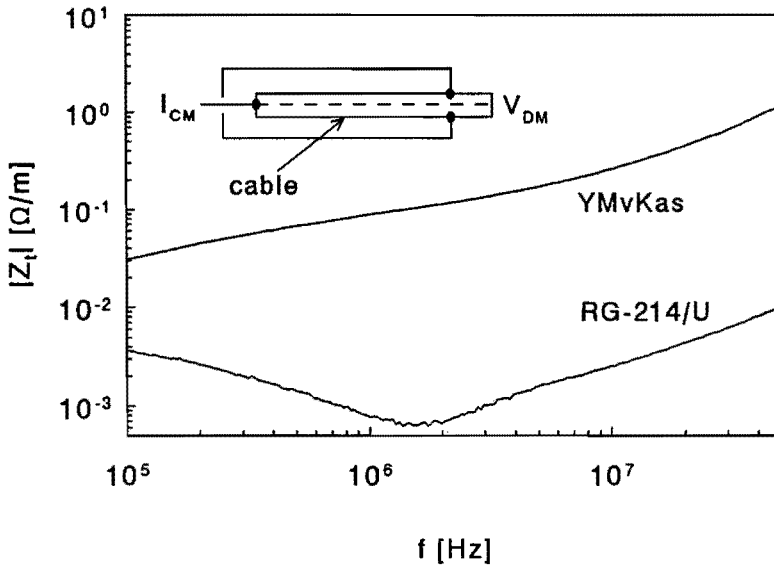
Fig. 2.6: *Measured transfer impedances of an RG-214/U and a YMvKas cable as function of the frequency f. The inset is a sketch of the triaxial setup used for these measurements.*

proximity effect causes an increased current density at the edges of the GS [Hou 90, p.56]; a tube with a cross section much larger than the largest dimension of the GS under test should be used, but this is often not practical. Therefore we designed a *modified wire injection* setup as is depicted in Fig. 2.7b. Instead of mounting a thin return wire close to the GS, we placed a broad copper foil (30 cm wide, 0.1 mm thick) at a distance of 95 cm from the bottom of the GS. In Fig. 2.8 the effect on the transfer impedance is shown when the nearby wire is replaced by the far away foil. Additionally the reciprocity of the transfer impedance is demonstrated in the same picture.
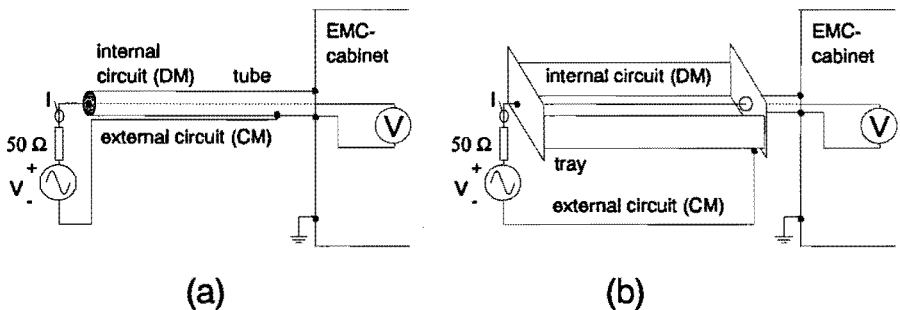
Fig. 2.7: *Schematic view of a wire injection measurement setup; (a) tube with a nearby return conductor, (b) cable tray with a far away return conductor (wire or foil).*
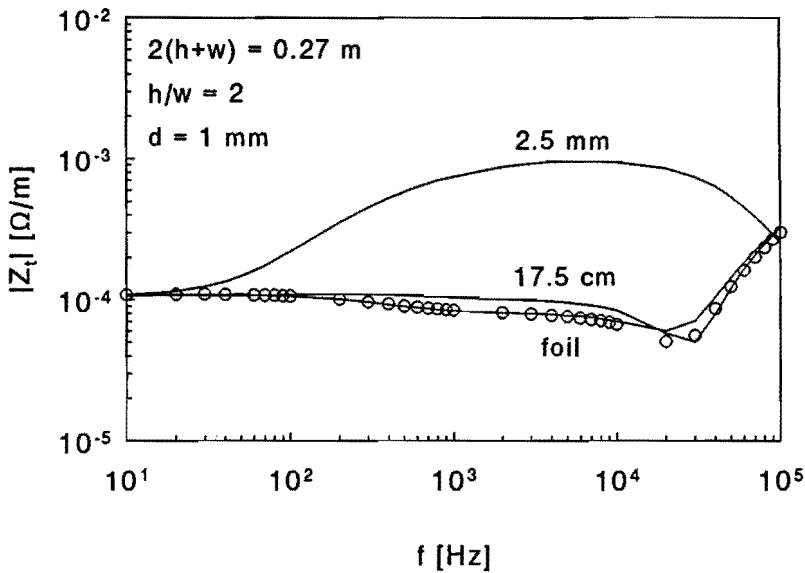
Fig. 2.8: Measurements of the Z_t of a cable tray with the return wire at 2.5 mm, at 17.5 cm and with a copper foil at 95 cm as return conductor, as indicated in the plot. With the foil as return conductor we also tested the reciprocal behavior of the Z_t (markers); a DM current is injected and a CM voltage measured. The height h of the aluminum tray is 9 cm, the half-width w is 4.5 cm and the thickness d is 1 mm (see 4.2).

Similarly, measurements on a copper tube with a non-central inner conductor and the foil as return conductor compare well with the values obtained from Eq. 2.18 assuming an axial symmetric current distribution. This implies, that the copper foil does not perturb the current distribution on a GS; i_{cm} can be assumed to return at infinity.

All GS's studied had a length of about 2 m. Metal plates were welded or soldered at the ends and one end was connected, via a copper tube, to an EMC-cabinet (Fig. 2.7b). In order to minimize the current over the imperfect connection between the tube and the EMC-cabinet (see the experiment from Fig. 2.4), the return conductor (injection wire of foil) for the CM current was connected to the end plate rather than to the cabinet. On the other end a current source was connected between the GS and the return conductor. Between 5 Hz and 100 kHz the CM current (400 mA peak-peak) was injected with a sine wave generator and measured by a Tektronix probe P6042 (DC-50 MHz). The DM voltage was measured with a lock-in amplifier placed inside the EMC-cabinet; the current probe output was used as reference. Above 100 kHz a network analyzer simultaneously measured the DM voltage and the current probe output. The tracking generator output of the network analyzer was used as source for the CM current.

Our setup can only be used to determine the distributed transfer impedance as long
as our GS's remain electrically short; the upper frequency limit of our setup there-
fore is about 10 MHz. Another limitation is the transfer impedance of the setup
itself: We obtained 6 $\mu\Omega$ with the lock-in and 6 mΩ with the network analyzer.
When the network analyzer was placed inside a special designed EMC-cabinet the
Z_t decreased to 1.6 mΩ. Please note that these values are obtained for the complete
setup in the mentioned frequency range; the much smaller triaxial setup combined
with the network analyzer and current probe had itself a Z_t of about 0.1 mΩ.

A two-port s-parameter set, an extension box of the network analyzer, is an inter-
esting alternative for the combination of the network analyzer and current probe.
The current probe can be omitted and measurements over a large frequency range
(300 kHz-1.8 GHz) can be made with a single apparatus. Our measurement setup
can be seen as a two-port network; in our setup two ports of the four-port net-
work in Fig. 2.3 are short-circuited and hence two ports remain. The scattering
parameters measured on these ports give a complete circuit description and the
transfer impedance can easily be derived from them [And 67, Bro 95]. Due to its
dimensions the limit of our setup with a 2 m long GS of course remains 10 MHz.
The intrinsic transfer impedance of the s-parameter set combined with the network
analyzer in the special EMC-cabinet remained 1.6 mΩ. In this thesis only limited
use is made of this method, because at the time most measurements took place
the s-parameter set was not yet available.

2.5 Nested grounding structures and multiple leads

When the transfer impedance of a certain grounding structure is too large we can
lower it by adding an extra GS. With an additional definition of the most appro-
priate currents and their loops, the above described transfer impedance concept
can be easily adapted. We will demonstrate this by adding an additional lead (3)
in parallel to lead (2) in the three-lead configuration from Fig. 2.5 as is sketched in
Fig. 2.9. According to the standard definition the Common Mode current now is
measured with a current probe around leads (1), (2) and (3); $i_{cm} = i_1 + i_2 + i_3 = -i_g$.
Further we define an additional current loop, which we will call the Intermediate
Mode (IM) current. This current is measured with a current probe around leads
(1) and (2); $i_{im} = i_1 + i_2$. The Differential Mode loop is not changed. In agreement
with Eqs. 2.4 we choose the following distribution of these loop currents over the
leads (1), (2), (3) and (g):

$$
\begin{aligned}
i_1 &= i_{dm} \\
i_2 &= i_{im} - i_{dm} \\
i_3 &= i_{cm} - i_{im} \\
i_g &= -i_{cm}
\end{aligned}
\qquad (2.19)
$$
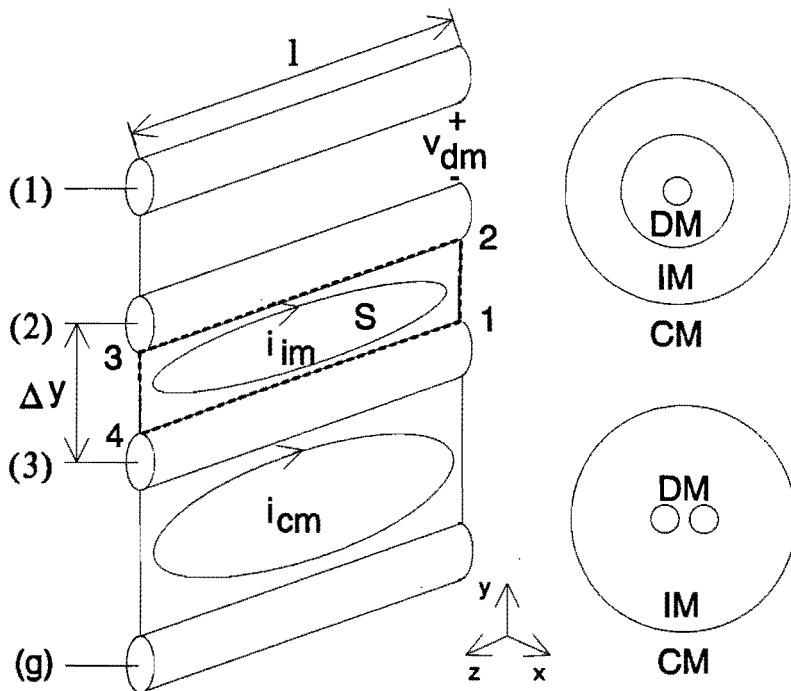
Fig. 2.9: Coupling mechanisms between the common mode current i_{cm} and the differential mode voltage v_{dm} via the intermediate mode loop. The pictures on the right hand show a multishield configuration (top) and a shielded multiconductor cable (bottom).

We can now calculate $\oint \vec{E} \cdot \vec{dl}$ for the IM loop:

$$\int_1^2 \vec{E} \cdot \vec{dl} + \int_2^3 \vec{E} \cdot \vec{dl} + \int_3^4 \vec{E} \cdot \vec{dl} + \int_4^1 \vec{E} \cdot \vec{dl} = -\mu_0 \iint_S \frac{d\vec{H}}{dt} \cdot \vec{dS} \qquad (2.20)$$

For simplicity we will at first neglect the contribution of the integral $\int \vec{E} \cdot \vec{dl}$ over paths 1-2 and 3-4. This is valid for long lengths l, when short-circuits at the ends are assumed. In a later stage loads are easily introduced again. We split up $\vec{E}$ and $\vec{H}$ into parts contributed by i_{im} and i_{cm}:

$$- \int_2^3 \vec{E}(i_{im}) \cdot \vec{dl} + \int_4^1 \{\vec{E}(i_{cm}) - \vec{E}(i_{im})\} \cdot \vec{dl} =$$
$$- \mu_0 \iint_S \frac{d}{dt} \{\vec{H}(i_{cm}) - \vec{H}(i_{im})\} \cdot \vec{dS} \qquad (2.21)$$

We can rearrange this equation so that all terms depending on i_{im} are written on

the left-hand side and all terms depending on i_{cm} on the right-hand side:

$$\int_2^3 \vec{E}(i_{im}) \cdot d\vec{l} \; + \; \int_4^1 \vec{E}(i_{im}) \cdot d\vec{l} + \mu_0 \iint_S \frac{d\vec{H}(i_{im})}{dt} \cdot d\vec{S} =$$

$$\int_4^1 \vec{E}(i_{cm}) \cdot d\vec{l} \; + \; \mu_0 \iint_S \frac{d\vec{H}(i_{cm})}{dt} \cdot d\vec{S} \qquad (2.22)$$

The right hand side of this equation equals the voltage induced by i_{cm} in the open IM loop (Eq. 2.12); in complex notation Eq. 2.22 can be rewritten, per unit length for long lengths l, as:

$$\left(J_{z,2}(I_{IM})/\sigma_2 + J_{z,3}(I_{IM})/\sigma_3 + j\omega\mu_0 \int_0^{\Delta y} H_x(I_{IM})\, dy \right) = Z_{t,3} I_{CM} \qquad (2.23)$$

where we have introduced:
$J_{z,2}$ and $J_{z,3}$ the current densities on the surface of conductor (2) respectively conductor (3);
σ_2 and σ_3 the conductivities of conductor (2) and (3);
$Z_{t,3}$ the transfer impedance, which describes the coupling between the CM and IM loop.

Now we write the left hand side of Eq. 2.23 as $Z_{IM} I_{IM}$, where Z_{IM} is the impedance per unit length of loop 1-2-3-4:

$$Z_{IM} = \left(J_{z,2}(I_{IM})/\sigma_2 + J_{z,3}(I_{IM})/\sigma_3 + j\omega\mu_0 \int_0^{\Delta y} H_x(I_{IM})\, dy \right) / I_{IM} \qquad (2.24)$$

When the conductor is not short-circuited at the ends, Z_{IM} is increased by the impedance of the loads.

In most practical applications with an IM loop the direct contribution of I_{CM} to V_{DM} can be neglected. We then can write $V_{DM} = Z_{t,2} I_{IM}$, where the transfer impedance $Z_{t,2}$ describes the coupling between the IM and DM loop. The overall transfer impedance, given by the ratio of V_{DM} and I_{CM} per unit length, is then:

$$\boxed{Z_t = V_{DM}/I_{CM} l = Z_{t,2} Z_{t,3} / Z_{IM}} \qquad (2.25)$$

which is in agreement with [Van 78, p.165]. Thus the additional lead (3) reduces the overall transfer impedance, when $|Z_{t,3}/Z_{IM}| < 1$. These considerations are also valid for GS's in general. For example in the top right picture of Fig. 2.9 a triaxial cable is shown; the IM loop is formed by the two shields. Some examples of measurements on tubular GS's are given in Fig. 2.10; depending on the GS chosen

a large reduction in the overall Z_t is possible. This is not the case for the anaconda, a flexible tube which can be very easily connected under most circumstances. It is not useful for EMC, because it is made from a helical strip and therefore behaves as a solenoid [Van 78, p.146]. As a result $|Z_{t,3}/Z_{IM}|$ is about equal to 1. The transfer impedance of the anaconda itself (not depicted in Fig. 2.10) is 0.15 mΩ/m for DC and starts to increase with the frequency already at 200 Hz.
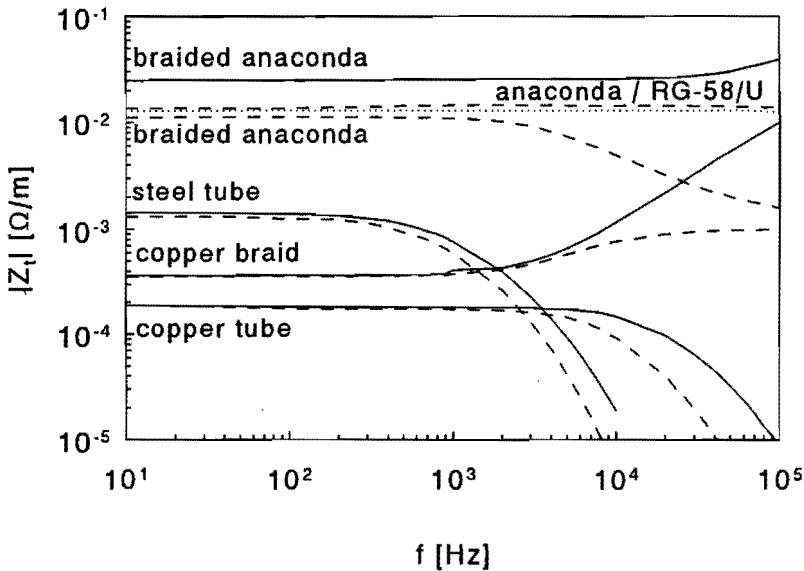
Fig. 2.10: Example of measured Z_t's of some tubular GS's combined with cables. The inner conductors are arbitrarily positioned as will be the case in practical use. The solid lines indicate the transfer impedance of the tubular GS itself, the dashed lines are measured with an RG-58/U inside the GS. The dotted line is the transfer impedance of the RG-58/U itself.

The overall Z_t is reduced, when Z_{IM} is increased, which can be done by inserting ferrite rings in the IM circuit [Hel 94b]. One could also interrupt the IM circuit, but then similar effects could occur as for interruptions in the CM circuit (Section 2.1), though usually at much higher frequencies.

In Fig. 2.9 also a two-lead shielded cable is shown (bottom right). When we assume that the shield is grounded at both ends, a convenient choice is to let i_{cm} flow over the shield only. Still we can distinguish three modes of operation. For each mode different choices for the current loops (DM and IM) are convenient:
(a) The two leads form a balanced circuit; both leads form the DM circuit, while the IM current flows equally over both leads and returns via the shield;
(b) The two leads form an unbalanced circuit; both leads form the DM circuit, while the IM current flows only over the grounded lead;

(c) Each lead forms a separate DM circuit with the shield. No IM loop is present. In the latter case we have two DM voltages and one CM current. This implies we should define two transfer impedances. The system can then be described with a matrix equation: $\vec{V}_{DM} = [Z_t]I_{CM}$. When we add an additional shield around each lead separately, these shields form two IM circuits with the outer shield. The coupling between the CM loop and the IM loops can be described with a matrix $[Z_{t,3}]$. The total system can then be described with:

$$\vec{V}_{DM} = [Z_{t,2}][Z_{IM}]^{-1}[Z_{t,3}]I_{CM} \qquad (2.26)$$

The $[Z_{t,2}]$-matrix contains the transfer impedances of both inner shields. The $[Z_{IM}]$-matrix contains the impedances of both IM loops formed by the two inner shields and the outer shields and also includes their mutual coupling. When more grounding structures are nested or more leads are added on the inside the system equation can be extended in the same manner. The advantage of our choice for the current loops is that each layer of GS's has its own loop.

2.6 Conclusion

We prefer a grounding system, which is based on, and benefits from, current flow in closed loops. In such systems the transfer impedance Z_t is an important parameter. With a convenient choice of the Differential Mode and Common Mode circuits the Z_t can be directly found from the DM voltage and the CM current. Our choice is different for balanced and unbalanced systems. Nesting of grounding structures or multiple leads can be easily described. We stress again, that other choices for the current loops can be made; each choice allows calculations, which, if consistently worked out, will give the correct currents in the various conductors.

We found the total transfer impedance by measuring the DM voltage at the terminals of interest and dividing it by the CM current. For cables it is convenient to determine a transfer impedance per unit length. For electrical short cables this transfer impedance can be easily obtained from the total Z_t. The overall transfer impedance describes the (indirect) coupling between CM and DM for nested grounding structures.

Chapter 3

The transfer impedance of cables with a nearby return conductor and a non-central inner conductor

The transfer impedance (Z_t) of a cable is often assumed to be a characteristic of the shield only, e.g. [Van 78, p.111]. We investigate the limits of this assumption by calculations and measurements. The first test cable was formed by a solid copper tube ("shield") and a wire inside; several positions, also non-central, were chosen for the wire. The common mode current (between 10 Hz and 100 kHz) through the tube had as return path a single wire, which was placed at several positions, near and at some distance from the shield. A second cable was formed by a tube with a longitudinal slot (comparable to some cables with a foil as a screen). Finally a third cable with a braided shield was tested. The three cables are depicted in Fig. 3.1. The results show that both the differential mode and the common mode circuit have to be carefully defined for a particular Z_t. Varying either circuit may alter Z_t drastically. Consequently, the Z_t of a particular cable measured in a triaxial setup is a characteristic of that setup and cannot always be used in another setup as for instance in cable bundles.
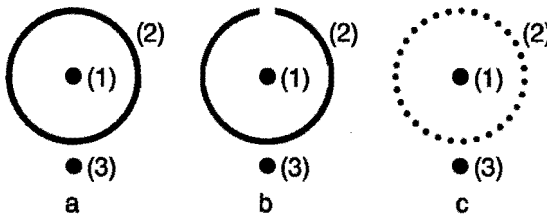
Fig. 3.1: Cross-section of the test cables used in our experiments: a: closed tube; b: slotted tube; c: braid. The positions of the inner and outer conductor were varied. When compared to Fig. 2.1b lead (3) is identical to lead (g).

3.1 Introduction

In our grounding concept the shields of cables in cable bundles are connected to each other at both ends. The main coupling path between the cables then usually is the coupling between the DM circuit of one cable to the CM circuit and from the CM circuit to the DM circuit of another cable [Sal 93]. This can be described by the respective transfer impedances of the cables. Equation 2.18 gives the transfer impedance of a closed tube for an axially symmetric current distribution over the shield. In cable bundles however the cables are close together and the symmetry in current will be disturbed.

Consider Fig. 3.1a where conductor (2) is a tubular shield around lead (1). When the return conductor (3) is a single wire placed close to the shield, the current distribution in the shield is no longer axially symmetric ($J_z = J_z(r, \phi)$) and a magnetic field (H) exists inside the tube. This is illustrated by a Boundary Element Method calculation [Oersted] for a tube as used in our experiments, at the frequency of 1 kHz (Fig. 3.2).
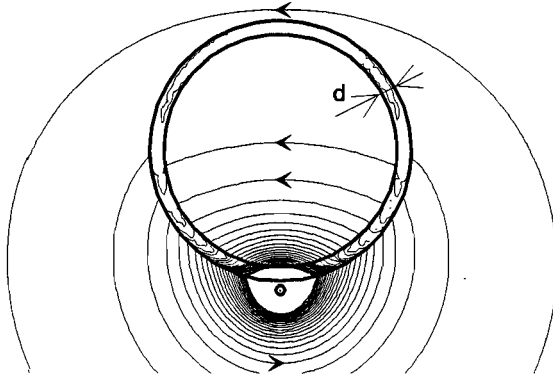
Fig. 3.2: The magnetic field (H) inside a tube, as used in our experiments, with a nearby (CM) return wire, calculated with the Boundary Element Method [Oersted]. The field lines near the return wire are too close together to be plotted. The frequency is 1 kHz; the wall thickness d of the tube is then 0.66 times the skin depth.

The H-pattern inside depends on the distance of the return wire, on the tube parameters and on the frequency. One may split the current distribution $J_z(r, \phi)$ in the shield into two terms $J_{z,s}(r)$ and $J_{z,ind}(r, \phi)$. The first, which gives the axially symmetric current density $J_{z,s}$, results in I_{CM} when integrated over the cross section of the shield, and is independent on the return path for I_{CM}, which may be either a single wire (3) (wire injection method, see Fig. 2.7a) or a coaxial cylinder (triaxial setup, see the inset of Fig. 2.6) outside the cable. At low frequencies ($\delta \gg d$) $J_{z,s}$ is also independent of r. Again there is no H-field inside the tube due to $J_{z,s}$.

The induced current distribution $J_{z,ind}$ is caused by the presence of the (near) return wire. This pattern of longitudinal eddy currents closes on the shield; near wire (3) $J_{z,ind}$ flows in the direction opposite to the I_{CM} through that wire and returns at the other side of the tube. In general $J_{z,ind}$ can be induced by any externally produced magnetic field. At very low frequencies $J_{z,ind}$ is reduced by the resistance of the tube. Inside the tube one then finds the pure vacuum field caused by I_{CM} through the return wire. However, the contribution of the mutual inductance to the transfer impedance is negligible at these low frequencies. Therefore Z_t then is yet virtually independent of the position of the inner conductor and of the outside wire. At higher frequencies the flux between the shield and inside wire varies with the position of both wires (1) and (3); Z_t varies accordingly. When the tube is made of ferromagnetic material, magnetostatic shielding can occur, this will be discussed in Chapter 5. At very high frequencies, for which $\delta < d$, $J_{z,ind}$ provides an effective shielding of the interior of the tube and Z_t decreases exponentially with increasing frequency for all positions of the inner and outer wires.

The central position of the inner conductor (1) is a special case. It turns out that Z_t is independent of the position of the outer wire (3), and is always given by Eq. 2.18. This can most simply be understood by considering the reciprocal situation. When the coaxial DM circuit is excited, there is no magnetic field outside the tube because of the symmetry. Then only the electric field at the outside of the tube determines Z_t according to Eq. 2.18.

When the return wire is far away from the tube, $J_{z,ind}$ becomes negligible with respect to $J_{z,s}$. The transfer impedance then approaches the value for a symmetrical current distribution. However, if a thin longitudinal slot is made in the originally closed tube (Fig. 3.1b), some magnetic field penetrates into the interior of the tube and the behavior of Z_t becomes inductive at high frequencies. With the return conductor nearby one can expect additional coupling, depending on its position with respect to the slot.

When the originally closed tubular shield is replaced by a braided shield (Fig. 3.1c), the CM current pattern can be expected to follow the wires, since the currents through the individual wires do not cross over from wire to wire at crossing points or between parallel wires [Van 75, Tyn 76]. When the helical shield wires have a short pitch, the current distribution in the shield is quickly homogenized in ϕ. Magnetic fields now penetrate easily. However, when the inner conductor (1) is at the center of the braided cylinder, Z_t is practically independent of the position of conductor (3), much like the situation for the solid shield.

3.2 Measurements

An overall description of the measurement setup is given in Section 2.4; the setup is depicted in Fig. 2.7. Measurements have been made on *(i)* a copper tube ($l =$
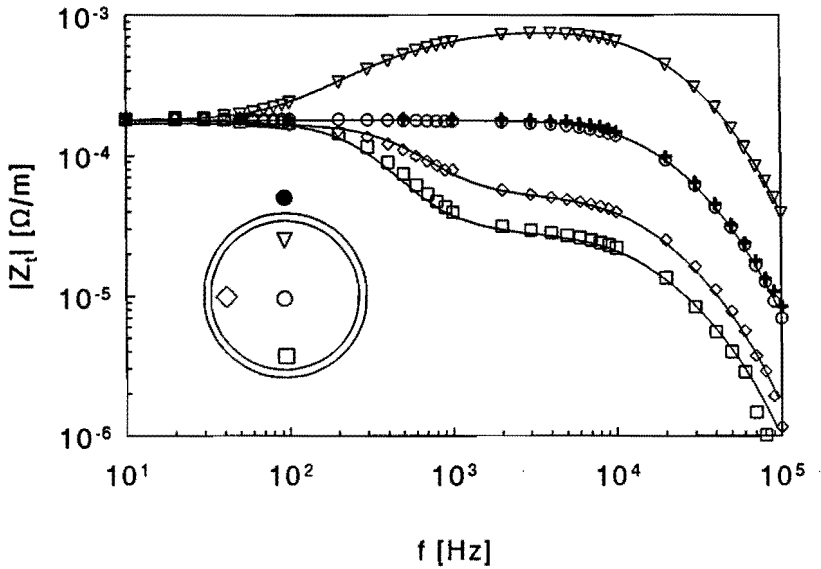
Fig. 3.3: Measured Z_t's for a copper tube with a return wire (•) close to the shield;
the markers indicate the positions of the inner conductor as shown in the inset. The
solid lines are Multipole Expansion (ME) calculations (see Section 3.3). The bold +'s
are measured with axially symmetric current distribution and central inner conductor.
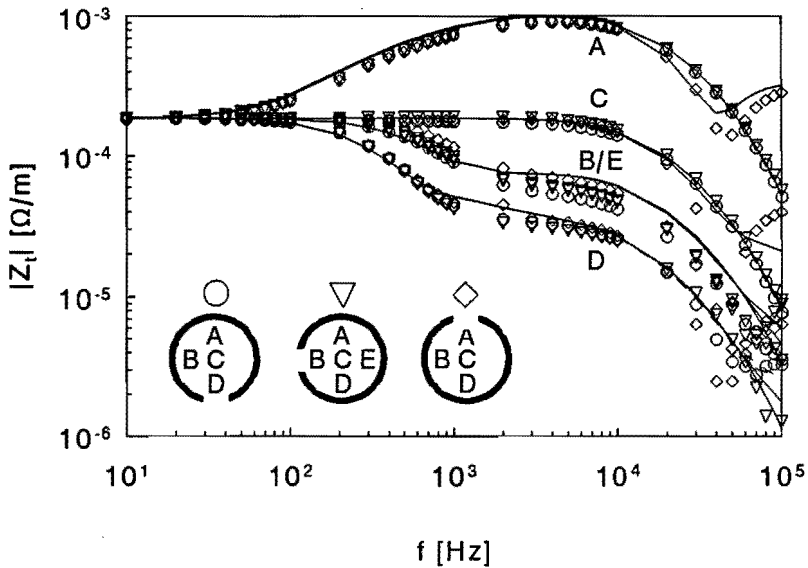
Fig. 3.4: Measured Z_t's for a slotted (width $b = 1$ mm) copper tube with a return wire
close to the shield; the markers indicate the positions of the slot with respect to the
return conductor as shown in the inset. Up to 30 kHz the Z_t equals the Z_t of the closed
tube. The solid lines are ME calculations and calculations of M_{slot} (see Section 3.3).
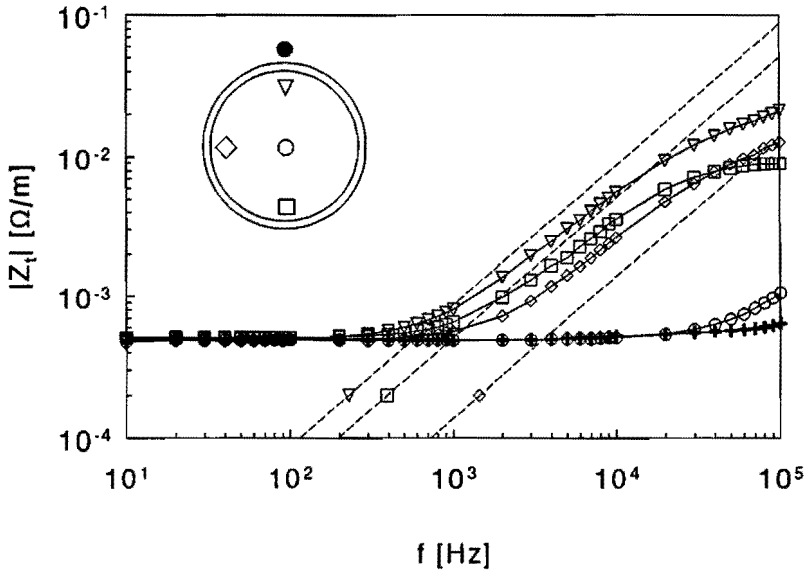
Fig. 3.5: Measured Z_t's for a copper braid with a return wire (•) close to the shield; the markers indicate the positions of the inner conductor as shown in the inset. The additional data indicated by bold +'s refer to an axially symmetric current distribution, while the inner conductor is at the center. The three dashed lines and their marker are inductance calculations, which are explained in Section 3.3. These graphs are quite different from the results of the tubes shown in Fig. 3.3 and Fig. 3.4.

2.03 m, o.d. $2r_1 = 28$ mm, wall thickness $d \approx 1.39$ mm, $\sigma \approx 5.0 \cdot 10^7$ $\Omega^{-1}m^{-1}$), on (ii) two slotted tubes ($l = 2.00$ m, o.d. $2r_1 = 28$ mm, wall thickness $d \approx 1.33$ mm, slot width $b = 1$ mm and 2 mm, respectively, $\sigma \approx 5.0 \cdot 10^7$ $\Omega^{-1}m^{-1}$) and on (iii) a copper braid ($l = 2.02$ m, o.d. 38 mm, inner diameter (i.d.) 32 mm). The braid consisted of two interwoven bundles of helical wires with a total copper cross section of 50 mm^2 and a pitch of about 13 cm. It was pulled around a PVC tube. The inner conductor was a copper wire of 2 mm^2 mounted at the center, or a wire of 1 mm^2 mounted at approximately 10.6 mm from the center, for the three angular positions indicated in the inset of Fig. 3.3. At one end the inner conductor was carefully shorted to the full circumference of the tube or braid. At the other end the voltage V_{DM} was measured. Both ends of the braid were mounted in such a way that I_{CM} was evenly distributed over the wires. The return wire for I_{CM} was a 1 mm^2 wire, which was taped against the tube or braid. Its center lies 1 mm from the outside of the closed tube and the braid. For the slotted tubes this distance is 2.2 mm.

The results of the measurements on the closed tube are given in Fig. 3.3. For the measurements with an (approximately) axially symmetric current over the shield, the return wire was replaced by the copper foil (bold +) at a distance of 95 cm

below the tube. Below 30 Hz the Z_t is given by the DC resistance of the tube. For the central position of the inner conductor Z_t remains at this value up to 2.8 kHz, the frequency for which the thickness d of the tube wall becomes equal to the skin depth δ. The fall-off of Z_t up to 100 kHz is in accordance with Eq. 2.18. These data compare very well with those for an axially symmetric current distribution on the tube (compare the $+$ and the $\circ$ in Fig. 3.3).

For the upper position of the inner conductor at a radius (r) of about 9.3 mm (curve labeled with $\triangledown$), nearest to the external wire, Z_t starts to increase above 30 Hz. This is caused by the increased current density near the external wire, described by $J_{z,ind}$. At the two other non-central positions Z_t decreases. Note that for a homogeneous external field perpendicular to the tube the characteristic frequency, at which eddy currents become important, is given by $r_1 d = \delta^2$ [Kad 59]: $f = 0.26$ kHz.

In the measurements on the slotted tubes, the angular position of the slot, with respect to the return wire, was varied in steps of $\pi/2$. Figure 3.4, located below Fig. 3.3, shows the results for the tube with the 1 mm slot. The additional magnetic coupling through the slot is negligible at low frequencies. The transfer impedance (Fig. 3.4) then is not significantly different from the Z_t of the closed tube (Fig. 3.3), regardless of the position of the slot.

To study the additional effect of the magnetic coupling through the slot, measurements at higher frequencies are necessary. Therefore we used the network analyzer in the special EMC-cabinet as discussed in Section 2.4. The transfer impedance of this setup itself however proved to be too large for measurements on the tube with the 1 mm slot. Therefore a second tube with a 2 mm wide slot was prepared. Even with the wider slot correct measurements were only possible, when the return wire was positioned close to the slot. The measured mutual inductance (M_{slot}) at 10 MHz for this position of the outer conductor is given in Table 3.1. Obviously M_{slot} strongly depends on the exact positions of the inner conductor, the return conductor and the slot.
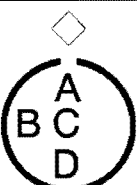
	position	M_{slot}	
		measured	calculated
	A	4.9 nH	4.8 nH
	B	96 pH	23 pH
	C	0.47 nH	0.23 nH
	D	48 pH	11 pH

Table 3.1: The measured and calculated mutual inductance M_{slot} at 10 MHz caused by the coupling of the magnetic field through the slot (slot width $b = 2$ mm) in the tube. The injection wire was mounted directly above the slot. The calculations are discussed in Section 3.3.

For the braid the results of the measurements are given in Fig. 3.5. To make comparison between the tubes and the braid easier, Fig. 3.5 has been located on the page opposite to Figs. 3.3 and 3.4. The transfer impedance for a symmetric current distribution and a central inner conductor (+ markers) barely deviates from the DC value up to 100 kHz. Some inductive behavior above 20 kHz is observed for a central inner conductor and CM return wire nearby (∘). The mutual inductance M is in this case about 1 nH/m. This M-value is low; the arguments based on reciprocity, as for the tube, would predict $M = 0$. Larger M-values, about 100 nH/m, are measured for the off-center inner conductors with the CM return wire nearby. The braid provides only little shielding for higher frequencies; this will be explained in Section 3.3.

3.3 Calculation and comparison with experiment

3.3.1 Tube

Two types of calculations have been carried out. In the first, the Boundary Element Method (BEM) is employed and the skin effect is considered [Oersted]. In the second, a Multipole Expansion (ME) of the relevant fields is used, which is a faster method. The results of both methods agree well within the accuracy allowed by the approximations in both methods.

In the ME calculations we follow the outline given by Kaden [Kad 59]; the magnetic fields outside and inside the tube due to I_{CM} in the return wire (3) are expanded into line multipole fields up to a certain order m. The return wire is at a fixed distance $2a$ with respect to the axis of the tube (Figs. 3.1 and 3.6a). Details of the calculations are given in Appendix A.1. In the tube wall the E- and H-field vary in the radial direction according to Bessel functions of integer order m, which are approximated by exponentials for our thin wall. The azimuthal variation is proportional to $\cos{(m\phi)}$ for E_z and for H_ϕ, and the corresponding sine function for H_r, where ϕ is the angle between inner and outer wire as seen from the center of the tube (Fig. 3.6a). The fields should be continuous for both the tangential H_ϕ- and the perpendicular B_r-components at the inside and outside wall of the tube.

In correspondence with the discussion in Section 2.3, also here we obtain from Faraday's law that two terms contribute to the total Z_t; first the E-field at the inside of the wall due to the symmetric I_{CM} and the longitudinal eddy currents $(J_{z,ind})$ combined, and secondly the magnetic flux between the wall and the inner conductor (1) at position (r, ϕ). This is illustrated with three drawings in Fig. 3.6. The I_{CM} through the tube does not result in a H-field inside. The intensity of the m-th order magnetic field of wire (3) varies with $((r_1/2a)(r/r_0))^m$. The convergence is slow when positions of the inner conductor (r, ϕ) and of the return wire $(2a, \pi)$ are close to the tube surfaces at r_0 and r_1 respectively; high orders m up to 100 are needed for sufficient (10^{-3}) relative convergence.

(a)   (b)   (c)
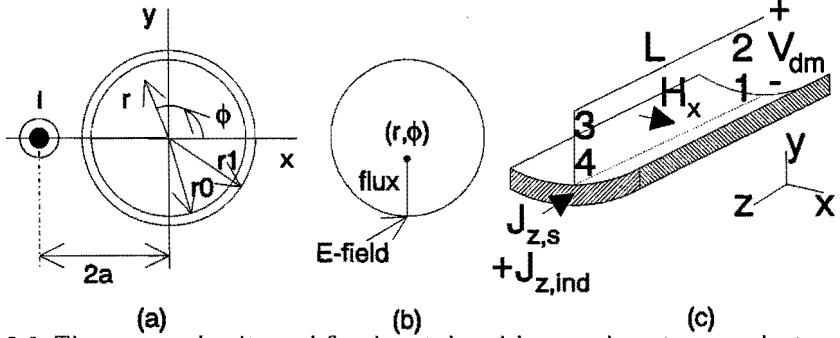
Fig. 3.6: The current density and flux in a tube with a nearby return conductor. When Faraday's law (see Section 2.3) is applied to the loop 1-2-3-4, we find that two terms contribute to Z_t; first the E_z-field due to $J_{z,s}$ and $J_{z,ind}$, and secondly the time-varying magnetic flux through the area loop 1-2-3-4. The contributions of $J_{z,ind}$ and the magnetic flux have opposite signs and compensate each other exactly at the center of the tube; in this case only $J_{z,s}$ contributes to Z_t. Then Z_t is given by Eq. 2.18.

Position:	center (○)	top (▽)	mid (◇)	low (□)	
r (mm)	0.0	9.3±0.1	11.0±0.5	11.6±0.2	11
d (mm)	1.38±0.05	1.34±0.03	1.35±0.11	1.5±0.1	1.38
σ (10^7 Ω^{-1} m^{-1})	4.88±0.29	5.00±0.23	5.26±0.58	4.37±0.27	5.80

Table 3.2: The fitted values for the position of the inner conductor r and the wall thickness d, both in mm, together with the conductivity in 10^7 Ω^{-1} m^{-1}, of the closed tube. Both the off-center value of r and the value for d correspond to the known values (last column). For the center position the value of r was not fitted. The lower value of r for the top position is due to sagging of the inside wire. The large deviation for d and σ in the low position are due to the increased uncertainty due to the small values of Z_t; e.g. the lowest values at the frequencies above 50 kHz had to be removed in the fitting procedure for this position.

With the inner wire at the center, $r = 0$, the E-field at the inside wall, produced by the longitudinal eddy currents, is exactly compensated by the magnetic flux for all orders m, independent of the position of the return wire, as shown in Appendix A.1. Only the Z_t due to the CM current (Eq. 2.18) remains, as it should, because of the reciprocity as mentioned before.

The lines drawn through the measured Z_t of Fig. 3.3 are a fit to the ME calculation. Several parameters were varied to obtain the fit; first, the r value of the inner conductor for the three off-center positions; second, the wall thickness of the tube; third, the conductivity, since the copper might contain impurities. The external return wire was at the fixed position of 15 mm from the tube axis. The fitted values are equal to the known parameters within a reasonable accuracy (see Table 3.2). The conductivity appears to be 16 % higher than the value for pure copper.

In Fig. 3.7 the calculated Z_t is shown as a function of the position r of the inside wire, in the plane through the axis of the tube and the return wire. The values are divided by the Z_t at $r = 0$ from Eq. 2.18, and are given for the three frequencies 0.1, 1 and 10 kHz. The return wire is again at the distance $2a = 15$ mm. The outer radius r_1 is 14 mm and the wall thickness d is 1.4 mm. For a comparison between the two calculation methods, the results of the BEM are also given at several positions.
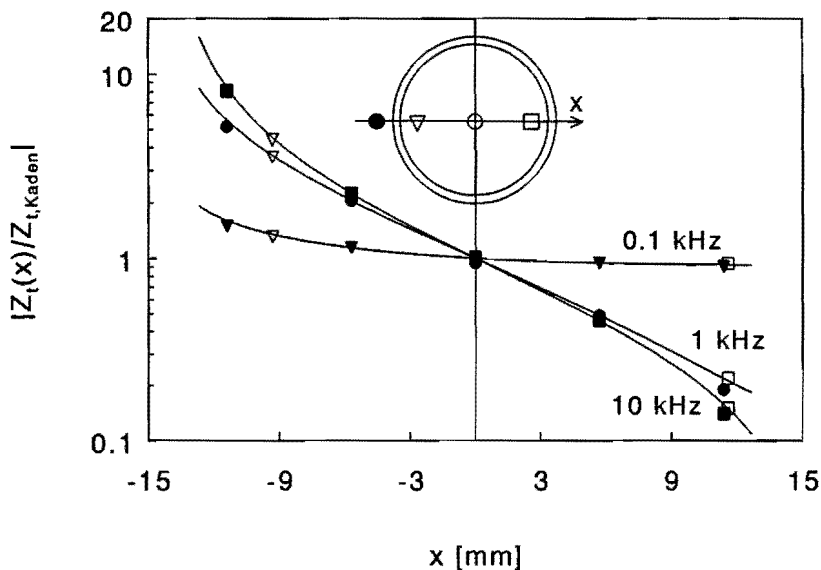
Fig. 3.7: The transfer impedance, divided by the Kaden value (Eq. 2.18), as function of the position of the inner conductor along the line (x-axis) through the center of the tube and the return conductor. The lines have been calculated with the Multipole Expansion method and the filled markers are obtained by the Boundary Element Method. The open markers are measurement results.

When the return wire is placed at 17.1 cm from the tube wall, the current distribution becomes already quite symmetric. The maximum difference (at 3 kHz) between the measured Z_t and Eq. 2.18 is about 20 percent. This dependence on the distance is also born out by the ME calculations.

3.3.2 Slotted tube

Up to 30 kHz the measurement results of the slotted tube (Fig. 3.4) coincide with the results of the closed tube (Fig. 3.3), so the ME method is also applicable in this case. When the return wire and slot are opposite to each other, which means at positions $(2a, \pi)$ and $(r_1, 0)$ respectively, the magnetic coupling through the slot is even negligible for the positions (r, π), $(r, \pi/2)$ and $(0, 0)$ of the inner conductor
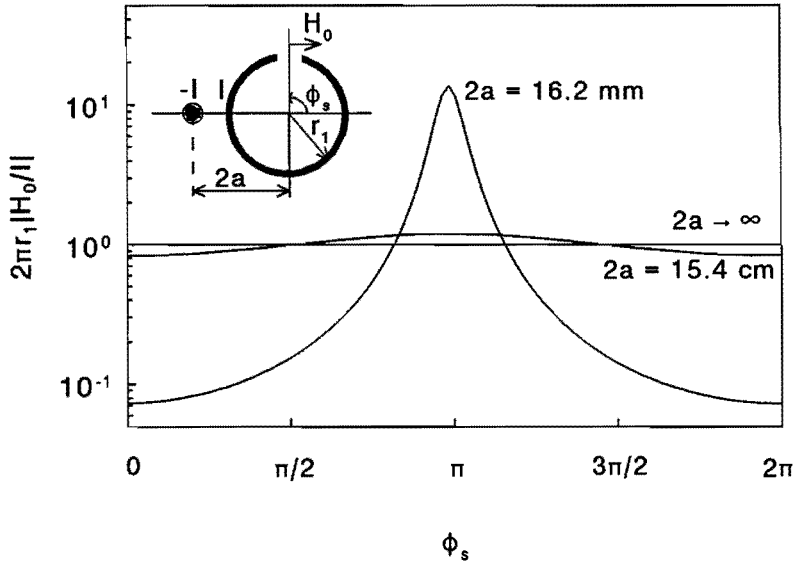
Fig. 3.8: The magnetic field H_0 along the circumference of a tube with an outer radius r_1 of 14 mm. The return conductor is positioned at a distance of $2a$ of the center of the tube as indicated in the insert. The magnetic field is divided by $I/2\pi r_1$, where I is the current which flows through the tube and returns via the wire. The frequency is 10 MHz.
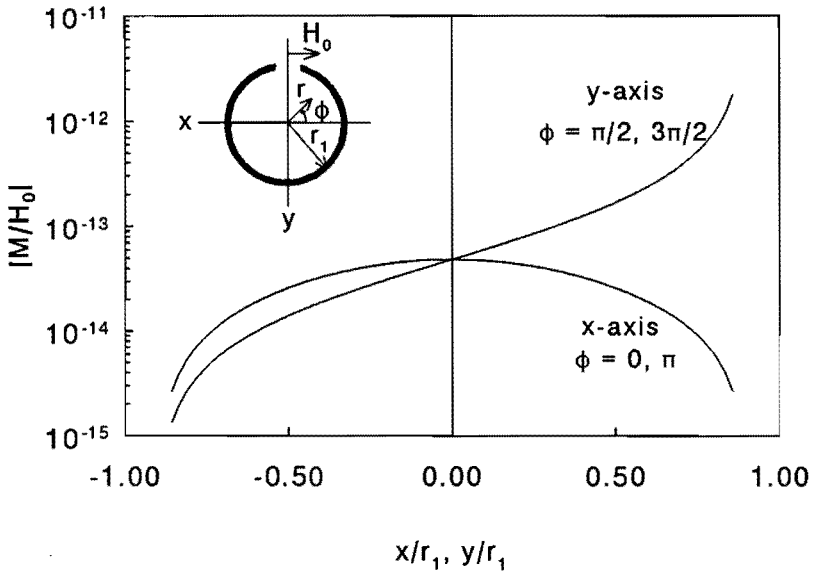
Fig. 3.9: The mutual inductance contribution M_{slot} to the transfer impedance, due to the coupling of the magnetic field H_0 above the slot. The position of the inner conductor (1) is varied along the x- and y-axis. The radius of the tube is $r_1 = 14$ mm, its wall thickness is $d = 1.4$ mm. The frequency is 10 MHz.

up to 100 kHz. For these three cases r, d and σ have been used as parameters in a fit to the ME calculation. The average values, together with the other parameters used in the calculations, are given in Table 3.3.

parameter	r_1 (mm)	$2a$ (mm)	r (mm)	d (mm)	σ $(10^7\,\Omega^{-1}\,\mathrm{m}^{-1})$
value	14	16.2	11.5	1.33	5.08

Table 3.3: The parameters used in the calculations on the slotted tubes.

The inductive coupling through the slot can be described with a mutual inductance term M_{slot} in Z_t. For high frequencies $(d > \delta)$ M_{slot} can be calculated following the guidelines given in [Kad 59]. First the magnetic field H_0 above the slot is calculated, using the image principle for the nearby return conductor. Then the magnetic field inside the tube, due to the penetration through the slot, is described with a fictitious line dipole in the slot. The amplitude of this dipole is proportional to H_0. More details are given in Appendix A.2 where M_{slot} is calculated for arbitrary positions, with respect to the return conductor, the inner conductor and the slot.

In Fig. 3.8 the variation of H_0 over the circumference of the tube is shown for three distances of the return conductor ($2a = 16.2$ mm, $2a = 15.4$ cm and $2a \rightarrow \infty$). When $2a$ goes to infinity H_0 simplifies to the well known expression $I/(2\pi r_1)$. The latter expression remains a good approximation for relatively small a; for $2a > 15.4$ cm the maximum deviation is smaller than 20 %. For $2a = 16.2$ mm H_0 varies a factor 100 along the circumference. When $2a$ approximates r_1, H_0 varies between 0 and ∞ along the circumference. In Fig. 3.9 M_{slot}, divided by H_0, is given for several positions of the inner conductor on either the x-axis or the y-axis. Here M_{slot} varies with a factor 1000. The frequency used for the calculations in both figures is 10 MHz. The deviation, up to a factor 4, between the calculations and measurements (Table 3.1) can be easily explained by the strong dependance of M_{slot} on the dimensions of the slot (App. A.2; Eq. A.27) and the positions of the wires. It is interesting that Griffith, who used test samples of slotted shields with dimensions more similar to actual coaxial cables in a triaxial setup, also reported difficulties to exactly correlate theory and measurement due to uncertainty about the slot width [Gri 71].

In a triaxial setup H_0 would be $I/(2\pi r_1)$. Even for the central position of the inner conductor, M_{slot} measured with the triaxial method or with the wire injection method can show big discrepancies.

3.3.3 Braid

Most braided cable shields consist of two interwoven bundles of helical wires, with opposite pitch. This pitch (about 13 cm for our braid) is usually small compared

to the length of the cable. For our calculations we assume that the currents in the individual wires do not cross over to the neighboring wires. This assumption is made by other authors [Van 75, Tyn 76] and is justified in view of the agreement between the calculations and the measurements reported in this section and in Fig. 3.5. This means, that the braid, possibly due to a large surface resistance of the individual wires [Kei 84, Fig. 1.33, p.33], does not permit the $J_{z,ind}$-current patterns which occur in a tube. Note that this leads to the strong difference between Fig. 3.3 and Fig. 3.5.

Let us first consider a simplified "braid" geometry with a DM circuit consisting of a single helical wire around a central wire, and a CM circuit formed by a single straight wire outside the helix. The vacuum field of the current through the straight wire causes no net flux in this DM circuit for an integer number of pitch lengths. Secondly, also the flux between two parallel helices, shifted over some angle, is zero for an integer number of pitch lengths. If the helical wires are interconnected at either end of the cable, and if the cable is longer than an integer number of pitch lengths, the excess length corresponds to a net induction voltage. This voltage induces circulating currents in between the helices. Also variations in the pitch have the same effect. For our long cable this current is small, as is shown in Fig. 3.5 by the small differences between the Z_t for a far (bold +) and near (o) return conductor, both for a central inner conductor.

For the full braid, the position of the helical wires is changed cyclically. This results in an approximately axially symmetric current distribution, which reduces the flux in the DM circuit, when a CM current is flowing in the braid. Only the inhomogeneities of the braid, such as deviations from the exact helical shape, allow some flux in the DM circuit caused by the CM current in the braid. Consequently, the transfer impedance with the total braid is equal to the DC resistance of the braid until the residual coupling becomes important; in our experiment this occurs above 10 kHz, the corresponding M-value is about 1 nH/m as mentioned before.

Our data for the non-central inner conductor also show that the magnetic field of the nearby return wire is barely reduced by the braid. We calculated the magnetic flux between the displaced inner conductor and the axis due to the vacuum field of the return wire as if the braid was absent. The corresponding M-values result in a Z_t as shown by the dotted lines in Fig. 3.5. Both amplitude and phase agree well with the measured data for both positions indicated by the open triangles ($\triangledown$) and open squares ($\square$). For the third position, indicated by the diamonds ($\diamond$), the calculated M-value is the smallest and depends strongly on the actual position.

In addition to our self made cable also an RG-58/U cable has been tested with the return wire close to its shield. In the frequency range from 5 Hz to 100 kHz the results were identical to those for a far away return conductor. The inner conductor was apparently well centered. Note that with a far away return conductor Z_t for

an RG-58/U cable increases above its DC value only above 1 MHz.

3.4 Conclusion

The dimensions of our test cables were chosen such that the important effects in the transfer impedance could be easily measured in our setup. When actual cables are considered, the same effects will be found at higher frequencies, because the cross-sections of these cables are usually smaller.

The measurements show that the geometry of both the DM and the CM circuit can have a strong effect on Z_t. The central position of the inner conductor of a coaxial cable is of great importance to make Z_t independent of the excitation. The situation changes drastically for less symmetric cables, such as cables with tubular shields and a longitudinal slot, damaged coaxial cables, short sections of cables or multiconductor cables with many non-central conductors, which are not helically twisted. For these cables the transfer impedance measured in a triaxial setup may differ widely from the one observed in actual cable bundles.

Chapter 4

The transfer impedance of non-magnetic cable trays

Cable trays can play a highly useful EMC role, when they are designed to keep interfering voltages picked up by wires and cables in the tray low. The transfer impedance is then of great interest and has been studied both theoretically and experimentally. It turns out that for non-magnetic trays with different geometries and conductivities, the magnetic field at the central line just above the floor of a tray can be represented by a single curve as function of frequency. The same applies to the current density at low frequencies. At high frequencies the current density can be calculated from the magnetic field. A typical curve of the overall Z_t of a cable tray, and its characteristic frequencies, is given in Fig. 4.1. Further the behavior of cables in a tray and the interconnections of trays have been studied.

4.1 Introduction

In the previous chapter the transfer impedance of tubular grounding structures has been studied. Especially the closed wall tubes showed excellent performance. When a large number of cables or wires is involved, pulling the cables through the tubes is cumbersome. It is easier to use metal plates [Gun 86] or cable trays as grounding structures. Trays encountered in industrial surroundings are usually made of steel, but we will first analyze trays made of non-magnetic metal ($\mu_r = 1$). In most practical situations the return conductor of the common mode current through a tray can be considered to be far away. An example of a tray is shown in Fig. 4.2. The cross sections of the trays we used in our experiments are shown in Fig. 4.3. As a voltage sensing wire we utilize a wire above the central line of the tray floor.

For convenience we first briefly discuss the typical Z_t-curve of non-magnetic trays, as depicted in Fig. 4.1 The details will be elaborated later in the subsequent sections. The transfer impedance of the configuration shown in Fig. 4.2 is determined by the electric field ($E_z = J_z/\sigma$) at the floor of the tray and by the flux
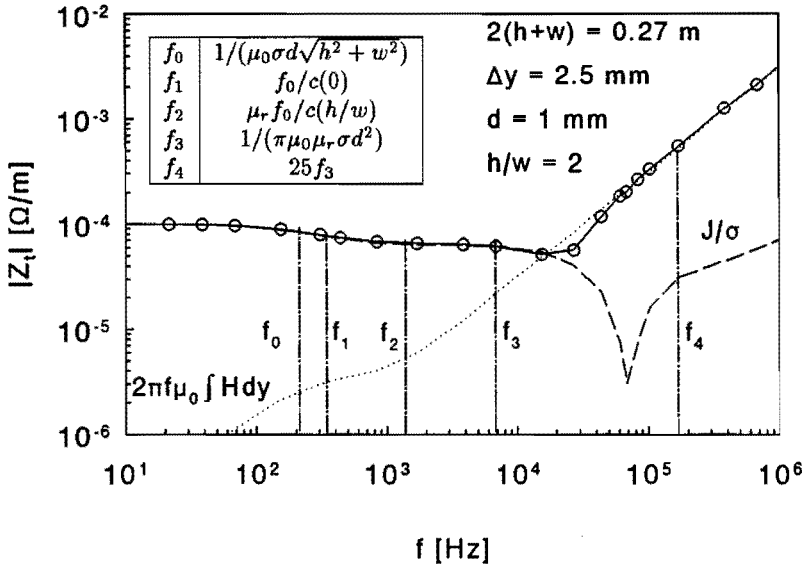
Fig. 4.1: *Typical transfer impedance (Z_t) curve of a non-magnetic cable tray. The specific example shown is calculated for an aluminum tray with $h = 90$ mm and $w = 45$ mm. The measurement lead was placed at 2.5 mm above the floor center (see Fig. 4.2). As in the discussion of the three-lead configuration in Section 2.3 both the current density J and the magnetic field H contribute to Z_t. The current density $J = J_z$ and the magnetic field $H = H_x$ (for $I_{CM} = 1$ A) are obtained from BEM calculations [Oersted] and substituted in Eq. 2.13: dashed line, J/σ; dotted line, $2\pi f \mu_0 \int H \, dy$.*
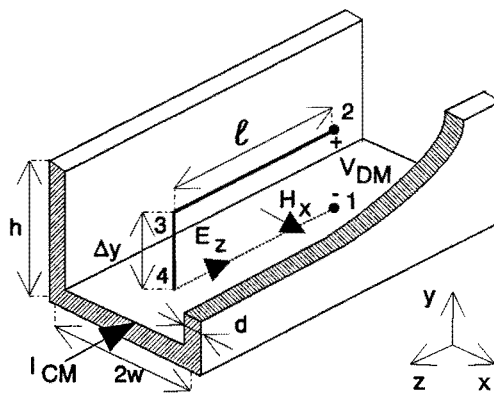
Fig. 4.2: *The common mode current I_{CM} through a tray couples to the interior causing the interference voltage V_{DM} (see Section 2.3).*

h/w = 0   h/w = 1/2   h/w = 2

45 |_____| 90 | |
_____
270   180   90
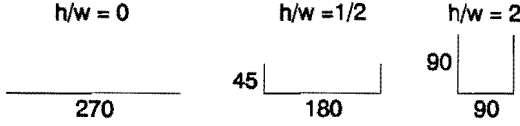
Fig. 4.3: Cross section of three cable trays with $h/w = 0$, $1/2$ and 2 respectively. These specific trays were used in our experiments (Section 4.3). They were created from aluminum ($\sigma = 3.72 \cdot 10^7 \ \Omega^{-1}m^{-1}$) plates with a total width $2(h + w)$ of 270 mm and a thickness d of 1 mm. In Chapter 5 similar trays made of steel are studied.

($\mu_0 \int H_x \, dy$) through the loop formed by the measurement lead and the floor (Section 2.3, Eq. 2.13). At low frequencies, $f < f_0$ (see Fig. 4.1), the contribution of the magnetic field to the transfer impedance is negligible. The current is homogeneously distributed over the tray and Z_t equals the DC-resistance of the tray. Between f_0 and f_1 the current concentrates near the edges of the tray; at the central line J_z decreases. This redistribution of the current also lowers H_x above the central line ($f_0 < f < f_2$). Above f_2 the magnetic field at the central line of the tray becomes constant at its high-frequency value. At higher frequencies the skin depth $\delta = \sqrt{2/\omega\mu\sigma}$ becomes smaller; at f_3 the skin depth δ equals the wall thickness of the tray d and at f_4 the skin depth equals $d/5$. Between f_3 and f_4 the skin effect causes a dip in J_z. In Fig. 4.1 however we can see that this dip is not important to the Z_t curve, because now the flux forms the dominant contribution. Above f_4 also J_z can be calculated with high-frequency approximations.

4.2 Calculations

4.2.1 DC approximation

For low frequencies ($f < f_0$, see Fig. 4.1) the current density in the tray is homogeneous and is determined by the total current I_{CM} through the tray and the area of the cross section of the tray:

$$J_z(x, y) = \frac{I_{CM}}{2(h + w)d} \tag{4.1}$$

The magnetic field at an arbitrary point (x, y) inside the tray can, for non-magnetic materials ($\mu_r = 1$), be determined from a superposition of an infinite number of line currents as is shown in Appendix B.1. From the magnetic field the flux through the loop can be calculated. For a lead at a small height Δy above the center of the floor of the tray, which is at $(x, y) = (0, 0)$, we can simplify:

$$\int_0^{\Delta y} H_{x,DC}(0, y) dy \approx H_{x,DC}(0, 0)\Delta y , \quad \text{for } \Delta y \leq (h + w)/10 \tag{4.2}$$

where $H_{x,DC}(0,0)$ is:

$$H_{x,DC}(0,0) = \frac{I_{CM}}{4(h+w)} \left\{ 1 - \frac{1}{\pi} \ln \left(1 + (h/w)^2 \right) \right\} \tag{4.3}$$

For low frequencies the transfer impedance then becomes:

$$Z_t(0,\Delta y) = \frac{1}{2\sigma(h+w)d} + j\omega \frac{\Delta y}{4(h+w)} \left\{ 1 - \frac{1}{\pi} \ln \left(1 + (h/w)^2 \right) \right\} \tag{4.4}$$

In Fig. 4.1 we see that the contribution of the second term (dotted line) is negligible compared to the first term (dashed line) for $f < f_0$.

4.2.2 High-frequency approximation

At high frequencies the skin depth δ ($= \sqrt{2/\omega\mu\sigma}$) is small compared to the thickness d of the tray. For δ smaller than $d/5$, that is for frequencies $f > f_4 = 25/\pi\mu\sigma d^2$ (see Fig. 4.1) the current density can be approximated by a surface current. To calculate the H-field one then only has to solve Laplace's equation. For positions far away from the upper rim an analytic solution for deep trays is derived in Appendix B.2.1:

$$H_x(x,y) = \frac{\gamma\pi I_{CM}}{2w} \cosh \left(\frac{\pi y}{2w} \right) \cos \left(\frac{\pi x}{2w} \right), \quad \text{for } y \le y_c = h - 0.8w \tag{4.5}$$

where $y = 0$ at the floor of the tray. The constant γ depends on the shape of the tray; when the H-field at a certain point in the tray is known γ can be determined. Van Houten has defined a shape factor g, which represents the ratio of $H_x(0,0)$ in a tray with certain h and w and $H_x(0,0)$ for a flat plate of equal width $2h + 2w$ [Hou 89, Hou 90]. With $H_x(0,0) = I_{CM}/(2\pi(h+w))$ for the plate [Kad 59][1], we find:

$$H_x(0,0) = \frac{g I_{CM}}{2\pi(h+w)} \Leftrightarrow g = \frac{2\pi(h+w)}{I_{CM}} H_x(0,0) \tag{4.6}$$

If we combine Eq. 4.5 (at $x = 0$ and $y = 0$) with Eq. 4.6, we obtain the following relation between γ and g:

$$\frac{\gamma\pi}{2w} = \frac{g}{2\pi(h+w)} \tag{4.7}$$

The magnetic field $H_x(0,0)$ has been calculated for several trays with different height-width ratios. We used a Boundary Element Method, which solved the complete Helmholtz equation, thus taking into account the full eddy current problem [Oersted]. The results compare well to those obtained by two BEM programs which

---

1. Kaden has erroneously omitted a factor $-j$ in his calculations [Kad 59, Eq. B.174, p.62]; his final result $|H_0|$ however is correct [Tin 93].
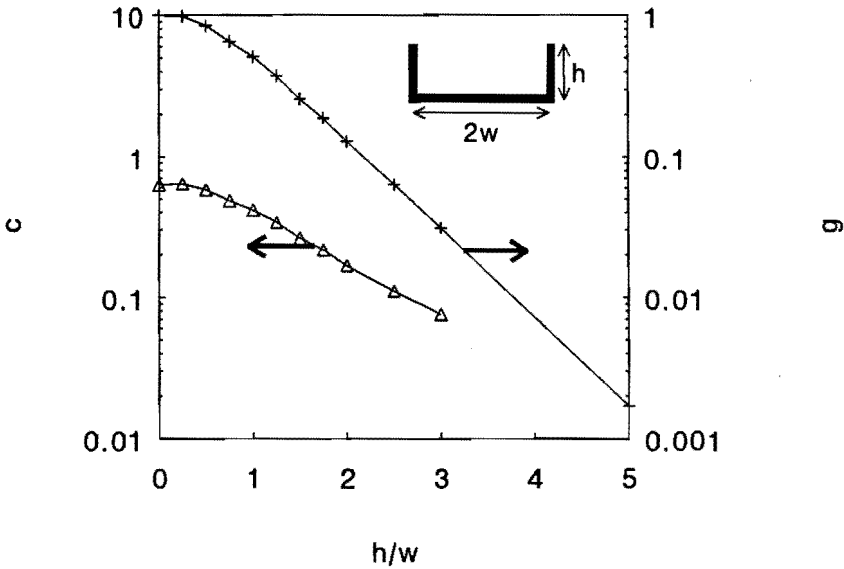
Fig. 4.4: The shape factors g and c as a function of h/w. The shape factor c will discussed in Section 4.2.3 (Eq. 4.17). The shape factor g is defined by Eq. 4.6. For h/w > 1 both g and c decrease almost exponentially. The numerical values are given in Table 4.1.

assume surface currents and solve Laplace's equation [Def 90, Deu 94]. The latter calculations require considerably less computation time, due to the reduction of the complexity. With $H_x(0,0)$ known, γ from Eq. 4.5 and g from Eq. 4.6 are known. Unfortunately the very small fields at the bottom of a very deep tray (for $h/w > 3$) cannot be accurately calculated with the BEM programs. Near the upper rim however the results are more reliable. The constant γ then is determined by a fit of Eq. 4.5 to the BEM H_x-field at e.g. $y = y_c$ (Eq. 4.5), so $H_x(0,0)$ (with Eq. 4.5) and g (with Eq. 4.6) can be calculated. In Fig. 4.4 and Table 4.1 g is given for several height-width ratios.

h/w	g	c	h/w	g	c
0	1	$2/\pi$	1 3/4	0.19	0.22
1/4	0.99	0.64	2	0.13	0.17
1/2	0.84	0.58	2 1/2	0.063	0.11
3/4	0.65	0.48	3	0.031	0.074
1	0.51	0.42	5	0.0017	-0.029
1 1/4	0.37	0.34	10	$9 \cdot 10^{-7}$	$-1 \cdot 10^{-6}$
1 1/2	0.26	0.26			

Table 4.1: The numerical values of the shape factors g(h/w) and c(h/w) as plotted in Fig. 4.4. The shape factor c will be used later in Section 4.2.3 (Eq. 4.17).

For $\delta < d/5$ ($f > f_4$, see Fig. 4.1 and App. B.2.2) the eddy current constant $k = (1+j)/\delta$ relates the current density in a metallic structure to the magnetic field at its surface; $\vec{J} = k(\vec{H} \times \vec{n})$, where $\vec{n}$ is normal to the surface [Bla 85, p.304]. For the floor of a tray one has:

$$J_z(x) = kH_x(x,0) \tag{4.8}$$

Substitution of Eqs. 4.5 and 4.8 in Eq. 2.13 leads to an expression for the Z_t of a *deep* tray as a function of the position in the tray:

$$Z_t(x,y) = \frac{g \cos\left(\frac{\pi x}{2w}\right)\left\{\frac{k}{\sigma} + j\omega\mu_0\frac{2w}{\pi}\sinh\left(\frac{\pi y}{2w}\right)\right\}}{2\pi(h+w)} \tag{4.9}$$

Equation 4.9 is valid for $y \leq y_c$, so it is not correct for shallow trays ($h/w \leq 0.8$). In Fig. 4.5 a magnetic field line plot is given around a tray with $h/w = 1/2$, when no cables or leads are present. The surface of the tray is equipotential (see Appendix B.2); the field lines are also lines of constant M.
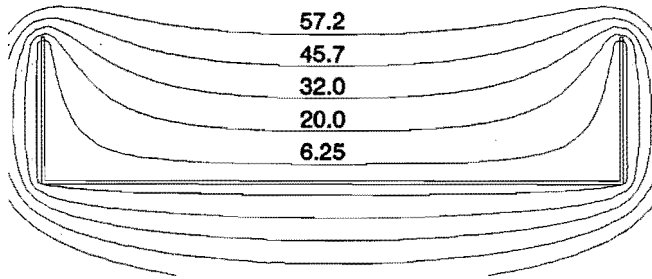
Fig. 4.5: At high frequencies the transfer impedance of a lead in a tray at position (x,y) is dominated by the magnetic flux coupling (M). Here the lines of constant M (in nH/m) around a shallow tray are shown ($h/w = 1/2$, $h = 45$ mm, $w = 90$ mm).

In Fig. 4.6 $H_x(x,0)$ is given for several height-width ratios. Figures 4.5 and 4.6 show, that in a *shallow* tray ($h/w \leq 0.8$) H_x can be taken constant for a large region around $(x,y) = (0,0)$, e.g. H_x is constant to within 10% over 50% of the space inside a tray with $h/w = 1/2$. This constant H_x leads to the expression for $Z_t(x,y) = Z_t(\Delta y)$ already given in [Hou 89]:

$$Z_t(\Delta y) = \frac{g\left\{\frac{k}{\sigma} + j\omega\mu_0\Delta y\right\}}{2\pi(h+w)} \tag{4.10}$$

The contribution of k/σ in this equation is negligible for:

$$\omega > \frac{\mu_r}{\mu_0\sigma(\Delta y)^2} \tag{4.11}$$
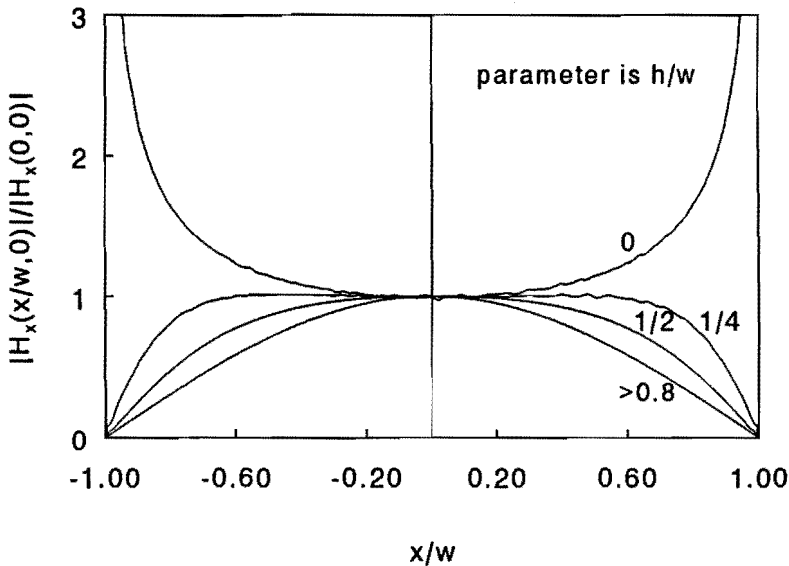
Fig. 4.6: The magnetic field $H_x(x/w, 0)$ at the floor of a tray for four height-width ratios, at high frequencies, divided by $H_x(0,0)$. The magnetic field $H_x(0,0)$ can be calculated with Eq. 4.6 and Table 4.1.

As stated earlier, above Eq. 4.8, also Eq. 4.10 is only valid for $\delta < d/5$ ($f > f_4$) or equivalently $\omega > 50/(\mu_0 \mu_r \sigma d^2)$. The cross-over frequency from Eq. 4.11 is therefore only of interest under the condition $\mu_r/\mu_0 \sigma (\Delta y)^2 > 50/\mu_0 \mu_r \sigma d^2$, or:

$$\Delta y > \mu_r d/7 \tag{4.12}$$

For trays with $\mu_r = 1$ this implies that the k/σ-term in Eqs. 4.9 and 4.10 is not important in practical situations; see Fig. 4.1 for $f > f_4$. Only the induction term in Eq. 4.10 remains:

$$Z_t(\Delta y) = j\omega\mu_0 \frac{g\Delta y}{2\pi(h+w)} \tag{4.13}$$

In Chapter 5 we will discuss the situation that μ_r is not 1.

Equation 4.13 is also convenient for deep trays, when the measurement lead is placed just above the tray floor; when Δy is small, $2w/\pi \sinh(\pi\Delta y/2w)$ in Eq. 4.9 can be approximated by Δy. Note that, in agreement with Fig. 4.6, Z_t is lower for off-center positions ($h/w > 0$).

4.2.3 Frequency dependence

The BEM program [Oersted] has been used to calculate the transfer impedance over a large frequency range for three shapes of cable trays: $h/w = 0$, $1/2$ and 2
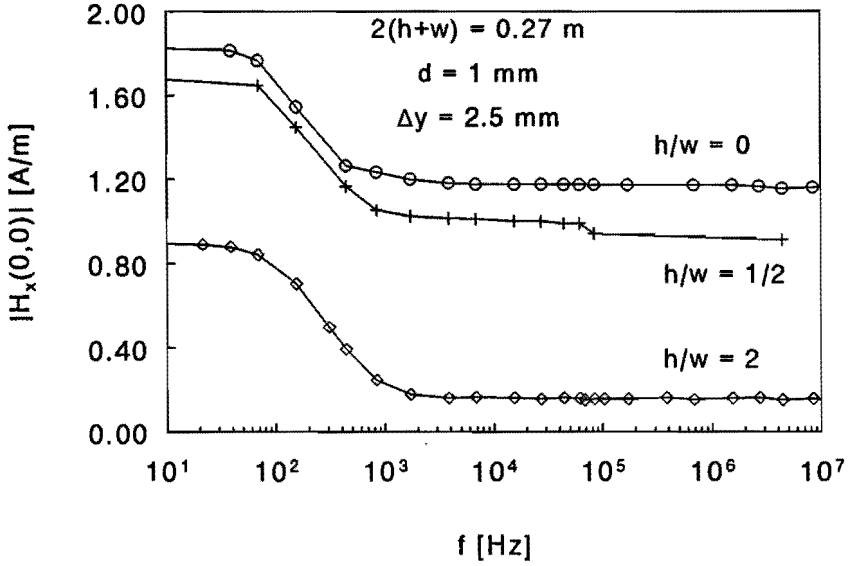
(a)
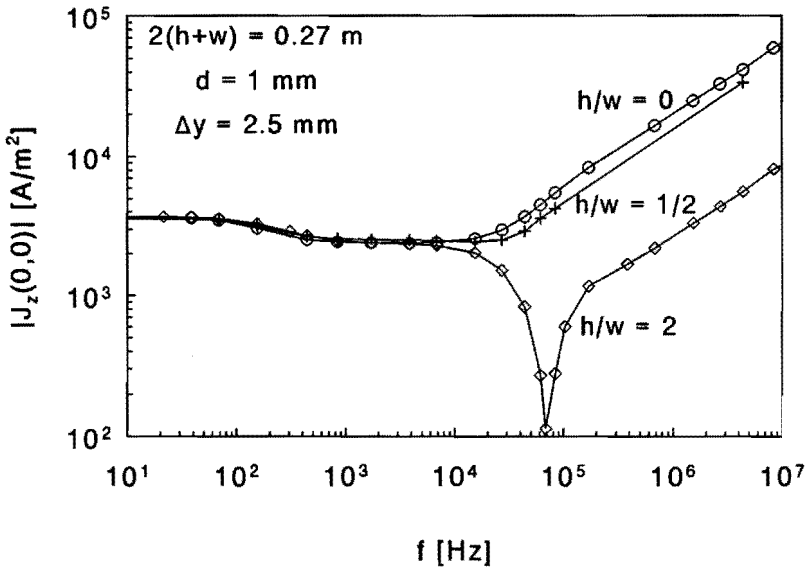
(b)

Fig. 4.7: The magnetic field (a) and the current density (b) at $(x, y) = (0, 0)$ as function of the frequency for $h/w = 0$ (○), $1/2$ (+) and $h/w = 2$ (◇); $\sigma = 3.72 \cdot 10^7 \ \Omega^{-1} m^{-1}$, $I_{CM} = 1A$. The transfer impedance obtained from these BEM calculations is compared with actual measurements in Fig. 4.10 (Section 4.3).

(see Fig. 4.3). The calculated values of H_x and J_z on the central line of the trays $(x, y) = (0, 0)$ have been plotted in Fig. 4.7, as a function of frequency.

For the trays described in Fig. 4.3, Fig. 4.7a shows that the magnetic field $H = H_x(0, 0)$ has two cross-over frequencies; H is constant at its DC value below about 100 Hz, and decreases till about 1 kHz and then becomes constant again. This behavior is found for all examined trays $(0 \le h/w \le 3)$. A good fit to the data turns out to be:

$$H(\omega) = H_{DC} \left(\frac{j\omega\tau_2 + 1}{j\omega\tau_0 + 1} \right) \tag{4.14}$$

where the lower cross-over frequency (f_0 in Fig. 4.1) is determined by τ_0 and the higher cross-over frequency (f_2 in Fig. 4.1) by τ_2:

$$\tau_0 = \mu_0 \sigma d \sqrt{h^2 + w^2} / 2\pi \tag{4.15}$$

$$\tau_2 = |c(h/w)| \tau_0 \tag{4.16}$$

The factor $c(h/w)$ in Eq. 4.16 is the ratio of the high-frequency magnetic field (Eq. 4.6) and the DC field (Eq. 4.3):

$$c(h/w) = \frac{H(\omega \to \infty)}{H(\omega = 0)} = \frac{2}{\pi - \ln(1 + (h/w)^2)} g(h/w) \tag{4.17}$$

For a plate c is $c(0) = 2/\pi$. An overview for other h/w-ratios is given in Table 4.1 and Fig. 4.4. The factor c becomes negative for $h/w \ge \sqrt{e^\pi - 1} = 4.7$; at DC the side walls then contribute more to the magnetic field at the floor than the floor itself.

We checked the fit given by Eq. 4.14 in more detail with BEM calculations for eight different trays in which we varied the following parameters; d (1 mm, 2 mm), h/w (0, 1/2, 2), $2h + 2w$ (30 mm, 270 mm) and σ ($3.72 \cdot 10^6$, $3.72 \cdot 10^7$, $3.72 \cdot 10^8$ $\Omega^{-1} m^{-1}$). All BEM calculations correspond to our model within eight percent. Though a Wilconox signed rank test [Ima 89, p.335] showed that our model is significantly incomplete, for our purposes Eq. 4.14 correctly describes both the amplitude and phase of H. The accuracy is shown in Fig. 4.8 where $|H(\omega) - H(\infty)| / |H(0) - H(\infty)|$ is plotted as function of $\omega\tau_0$. In the same figure the results obtained from BEM calculations on the eight trays are shown after the same transformation.

The description of the current density $J = J_z(0, 0)$ as function of the frequency (plotted in Fig. 4.7b) is more complicated than the description of the magnetic field. We consider three regions, which are separated by $\delta = d$ and $\delta = d/5$ (respectively f_3 and f_4 in Fig. 4.1).

For low frequencies ($\delta > d$, $f < f_3$) a good fit for the current density J turns out to be similar to the fit for H; in Eq. 4.14 H_{DC} must be replaced by J_{DC} and τ_2 by τ_1:

$$J(\omega) = J_{DC} \left(\frac{j\omega\tau_1 + 1}{j\omega\tau_0 + 1} \right), \delta > d \Leftrightarrow \omega < \frac{2}{\mu\sigma d^2} \Leftrightarrow f < f_3 \tag{4.18}$$
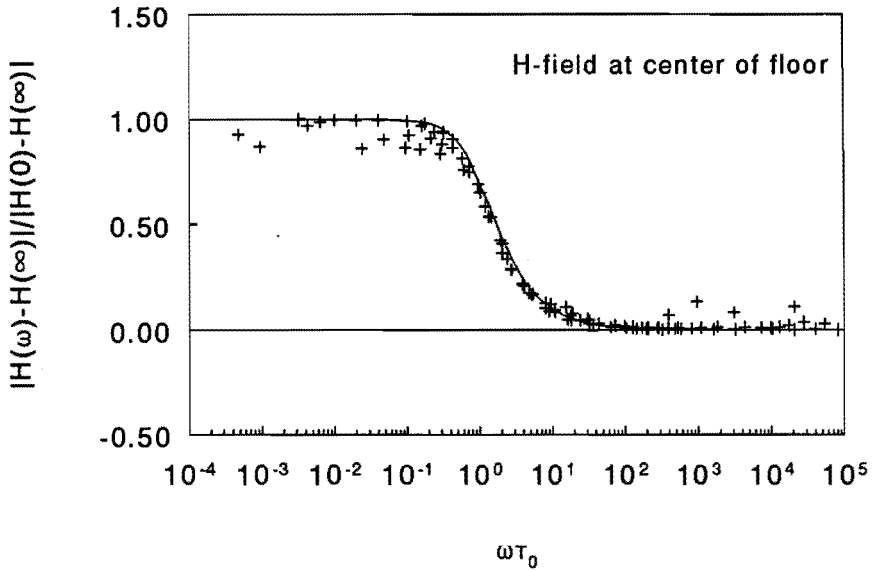
$Fig. 4.8$: Overview of the calculated magnetic field (+) for eight trays after a linear transformation. The relative permeability was 1 in all cases, all other parameters (σ, h, w, $2h + 2w$ and d) were varied. The transformation of Eq. 4.14 (solid line) provides a good fit.

This behavior of J is confirmed by van Horck [Hor 95], who calculated the redistribution of $J_z(x, \omega)$ on a thin plate, where the skin effect in the transverse direction could be neglected. Similar to the curve of $H(\omega)$ the first cross-over frequency (f_0 in Fig. 4.1) is determined by τ_0 (Eq. 4.15). The second cross-over frequency (f_1 in Fig. 4.1) is now determined by τ_1:

$$\tau_1 = c(0)\tau_0 = \frac{2}{\pi}\tau_0 \tag{4.19}$$

The calculations in Fig. 4.7b show that J for $f < f_3$, is independent of the height-width ratio of the tray, thus also τ_1 is independent of this ratio. For a plate τ_1 and τ_2 are equal. For all other shapes τ_1 is larger than τ_2.

In the intermediate frequency range ($f_3 < f < f_4$ in Fig. 4.1), where $d/5 < \delta < d$ or $2/\mu\sigma d^2 < \omega < 50/\mu\sigma d^2$, Fig. 4.7b shows a dip in J especially for deep trays. This is caused by the fact that the local magnetic field on the exterior of the tray is much bigger than the field on the interior; the current density pattern corresponding to the exterior field penetrates and reduces the total current density on the interior. As shown in App. B.2.2 this dip in J can only be fitted by an expression, when both the interior and exterior magnetic fields are known.

When the skin depth is small enough, at about $\delta < d/5$ ($f > f_4$ in Fig. 4.1), the current patterns caused by the interior and exterior magnetic fields no longer

overlap and the inside and outside become decoupled (see App. B.2.2). The current density J is then determined by Eq. 4.8:

$$J(\omega) = kH(\omega) \, , \, \delta < \frac{d}{5} \Leftrightarrow \omega > \frac{50}{\mu\sigma d^2} \Leftrightarrow f > f_4 \qquad (4.20)$$

We have already seen that the mutual inductance term always dominates the transfer impedance for high frequencies $f > f_4$ (see below Eq. 4.12). Also the dip in J between f_3 and f_4 causes the mutual inductance to become dominant (see Fig. 4.1); for the transfer impedance this dip in J is thus less important. Equations 4.14 and 4.18 then can be combined in a single "engineering" expression, which approximates the transfer impedance for shallow trays and for deep trays with the inner conductor close to the floor:

$$Z_t(\omega) = \frac{J_{DC}}{\sigma I_{CM}} \left(\frac{j\omega\tau_1 + 1}{j\omega\tau_0 + 1} \right) + j\omega\mu_0 \Delta y \frac{H_{DC}}{I_{CM}} \left(\frac{j\omega\tau_2 + 1}{j\omega\tau_0 + 1} \right) \qquad (4.21)$$

J_{DC} and H_{DC} are defined by Eqs. 4.1 and 4.3. In Section 4.3, Figs. 4.10 and 4.11, the engineering expression is compared with BEM calculations and measurements. The cross-over frequencies found above are plotted in the transfer impedance curve of Fig. 4.1 and recapitulated in the inserted table.

It is interesting to compare the behavior of trays to that of slotted tubes (Section 3.3.2). In the trays the current is redistributed over its width between f_0 and f_1; at the center the current density decreases and towards the edges it increases (for these low frequencies the transfer impedance in the corners might actually be higher than in the center of the tray). For the tube with a *narrow* slot also a redistribution of the current has been found over its circumference, but the decrease of J at the floor, with the slot at the top ($\phi_s = \pi/2$), is negligible, since the increase at the edges is very local. Therefore the behavior of J in the slotted tubes from Section 3.3.2 remains comparable to that in a solid wall tube. For tubes with wider gaps the redistribution, calculated by Ellis, resembles the redistribution in trays [Ell 71].

4.2.4 Trays with multiple conductors

When conductors are placed inside a cable tray, but are not connected, no net current flows over them. The modification of the magnetic field inside the cable tray by such a conductor then is negligible if the distances between the conductors and between conductors and tray are large compared to the cross section of the conductors. The mutual induction contribution M to the transfer impedance remains the same as determined for a tray with no conductors present. As an example BEM calculations have been performed for three solid conductors (radius 1.75 mm) inside the tray with $h/w = 1/2$. The conductors where placed above the central line

(a)

(b)
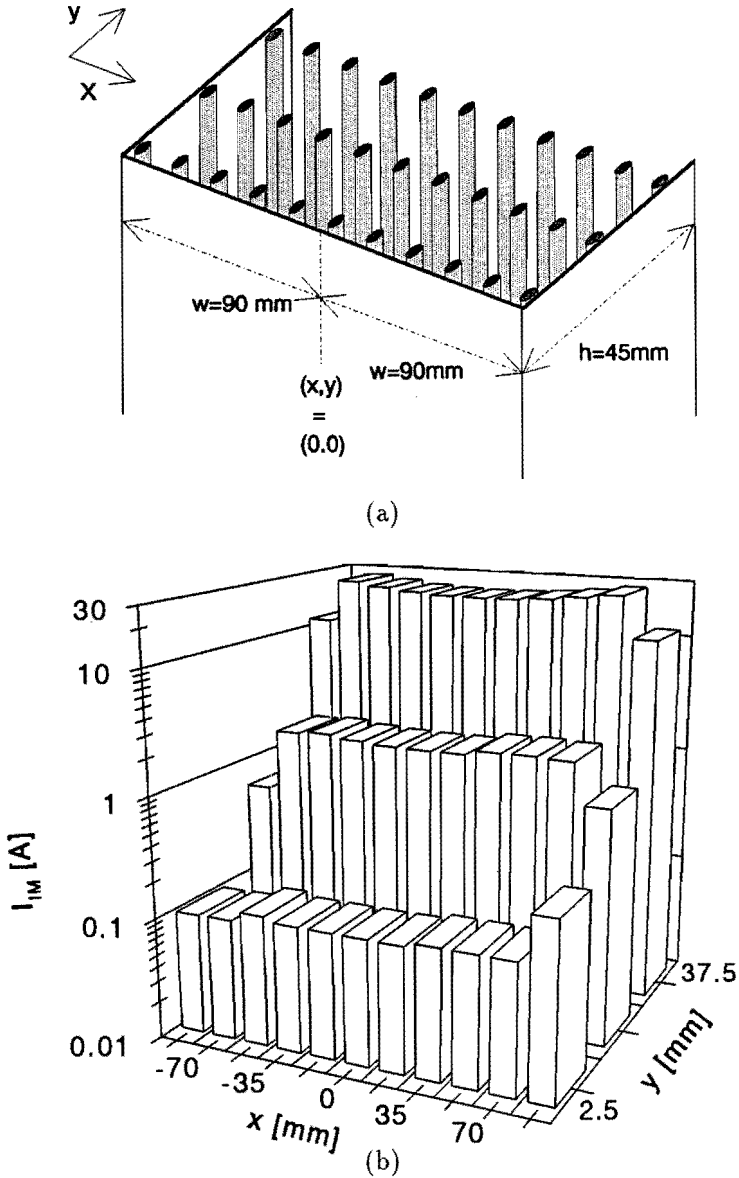
Fig. 4.9: (a) A common mode current of 1 kA is injected over a shallow aluminum tray
(h/w = 1/2) holding 33 grounded solid copper conductors (diameter 3.5 mm). (b) The
current distribution over the 33 conductors at high frequencies (f = 4.4 MHz). For DC
19.7 A flows over each conductor, which is approximately the same as in the top level
for high frequencies. The labels x and y indicate the position of the conductor in the
tray; (x, y) = (0, 0) is at the floor center. Due to numerical problems near the rims the
picture is not completely symmetric around x = 0.

at a height of 2.5 mm, 20 mm and 37.5 mm. For the lowest position the distance between the conductor and the tray is not large compared to the cross section of the conductor. The calculated M with the conductor present is 30 % lower than the corresponding value for a very thin conductor. When the solid conductor is replaced by a woven braid, the difference should be less, because the magnetic field can penetrate through the braid (Chapter 3). When the other two positions for the solid conductors are compared to the situation without conductors the differences are less than 2 %. If more conductors are present and the distances are small in comparison to the cross section of the conductors M is lowered, so the M, calculated with no conductors present, gives a worst case situation.

When the conductors are connected to the tray at both ends, which is for instance the case for correctly installed cable shields, the I_{CM} through the tray causes currents $\vec{I}_{IM}$ in the loops formed by these conductors and the tray (see Section 2.5):

$$\vec{I}_{IM} = [Z_{IM}]^{-1}[Z_{t,tray}]I_{CM} \qquad (4.22)$$

$[Z_{IM}]$ is the $N \times N$ impedance matrix of the N conductors with the tray as reference and also includes their mutual coupling. The $N \times 1$ matrix $[Z_{t,tray}]$ describes the coupling between each of the conductors and the I_{CM} through the tray. The net current through the tray is $I_{CM} - \sum_i I_{IM,i}$.

As an example the current distribution in 33 grounded solid conductors in the same tray as above is given in Fig. 4.9. The CM current is 1 kA and the net current over the tray itself is 0.76 kA. The currents over the conductors in the middle level ($y = 20$ mm) are about 10 times lower and the currents at the lowest level ($y = 2.5$ mm) are about 200 times lower than the currents in the upper level ($y = 37.5$ mm). Over the conductor, which is placed at 2.5 mm above the floor center flows about 0.1 A, while in the situation that the other conductors are not present 6 A flows over it. It is clear, that, at high frequencies, the upper conductors ($y = 37.5$ mm) effectively protect the underlying layers. When these conductors are replaced by cables, the voltages $\vec{V}_{DM}$ at the end of the individual cables can be calculated with $\vec{V}_{DM} = [Z_{t,cable}]\vec{I}_{IM}$ (Eq. 2.26). If the cable shields are braids, the currents at the lowest level may be slightly higher.

From Fig. 4.9 one may conclude, that sensitive cables, meaning cables connected to very sensitive terminals, or cables with a high $Z_{t,cable}$, should be placed at the floor of the tray and less sensitive cables can be placed on top. Of course one should watch that DM-DM cross talk effects between the cables in the tray do not become important. The vicinity of the tray has a beneficial effect on the cross talk, when compared to a cable bundle without tray.
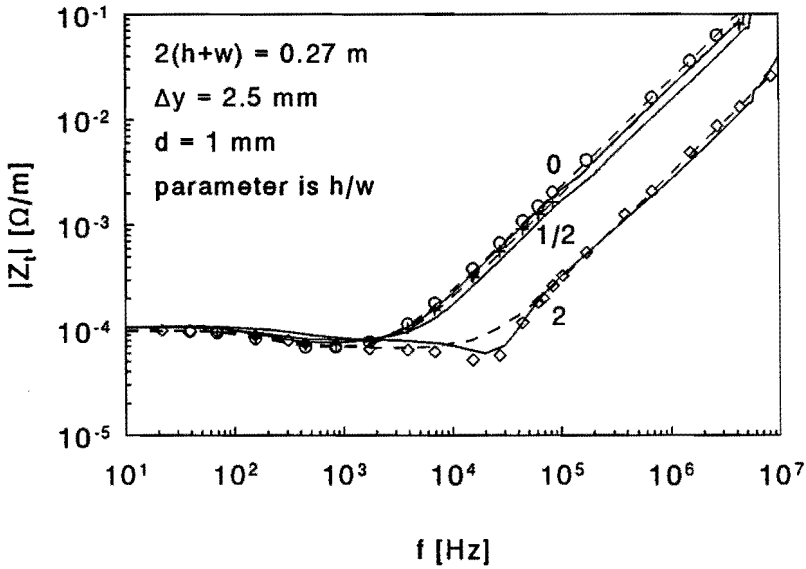
Fig. 4.10: The transfer impedance of aluminum trays with h/w as indicated. The measuring lead is at $\Delta y = 2.5$ mm above the central line of the tray floor. Solid lines represent measurements, dashed lines the engineering expression (Eq. 4.21) and markers BEM calculations.
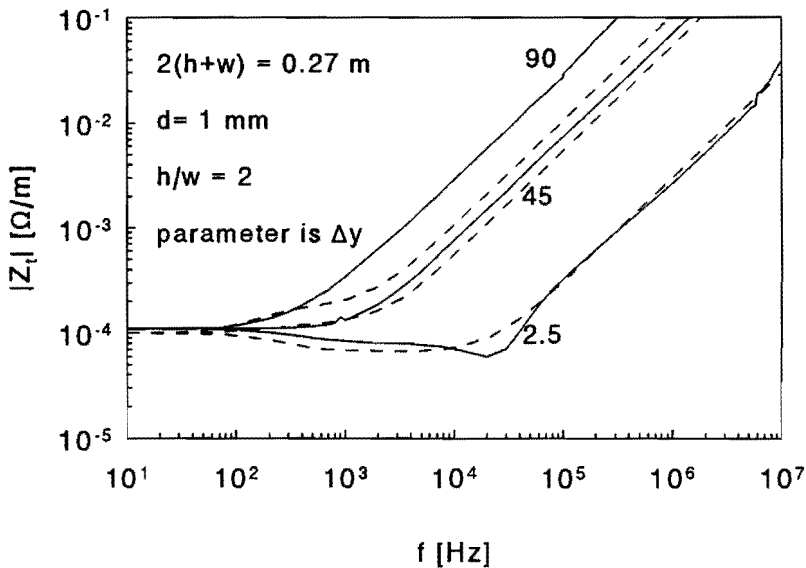

Fig. 4.11: The transfer impedance of an aluminum tray with $h/w = 2$. The measuring leads are at $\Delta y = 2.5$ mm, 45 mm and 90 mm above the central line of the tray floor. Solid lines represent measurements and dashed lines the engineering expression (Eq. 4.21).

4.3 Measurements and comparison with calculations

Home-made aluminum trays with $h/w = 0$, $1/2$ and 2 (see Fig. 4.3) have been investigated with the measurement setup shown in Fig. 2.7b. The length l of the trays was 1.96 m and the total width of the metal $2(h+w)$ was 0.27 m. Figure 4.10 shows the transfer impedance with a measuring lead along the center at a height Δy of 2.5 mm above the floor. The measured data agree to within 20 % with the BEM calculations. Also the engineering expression (Eq. 4.21) shows adequate behavior. At low and at high frequencies it agrees with the BEM calculations within 8 %. For $h/w = 2$ a larger deviation is found at the intermediate frequency range as expected, because the skin effect is not modeled by the engineering expression. Good agreement is also found with the calculations performed by Maciel as is shown by Fig. 2-IV in his thesis [Mac 93], where the results of our mutual methods are compared for one specific tray [Mac 92b]. In Maciel's model the tray is replaced by a set of parallel wires and, as in our engineering expression, he omits the skin effect.

We also measured some transfer impedances for leads in a tray at larger heights above the central line. For the tray with $h/w = 1/2$ and a lead in the uppermost position within the tray ($\Delta y = 42.5$ mm) we found that the transfer impedance calculated with the engineering expression (Eq. 4.21) is 40 % higher than the measured Z_t. For the tray with $h/w = 2$ the measured Z_t is shown in Fig. 4.11 for a single lead at three different heights. The maximum difference between measurement and engineering expression is 25 % for a lead at a height of 45 mm and 60 % for a lead at a height of 90 mm. This difference is easily understood; in the engineering expression the integral over H_x, expressing the flux through the loop formed by lead and tray (see Eq. 2.13), is approximated by $H_x\Delta y$. When the complete integral is calculated by the BEM program, good agreement is found with the measurements. Still, even for leads high in a deep tray the correct order of magnitude of the transfer impedance is found with the engineering expression.

4.3.1 Interconnections

In Section 2.2 we have distinguished two types of transfer impedances. The transfer impedance of cable trays, discussed above, is a distributed parameter, but the transfer impedance of their interconnections and connections to the equipment are local parameters. We studied the transfer impedance of an interconnection between two trays with $h/w = 2$. The length of both trays was 1 m. The lengths of the interconnections were respectively 2 cm and 10 cm, the actual gap between the trays was 1 mm and 8 cm. The different types of interconnections are depicted in Fig. 4.12, their measured (local) transfer impedances are shown in Fig. 4.13. When wires are used as interconnection the local transfer impedance can easily dominate the overall Z_t; for longer wires this was previously already concluded by Maciel [Mac 93]. When 2 cm long connections are considered, the use of two strips
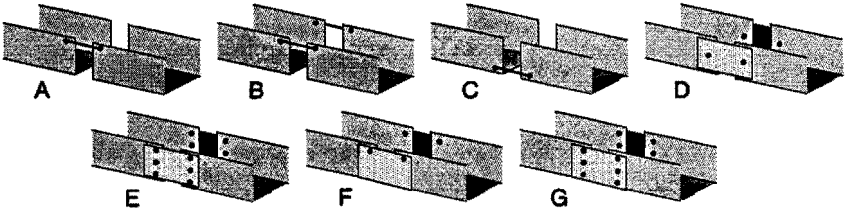
Fig. 4.12: Overview of the examined interconnections between two trays with $h/w = 2$.
A: 1 wire, at one upper rim only; B: 2 wires, at both upper rims; C: 2 wires, at both
edges (only 1 wire shows in the drawing); D: 2 strips, connected with 4 bolts in total; E:
2 strips, connected with 12 bolts in total; F: U-shape, connected with 4 bolts in total; G:
U-shape, connected with 18 bolts in total. We used 2.5 mm^2 copper wires and aluminum
strips with a height of 90 mm (similar to the height of the tray) and a thickness of 1 mm.
The U-shape was similar to the tray, just slightly larger to make it fit.
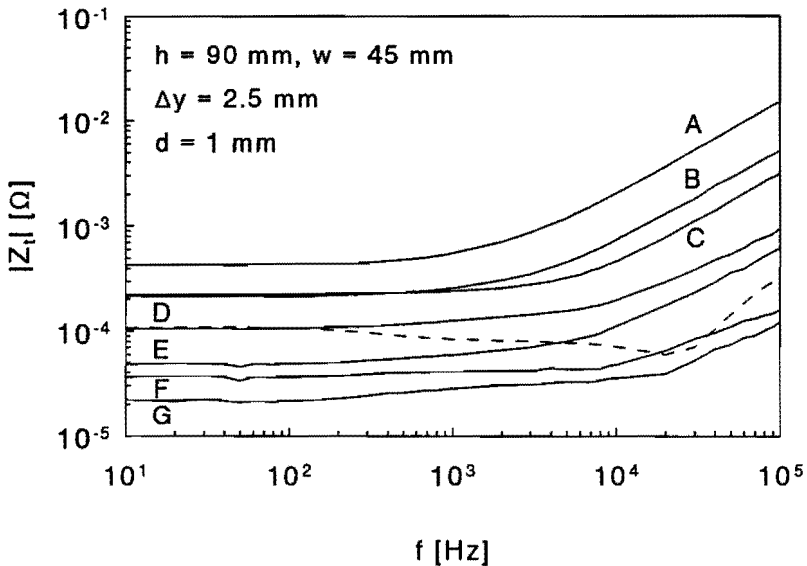
Fig. 4.13: The measured (local) transfer impedance of an interconnection between two
trays. The length of the various types of interconnections was 2 cm, the actual gap
between the trays 1 mm. The letters along the curves indicate the type of interconnection
as shown in Fig. 4.12. The dashed line indicates the transfer impedance of the tray with
$h/w = 2$ for 1 meter length.

on both sides of the tray is acceptable. For the 10 cm long interconnection only the contribution of a U-shaped profile to the total Z_t is negligible. It is interesting to observe that the number of bolts is more important at low frequencies than at high frequencies. The local Z_t was determined by measuring the overall Z_t and subtracting the contribution of the in total 2 meter long tray; the measurements on the connections with a Z_t lower than that of the tray proper are not very accurate, but still give a good indication. When shallower trays are considered the interconnection becomes less important, because the Z_t of the tray itself is higher, especially at high frequencies.

The above considerations are also valid for the connection of a tray to the equipment. Due to the higher Z_t of the tray at higher frequencies, compared to a tube, this connection is less critical than that for the tube from Fig. 2.4.

4.3.2 Cables in a tray

We replaced the measuring lead in the aluminum trays with $h/w = 1/2$ and $h/w = 2$ by an RG-58/U cable, which has a braided shield. Figure 4.14 shows the overall transfer impedance of the combination of tray and cable. The height of the cable was varied; the same positions as for the lead in Fig. 4.11 were chosen. The shield of the cable was connected to the tray at one end and to the EMC-cabinet on the other end (see Section 2.4). The overall Z_t can be calculated with the model described in Section 2.5 and Subsection 4.2.4.

The important parameter we want to calculate is the impedance Z_{IM} of the loop formed by the cable and the tray. First let us consider a solid round conductor (radius r) short-circuited at both ends of the tray. At low frequencies Z_{IM} will be dominated by the impedance of the wire Z_w given by Eq. 2.15. At very high frequencies Z_{IM} will be dominated by the external part of the self inductance L_e of the loop. When the skin depth is small ($\delta \ll \Delta y, d$) and the wire is not too close to the side walls, the tray can be replaced by a metallic half space. With the image principle we obtain [Kad 59, p.69] [Van 78, p.38]:

$$L_e = \frac{\mu_0}{2\pi} \ln \left(\frac{\Delta y + \sqrt{\Delta y^2 - r^2}}{r} \right) \equiv \frac{\mu_0}{2\pi} \operatorname{acosh} \left(\frac{\Delta y}{r} \right) \tag{4.23}$$

At intermediate frequencies also the internal impedance Z_i of the space may become important. Kaden has given an elegant derivation of Z_i based on the dissipated power [Kad 59, p.69]:

$$Z_i = \frac{1 + j}{2\pi \delta \sigma \sqrt{\Delta y^2 - r^2}} \tag{4.24}$$

The total loop impedance is:

$$Z_{IM} = Z_w + Z_i + j\omega L_e \tag{4.25}$$
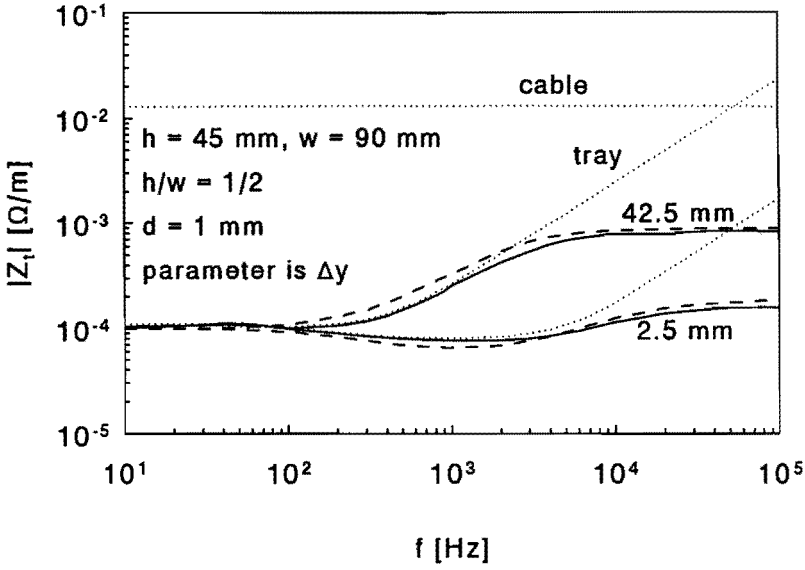
(a)
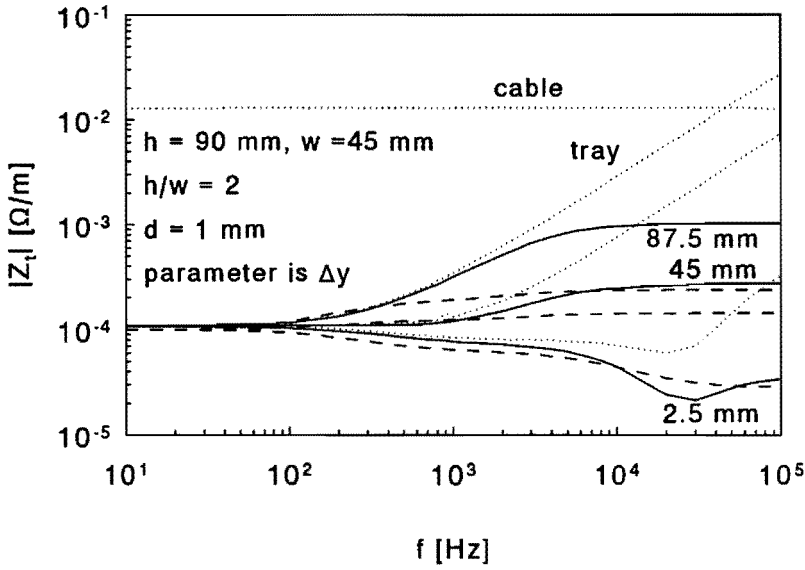
(b)

Fig. 4.14: The measured overall transfer impedance of an RG-58/U cable in an aluminum tray with (a) $h/w = 1/2$ and (b) $h/w = 2$. The height of the cable was varied as indicated in the plot. The solid lines represent the measured total Z_t. The dashed lines are the result from the engineering expression for $Z_{t,tray}$, the analytic expressions for Z_{IM} and the measurement of $Z_{t,cable}$. The dotted lines are the measured transfer impedances of the tray and of the cable proper.

In Appendix B.3 the same expression is derived following the lines given by Carson [Car 26]. The latter method is more difficult, but has the advantage that, when more cables are present, also the coupling between the IM loops can be calculated.

Equations 4.23 and 4.24 take into account the proximity effect. In Chapter 3 however we have seen that the magnetic field easily penetrates through a braid, which means that we should not take the proximity effect into account. The current over the cable shield is homogeneously distributed over the strands of the braid. The magnetic field outside the braid, when the metallic half space is not present, can be described by a line current in the braid center. The complete magnetic field, with the metallic half space present, is given by this field plus the field caused by an image of the central line current in the metallic half space. The total flux through the loop formed by shield and half space is found by integrating the first term between the half space and the outside of the braid and the latter term between the half space and braid center. Equations 4.23 and 4.24 then simplify to:

$$L_e = \frac{\mu_0}{2\pi} \ln\left(\frac{2\Delta y}{r}\right) \qquad (4.26)$$

$$Z_i = \frac{1+j}{2\pi\delta\sigma\Delta y} \qquad (4.27)$$

The strands of the braid of the RG-58/U are very thin, so skin effects will only occur at very high frequencies. The internal impedance of the braid will remain the DC-resistance up to high frequencies of the order of 1 MHz: $Z_w = 13$ mΩ/m.

With the previous results we can calculate the overall transfer impedance of the cable in the tray (Eq. 2.25):

$$Z_{t,total} = Z_{t,cable} Z_{t,tray} / (Z_w + Z_i + j\omega L_e) \qquad (4.28)$$

For an RG-58/U the transfer impedance $Z_{t,cable}$ is 13 mΩ/m up to 1 MHz (see Fig. 2.10 for a curve up to 100 kHz), the transfer impedance of the tray $Z_{t,tray}$ can be calculated with the engineering expression (Eq. 4.21) or in the high-frequency approximation with Eq. 4.13. In Fig. 4.14 the engineering expression is used for the calculation of $Z_{t,tray}$. We found good agreement between the calculated and measured overall transfer impedance for tray and cable with $h/w = 1/2$; for Δy = 2.5 mm the deviation is less than 15 %, for $\Delta y = 42.5$ mm the deviation is less than 30 %. Our calculations did not take into account the increase in Z_{IM} and in $Z_{t,cable}$ caused by the connection of the 2 m long tray to the EMC-cabinet via the 30 cm long tube (see Fig. 2.7b); this could easily explain the deviation of 15 % found for the cable at $\Delta y = 2.5$ mm.

For the tray with $h/w = 2$ also good results are found with the cable at a height of 2.5 mm (deviation 18 %), but for the higher positions $\Delta y = 45$ mm and 87.5 mm the measured transfer impedance is 2, respectively 4.4, times higher than calculated. There are two reasons for this. First we already have seen that the transfer
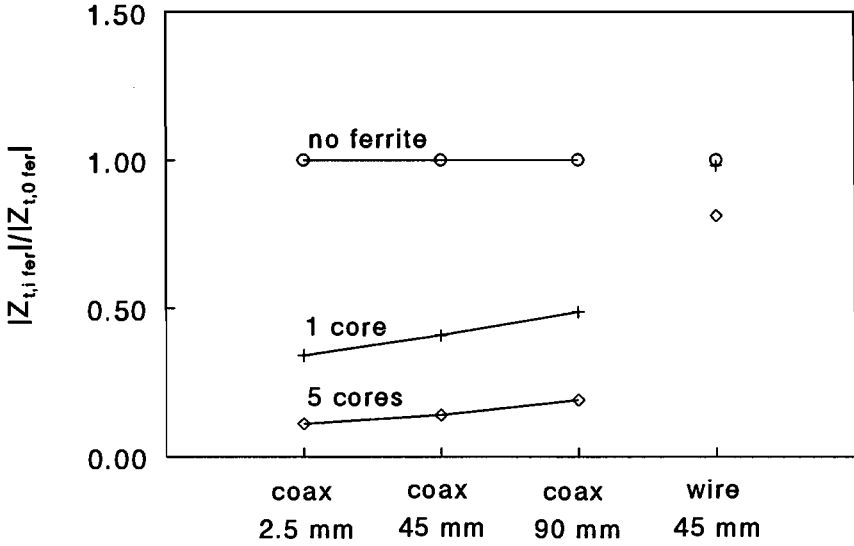
Fig. 4.15: The influence of ferrite in the IM circuit on the overall transfer impedance. The same configuration as in Fig. 4.14b was used. The frequency was 100 kHz.
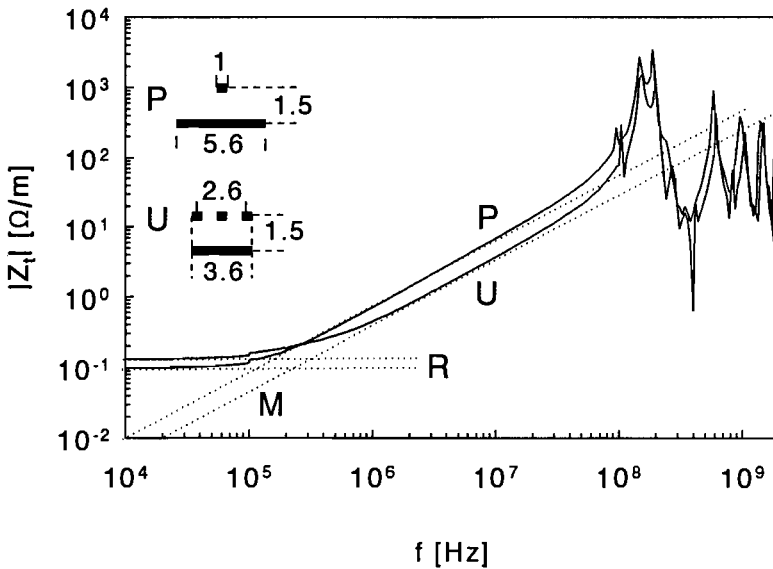
Fig. 4.16: The transfer impedance of a tray-like structure (U) on a printed circuit board, compared with a trace above a small ground plane (P). The total amount of copper in the ground circuit is kept constant.

impedance calculated with the engineering expression is too optimistic (Fig. 4.11). Second the calculations of Z_{IM} are based on a wire above an infinitely large half space. At a height of $\Delta y = 45$ mm the distance to the side walls is the same as the height and we obtained from our measurements that the actual Z_{IM} is lower than expected (see App. B.3). For the highest position this is even worse; Z_{IM} hardly increases between $\Delta y = 45$ mm and 90 mm.

Figure 4.14 shows that the overall transfer impedance of cable and tray at high frequencies increases with increasing height of the cable within the tray. Obviously the mutual inductance term (see Fig. 4.5 or 4.11) in the transfer impedance increases more rapidly with increasing height of the cable, than the self inductance (see Eq. 4.26) of the IM loop.

When more cables with braided shields are mounted inside a tray the considerations given in Subsection 4.2.4 remain valid. The modification of the magnetic field due to the presence of the cables is less than for the solid conductors, because the field penetrates the shields.

4.3.3 Ferrite

For the configurations with the coaxial cables in Fig. 4.14b the influence of ferrite cores (Kitagawa: item nr. TR-28-16-20; o.d. 28 mm; i.d. 16 mm; height 20 mm. Material 3A4: $\mu_{iac} = 800$) was examined. Figure 4.15 shows the results of measurements at 100 kHz.

The use of one ferrite core in the IM loop already gives a big decrease of the overall Z_t, especially for a small IM loop; it then has relatively more influence on the impedance of the loop. The ferrite core should not be introduced in the DM loop; the decrease of the Z_t with one ferrite core is not even significant. Also the application of ferrite in the CM loop is not interesting, because usually this loop is quite large and a lot of ferrite would be necessary to influence the impedance. In addition the CM current might easily be large enough to saturate the ferrite, which causes unwanted non-linear effects, whereas the IM current usually remains much smaller. At low frequencies ferrites are less useful, because the loop impedance is dominated by the resistivity.

4.3.4 Tray-like structures on a printed circuit board

It is possible to position the ground traces on a printed circuit board (PCB) in such a way that the resulting grounding structure looks similar to a U-shaped tray. Compared to a small ground plane with the same amount of copper it has a lower transfer impedance at high frequencies and needs less space on a PCB. The example shown in the inset of Fig. 4.16 has a ratio $h/w = 0.55$. When the results of the real trays also would apply to our "PCB tray", we expect for the shape

factor g a value of about 0.8 (see Table 4.1). The measured value of g however is 0.54; this PCB tray differs too much from our solid wall trays.

The measurement setup is a miniaturized version of Fig. 2.7b. The two-port s-parameter set was used (see Section 2.4). We corrected the measurement for the 50 Ω loading. Up to 100 kHz the transfer impedance of both structures is given by their DC-resistance R, which should be equal for both. Probably due to the production process there is a difference of 34 %. Above 100 kHz the magnetic field coupling M becomes important. The total length of the PCB was 20 cm and above 100 MHz standing waves occur. Transmission line theory has to be applied and it becomes cumbersome to determine the distributed Z_t from measurements.

4.4 Conclusion

The transfer impedance concept has successfully been applied, both theoretically and experimentally, to a large variety of non-magnetic cable trays. At low frequencies the Z_t is dominated by the resistive voltage drop over the tray due to the CM current through the tray. For very low frequencies the current distribution is homogeneous. For higher frequencies the current density increases at the corners of the tray. For still higher frequencies the skin effect occurs and the current flows only at the surface of the tray. However the skin effect is of minor importance for the Z_t of a tray and a simple expression has been found which adequately describes the behavior of the Z_t. For very low and very high frequencies even more accurate expressions have been found for the Z_t as a function of the position of the lead in the tray.

Boundary Element Method calculations and measurements are in good agreement. The transfer impedance, calculated with no conductors present in the tray, gives the worst case situation. When a cable is placed in a shallow tray calculations and measurements agree well. Ferrite rings around a cable in a GS effectively reduce the overall Z_t. We also have shown that interconnections of trays can be made without significantly increasing the overall Z_t.

Chapter 5

The transfer impedance of ferromagnetic grounding structures

Many practical grounding structures are made of steel, which is a ferromagnetic material ($\mu_r \gg 1$). The DC resistance for ferromagnetic materials is usually larger than for non-magnetic materials; at low frequencies the non-magnetic GS's have the lower transfer impedance compared to their ferromagnetic counterparts. However, because the skin effect in ferromagnetic materials already starts at low frequencies, the transfer impedance of completely closed structures (tubes) soon starts to drop. For $\mu_r \gg 1$ also the boundary conditions for the magnetic field have to be adjusted; this alters the magnetic circuit in structures with an airgap. In general the steel GS's then have the higher transfer impedance up to high frequencies. In the high-frequency limit the transfer impedance becomes independent of the material parameters. This is demonstrated for slotted tubes and for cable trays.

5.1 Introduction

In the previous two chapters we have studied the transfer impedance of non-ferromagnetic grounding structures ($\mu_r = 1$). In this chapter we will consider the same grounding structures, now made of steel (St. 37; $\sigma \approx 5 - 10 \cdot 10^6 \, \Omega^{-1} \, \mathrm{m}^{-1}$ [Str 41], $\mu_r \approx 120$, constant over a large frequency range [Bla 85, p.276] [Cow 70]). We consider small currents flowing over the GS's; the analysis will assume linearity. Non-linear phenomena occurring for large currents will be discussed in the next chapter.

5.2 Tubes with a nearby return conductor and a non-central inner conductor

5.2.1 Solid wall tube

In Chapter 3 we have found that the magnetic field caused by a nearby return conductor penetrates into a copper tube and thus adds to the transfer impedance.
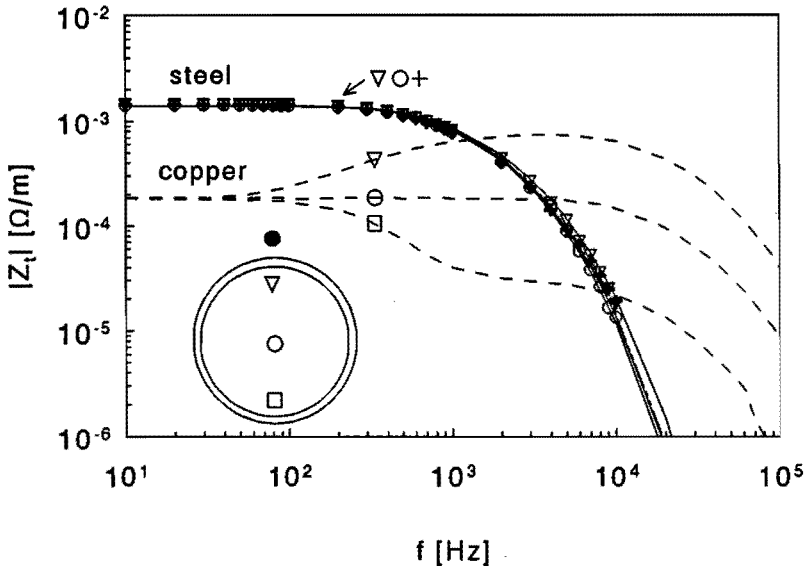
Fig. 5.1: The transfer impedance of a steel tube with a non-central inner conductor and a nearby return conductor. The measurements for steel (markers $\triangledown$, $\circ$ and $+$) coincide with each other; apparently no magnetic field enters the interior of the steel tube. The bold $+$'s indicate measurements with a central inner conductor and a far away return and the solid lines indicate ME-calculations. The dashed lines (configuration marked by $\triangledown$, $\circ$ and $\square$) show the measurement results on a copper tube, which are taken from Fig 3.3.

For steel tubes one expects "magnetostatic" or μ_r-caused shielding, and thus less penetration of the magnetic field. The Multipole Expansion (ME) calculations of Appendix A.1 are valid for an arbitrary permeability. For the limiting case $\mu_r \rightarrow \infty$ one infers from Eqs. A.9, A.13 and A.14 that the magnetic field inside the tube is zero. Also for practical μ_r-values the magnetic field in the interior of the tube is negligibly small. This is shown in Fig. 5.1 by the measurement results on an actual steel tube. The measurements hardly change, when the position of the inner or outer conductor is varied. The deviation from the Kaden expression (Eq. 2.18), which deals only with the effect of the electric field, is negligible. For the ME-calculations one would like to fit three parameters (σ, μ_r and d) to the measured data for the steel tube. Due to the strong interdependence this is quite difficult; the results of the ME-calculations have to be similar to the Kaden expression (Eq. 2.18), which has only two free combinations of parameters (σd and $\sigma \mu_r$). Yet the values given in Table 5.1 seem plausible and lead to good results as is shown in Fig. 5.1.

The steel tube we used in our experiments has the same dimensions as the copper tube of the previous experiments (see Table 3.2).

parameter	r_1 (mm)	$2a$ (mm)	r (mm)	d (mm)	σ $(10^6 \Omega^{-1}\,\mathrm{m}^{-1})$	μ_r
value	14	15	11	1.38	6.49	120

Table 5.1: The parameters used in the calculations on the solid wall steel tube.

It is interesting to compare the transfer impedance of both tubes. At very low frequencies the DC resistance of the tubes is important, which is lower for the copper tube. The skin effect starts to occur earlier with the steel tube because of the larger permeability, thus the exponential decay of Z_t of the steel tube starts earlier and drops below the Z_t of the copper tube between 1 and 10 kHz.

5.2.2 Slotted tube

In Fig. 5.2 the transfer impedance of a slotted steel tube is compared to a similar copper tube. For both tubes the slot width is 2 mm. At low frequencies the Z_t-behavior of the slotted tubes resembles that of the solid wall tubes. For the steel tube the interior magnetic field already becomes important at somewhat higher frequencies; with the inner and return wires at the same position for both tubes, the Z_t of the steel tube is much higher than that of the copper tube.

To measure the interior magnetic field itself, instead of the combination of electric and magnetic field given by the transfer impedance, a 1.5 m long, 12.5 mm high, rectangular loop was placed inside the tube. The sensor plane coincides with the plane through the center of the tube and the slot. The distance between the floor of the loop and the tube wall was 1 mm. The analytic expression for the magnetic field inside the copper tube, which is used in Chapter 3 and derived in App. A.2, is a function of the skin depth δ. Therefore the interior magnetic fields of the steel and copper tubes are most conveniently compared at the same δ. The measured magnetic field inside the steel tube is up to about a factor 100 larger than the measured field inside the copper tube. The measured and the calculated interior field in the copper tube differ at 100 kHz only by a factor 2.5 (the same order has been reported for the difference in the measured and calculated Z_t in Chapter 3, Table. 3.1). Obviously at these frequencies, though $\delta < d$, the analytic expression (Eq. A.26) cannot be used for magnetic materials. This is made plausible, if we consider, that in the copper tube the slot only alters the current distribution, when compared to a closed wall tube, but in the steel tube the slot can be seen as airgap, which strongly alters the magnetic circuit as well.

The lines of magnetic force are inclined to follow the metal with increasing μ_r, due to the changing boundary conditions for the tangential component of the B-field. On the other hand, for high frequencies, eddy currents tend to make any metal free of field; at a constant frequency eddy currents increase with increasing μ_r. This dualistic behavior of magnetic materials has already been observed by Lord
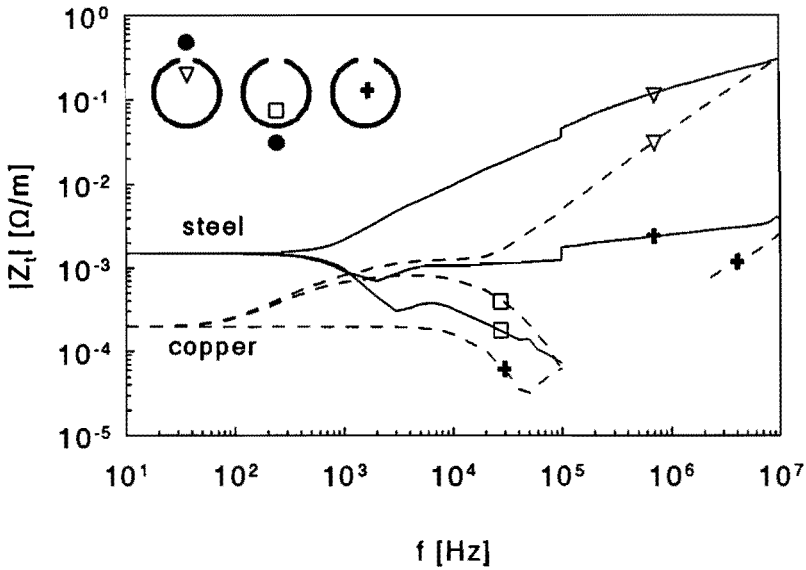
Fig. 5.2: Transfer impedance measurements for a slotted steel tube (b = 2 mm) with a return wire close to the shield; the labels indicate the positions of the slot with respect to the return conductor as shown in the inset. The dashed lines show the measurement results for a copper tube, which are taken from Fig 3.4. The additional curves, labeled by bold +'s, are measured with an axially symmetric current distribution and a central inner conductor. The breaks at 100 kHz and the gaps in some curves above 100 kHz are caused by a change in equipment (see Section 2.4).

Kelvin [Tho 00, p.303]: "In the magnetic problem the iron corresponds to the good conductor, the air to the bad one. When the field is steady the lines of force prefer to take a long path through the iron rather than a short one through the air; they will thus tend to keep within the iron; when however the magnetic field is a very rapidly alternating one, the paths of the lines of force will tend to be as short as possible, whatever the material through which they pass. The lines of force will thus in this case leave the iron and complete their circuit through the air."

Only at very high frequencies the magnetic field becomes independent of the material parameters (see Section 4.2.2). The Z_t's of both tubes then become equal and are dominated by the magnetic field; $Z_t = j\omega M_{slot}$, where M_{slot} now is given by Eq. A.26 and is independent of μ_r as shown by Eq. A.27. Figure 5.2 shows that this occurs only at about 10 MHz.

5.2.3 Slotted tube with copper braid

More expensive cables are often made from a foil with a high permeability, which is covered by a braid. To have a first impression of the behavior of such a cable,

we placed a litze braid around the slotted steel tube; no insulation was put in between. As we saw earlier in Fig. 5.2 the slotted steel tube without a braid has a Z_t larger than the Z_t of the slotted copper tube, except for the measurement position far from the slot between 1 and 100 kHz. For the braided slotted steel tube we obviously find, that the Z_t is lower than for the tube and the braid measured separately. We also find that the Z_t is lower than for the copper tube without braid above about 500 Hz, except for the measurement position close to slot.
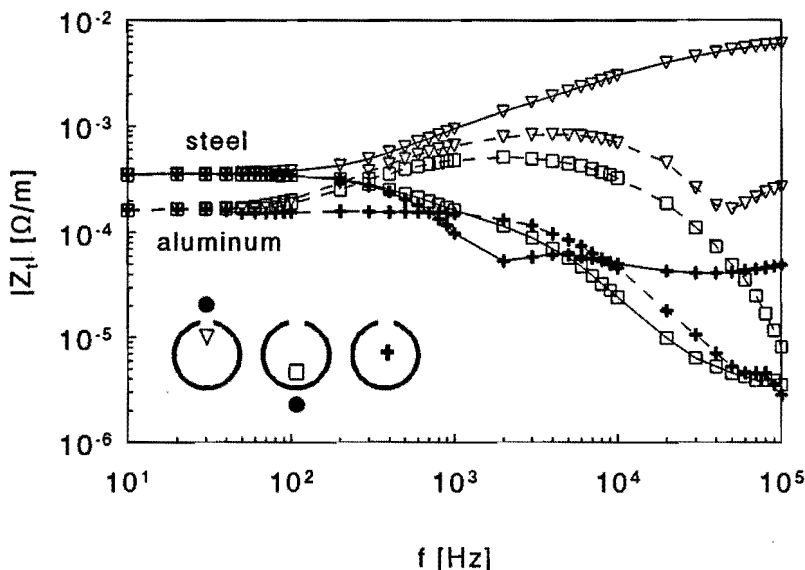
Fig. 5.3: *Transfer impedance measurements for a slotted steel tube ($b = 2$ mm) covered by a litze braid and with a return wire nearby; the markers indicate the positions of the slot with respect to the return conductor as shown in the inset. The bold +'s are measured with an axially symmetric current distribution. The dashed lines show the measurement results for a slotted aluminum tube with a braid.*

It is difficult to maintain the slot width of a copper tube, when it is covered by a braid. From the mechanical point of view this is easier for an aluminum tube. The measurement results of the slotted aluminum and steel tube, both covered by a braid, are compared in Fig. 5.3. It obviously strongly depends on the exact position of the inner and outer conductor and on the frequency which material gives the lower Z_t.

When the slot is made much narrower or even overlapping the results for the braided slotted steel tube will be better; the current is carried by the copper braid and the magnetic field penetrating through the braid is shielded by the steel or μ-metal. It should however be mentioned that the actual behavior of the relative permeability (μ_r) of μ-metal may be different from that of steel [Cow 70].

5.3 Cable trays

5.3.1 BEM calculations

In Chapter 4 the transfer impedance of non-magnetic cable trays has been discussed and especially the engineering expression (Eq. 4.21) is of practical interest. Unfortunately we have found a big difference in the behavior of the steel and copper slotted tubes, thus we have to investigate the validity of the analytic expressions derived in the previous chapter for the case $\mu_r \neq 1$.

In the BEM program the material parameters can be changed easily. We used the same trays as in the previous chapter and we varied only the relative permeability in steps ($\mu_r = 1, 20, 100$ and 1000). The changing boundary conditions for the tangential $\vec{B}$ and the normal $\vec{H}$ will change the field patterns. The calculated values of H_x and J_z on the central line of the trays $(x, y) = (0, 0)$ have been plotted in Fig. 5.4 for $h/w = 0$ and $h/w = 2$ and varying μ_r. In agreement with the experiments of Cowdell [Cow 70] we assumed in our calculations μ_r and σ to be independent of the frequency. In this chapter we also assume both parameters to be independent of the current through the tray.

At DC and very low frequencies, the calculations show that the magnetic field in the center above a plate is barely influenced by variations in μ_r. In Table 5.2 additional calculations at very low frequency are presented. This behavior is in agreement with calculations of Strütt, who has not only given a general approach for calculating the magnetic field inside and outside non-magnetic conductors, as presented in App. B.1, but has also given solutions for the inside fields of ferromagnetic conductors with rectangular, triangular or elliptical cross section [Str 27]. He makes use of the fact that magnetic field lines tend to close inside ferromagnetic materials (see quotation on p. 68 of this thesis [Tho 00, p.303]). With increasing permeability it becomes more and more correct to let the outermost field line inside the metal coincide with the conductor boundary. Mathematically this means that the relative permeability μ_r goes to infinity and the current density J_z goes to 0, while their product, thus also the B-field, remains at a finite magnitude [Hag 62, p.285].

The solution for a rectangular conductor is not very attractive. It is more convenient to consider our thin plate as a thin conductor with elliptical cross section (axis w and $d/2$), analogous to the high frequency approximation from Subsection 4.2.2. The solution is in principle given by Strütt, but elaborated by Hague [Hag 62, p.289]:

$$B_x = +\mu_0\mu_r J_z \frac{w^2 y}{w^2 + (d/2)^2} \tag{5.1}$$

$$B_y = -\mu_0\mu_r J_z \frac{(d/2)^2 x}{w^2 + (d/2)^2} \tag{5.2}$$

If we now suppose μ_r to be finite and substitute a current density J_z equal to $I_{CM}/(2wd)$, we can calculate $\vec{H}$ on the surface, knowing that its tangential component is continuous. At $(x, y) = (0, d/2)$ we find $H_y = 0$ and:

$$H_x \approx \frac{I_{CM}}{4w}, \quad \text{for } d \ll w \tag{5.3}$$

If we compare this expression with Eq. 4.3, with $h = 0$ substituted, we find the same results for a calculation based on $\mu_r = 1$ as for a calculation with starting point $\mu_r = \infty$. Therefore it is reasonable to assume that the tangential H-field at the surface of a plate is independent of the relative permeability, as indicated by the BEM results (Table 5.2).

μ_r	$4(h+w)H_x/I_{CM}$		
	$h/w = 0$	$h/w = 1/2$	$h/w = 2$
1	1.00	0.93	0.48
20	1.00	0.91	0.45
50	–	0.88	0.43
100	1.00	0.87	0.46
250	–	0.88	0.58
500	–	0.92	0.70
1000	–	0.95	0.81
5000	–	–	0.96
10000	1.00	1.00	0.98

Table 5.2: The DC magnetic field ($f = 0.7$ Hz), normalized at $I_{CM}/(4(h+w))$, at the floor center of a tray for various μ_r and h/w. ($2h + 2w = 0.27$ m, $d = 1$ mm).

For a tray two effects are found at DC. In the first place some "shielding" takes place: for a small μ_r (< 200 for $h/w = 2$ and $d = 1$ mm) the H_x-field above the floor decreases very slightly (less than 10 percent). In the second place the magnetic field lines are strongly inclined to follow the metal (as discussed for the slotted tube, p.68). As a consequence of this, the magnetic H_x-field above the floor increases with μ_r, until for a large μ_r (> 2000 for $h/w = 2$) the H_x-field at the inside surface of the tray turns out equal to the H_x-field above the plate. Also for $\mu_r = 100$, $h/w = 2$ and $d = 2$ mm a small increase of the H_x-field has been found; the H_x-field for $d = 2$ mm is 12 percent higher than the field found for $d = 1$ mm.

For $h/w = 1/2$ both mechanisms also occur, but for all μ_r the difference between the field inside the tray and that around the plate, at the center, is less than 15 percent.

The BEM calculations indicate that the magnetic field starts to decrease from its DC value at:

$$f_0 = \frac{1}{2\pi \tau_0} \frac{H_{DC,\mu_r=1}}{H_{DC,\mu_r\neq1}} \tag{5.4}$$
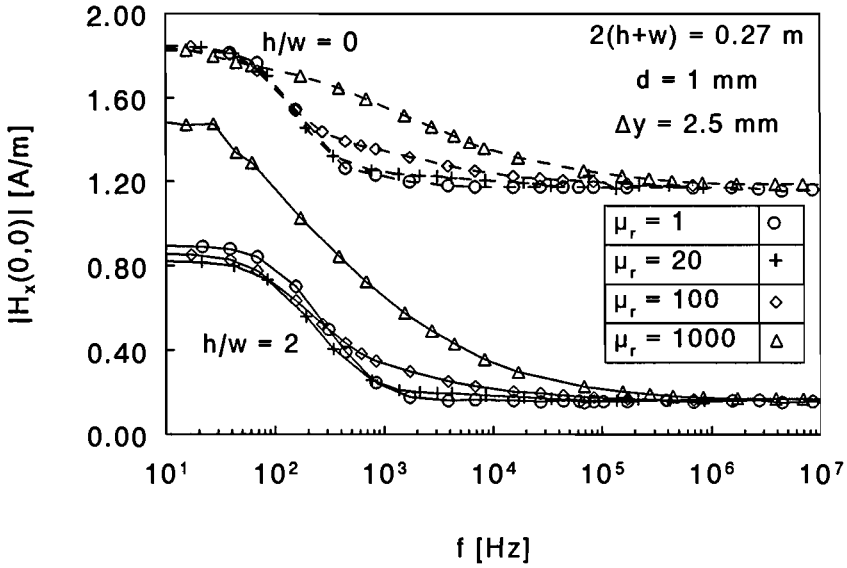
(a)
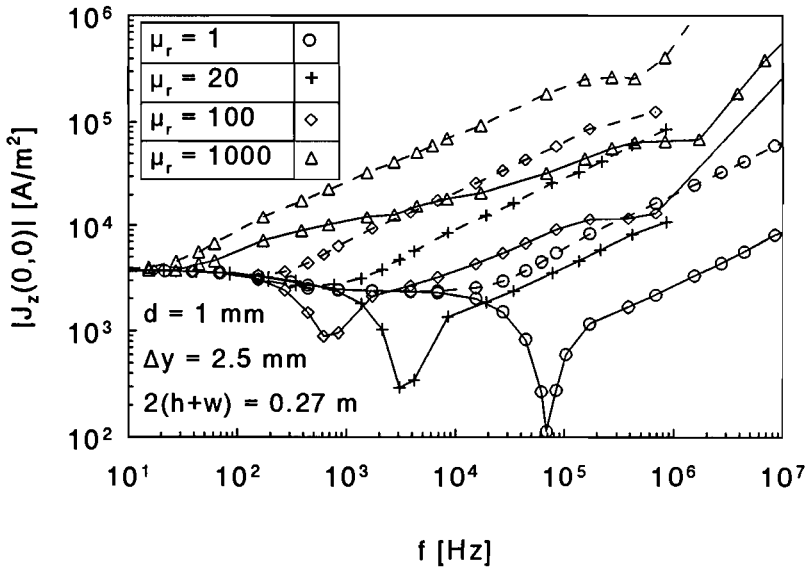
(b)

Fig. 5.4: *The computed magnetic field (a) and the current density (b) at $(x, y) = (0, 0)$ as function of the frequency for a plate ($h/w = 0$; dashed line) and a deep tray ($h/w = 2$; solid line) with μ_r as parameter. ($\sigma = 3.72 \cdot 10^7 \ \Omega^{-1} m^{-1}$, $I_{CM} = 1A$).*

When μ_r is small enough, depending on h/w, a good approximation is $f_0 = 1/(2\pi\tau_0)$, where $\tau_0 = \mu_0\sigma d\sqrt{h^2 + w^2}/2\pi$ (Eq. 4.15).

According to the BEM calculations the magnetic field reaches its high-frequency limit at:

$$f_2 = \frac{\mu_r}{2\pi\tau_2} \tag{5.5}$$

where $\tau_2 = |c(h/w)|\tau_0$ (Eq. 4.16). A similar scaling with μ_r is found for the impedance of a wire above a conducting half plane, which is discussed in App. B.3.

In Table 5.3 the BEM calculations of $H(\omega)$ are compared to the expression obtained for non-magnetic trays (Eq. 4.14). With increasing μ_r, increasing thickness d and increasing depth of the tray the differences between the results of both methods increases. For thin shallow steel trays ($h/w \leq 0.8$), as most frequently encountered in practical situations, the engineering expression for $H(\omega)$ remains quite applicable.

d (mm)	h/w	max. deviation (%)			
		$\mu_r = 1$	$\mu_r = 20$	$\mu_r = 100$	$\mu_r = 1000$
1	0	1.9	4.3	12.0	30.4
1	1/2	1.6	–	15.8	32.6
1	2	7.2	24.6	60.7	198.4
2	0	–	–	16.8	–
2	2	0.8	–	79.8	–

Table 5.3: The maximum deviation between BEM calculations for various μ_r and the expression for $H(\omega)$ from Eq. 4.14 (for $\mu_r = 1$).

For high frequencies ($\delta \ll d$) the current density $J(\omega)$ at the central line can be calculated with Eq. 4.8: $J(\omega) = kH(\omega)$. The eddy current constant k depends on μ_r. The low-frequency behavior ($\delta \geq d$) of $J(\omega)$ is independent of the relative permeability as is shown in Fig. 5.4b; Eqs. 4.18 and 4.20 are valid for all μ_r. No exact expression has been found for the dip in $J(\omega)$ in the region $d \leq \delta \leq d/5$, because in this case the high-frequency limit $f > f_2$ is still not reached and no exact expression for $H(\omega)$ has been found for deep trays. The dip becomes less pronounced with increasing μ_r or decreasing depth of the tray; in other words the difference between interior and exterior H-field then become less (see App. B.2.2).

The BEM calculations further resulted in several empirical scaling laws for trays, which hold for general μ_r:

1. The curves of H and J are primarily a function of $\omega\sigma$; the transfer impedance of trays with the same shape and permeability, but with different conductivity, can be obtained from the results for one conductivity, e.g. those of Fig 5.4. In App. B.3 similar results have been obtained for the impedance of a wire above a ground plane;
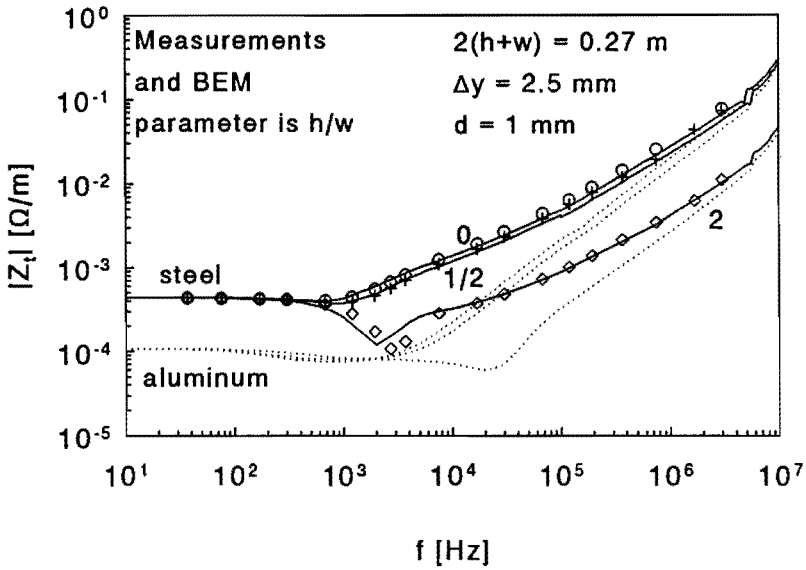
(a)
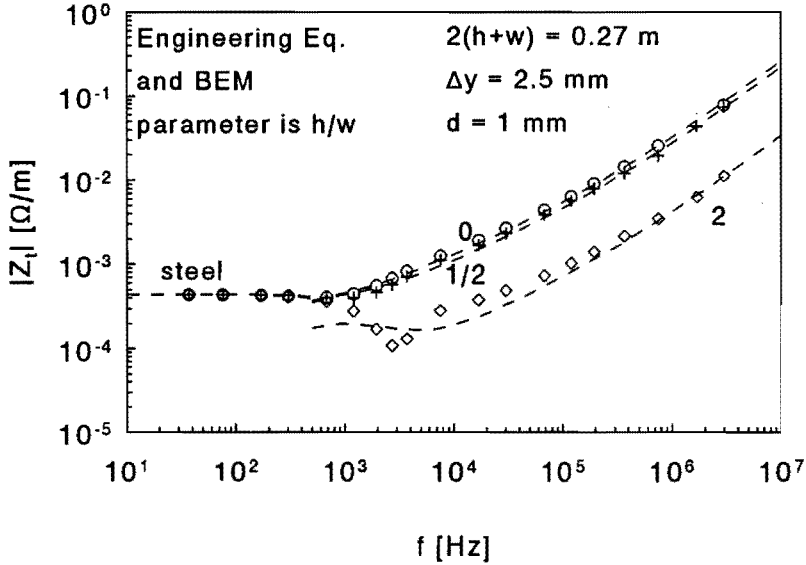
(b)

Fig. 5.5: The transfer impedance of steel trays with h/w equal to either 0, 1/2 or 2. The measuring lead is at $\Delta y = 2.5$ mm above the floor center of the conduit. Solid lines represent measurements, dashed lines the engineering expression for steel (Eq. 5.6) and markers BEM calculations. The dotted lines are the measurements on aluminum trays taken from Fig. 4.10.

2.   When we vary f, d and $h + w$ at constant $h/w, \sigma$ and μ_r, a single curve is obtained for the magnetic field as function of the frequency when $(h + w)H$ is plotted against $\omega d \sqrt{h^2 + w^2}$. This result is similar to Eq. 4.14, but more general;

3.   Another single curve can be obtained for $d(h+w)J$ plotted against $\omega d \sqrt{h^2 + w^2}$ (Eq. 4.18). This plot is only valid for low frequencies $(d \leq \delta)$;

4.   For high frequencies $(\delta \leq d/5)$, the scaling laws for H also apply to J, since the current density then can be calculated from the interior H-field (Eq. 4.20).

5.3.2 Comparison between measurements and calculations

For the measurements home-made steel trays were used with the same cross sections and lengths as the aluminum trays described in Section 4.3. The results of the measurements with a lead in the center of the tray at a height of 2.5 mm are shown in Fig. 5.5a. From the measured DC resistance we obtain a conductivity σ of $8.5 \cdot 10^6 \ \Omega^{-1} \, \mathrm{m}^{-1}$; 30 % higher than found for the steel tubes. After applying the first scaling law, given in the previous section, to the BEM calculations with $\mu_r = 100$ from Fig. 5.4, we found good agreement with the measurements as is shown in Fig. 5.5a. Additional calculations on $h/w = 2$ indicate that μ_r actually has to be between 100 and 200. Therefore the value of $\mu_r = 120$ found for the steel of the tubes also seems applicable to the trays.

Because μ_r is rather low, we can use for shallow trays the general expression for $H(\omega)$ given by Eq. 4.14. The engineering expression for steel trays then becomes:

$$
Z_t(\omega) = \begin{cases} \dfrac{J_{DC}}{\sigma I_{CM}} \left(\dfrac{j\omega\tau_1 + 1}{j\omega\tau_0 + 1} \right) + j\omega\mu_0\Delta y \dfrac{H_{DC}}{I_{CM}} \left(\dfrac{j\omega\tau_2 + 1}{j\omega\tau_0 + 1} \right) & , \omega < \dfrac{4}{\mu_0\mu_r\sigma d^2} \\[4mm] \left(\dfrac{k}{\sigma} + j\omega\mu_0\Delta y \right) \dfrac{H_{DC}}{I_{CM}} \left(\dfrac{j\omega\tau_2 + 1}{j\omega\tau_0 + 1} \right) & , \omega > \dfrac{4}{\mu_0\mu_r\sigma d^2} \end{cases}
$$

$$(5.6)$$

The low-frequency (LF) and high-frequency (HF) branch are continuous, when $\tau_1 \simeq \tau_2$. For 90 % correspondence between τ_1 and τ_2 (Eqs. 4.19 and 4.16) this implies $h/w \leq 1/2$, while for 75 % correspondence $h/w \leq 0.8$ is sufficient[1].

Results of the engineering expression for the three home-made trays are plotted in Fig. 5.5b. For $h/w = 0$ and $1/2$ the LF-branch agrees with the measurements within 3 % and with the scaled BEM calculations $(\mu_r = 100)$ within 0.3 %. The HF-branch is in agreement with the measurements and the scaled BEM calculations within 15 % up to 1 MHz. Above 1 MHz the maximum difference with respect to the measurements is 30 %, because the frequency approaches the first resonance.

---

1. About 60 % of the steel trays offered in commercial catalogues fulfill the requirement of $h/w \leq 0.8$; the percentage of shallow trays encountered in industrial surroundings is probably even higher.
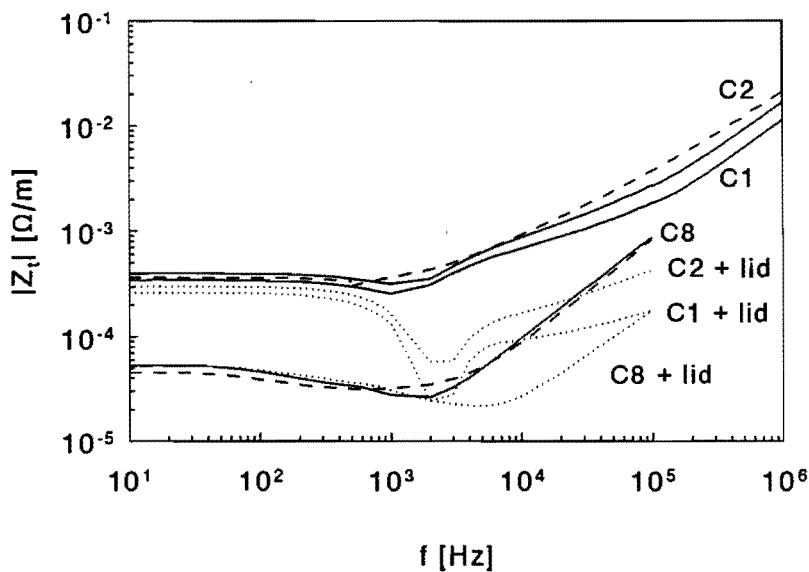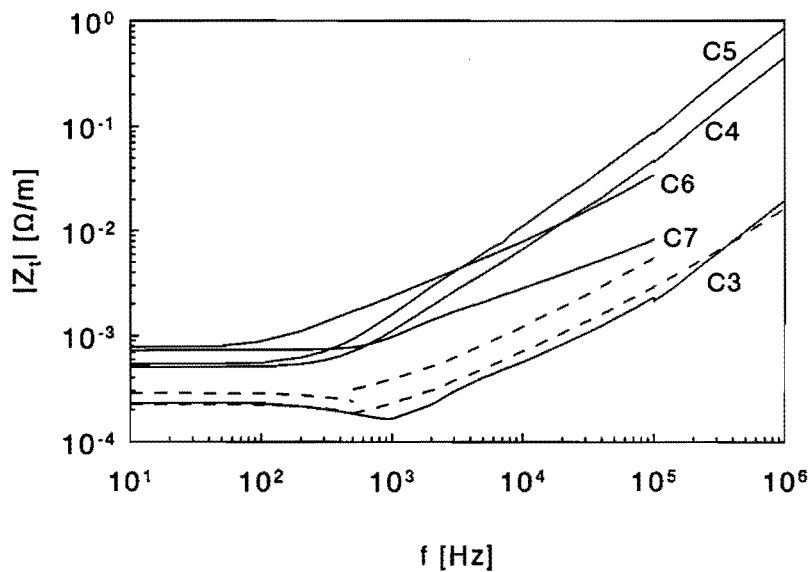
Fig. 5.6: The transfer impedance of some commercially available cable trays, with and without lids. See Table 5.4 for a description. The measuring lead is at $\Delta y = 2.5$ mm above the floor of the tray. Solid lines represent measurements and dashed lines the engineering expression. For trays C4, C5 and C6 the engineering expression is not plotted. The dotted lines in (a) indicate measurements on trays covered with a lid.

As expected for $h/w = 2$ larger deviations are found. The LF-branch of the engineering expression agrees within 10 % with the measurements and within 2 % with the BEM calculations. The deviation between the HF-branch and the measurements and the BEM calculations goes up to a factor 2, because the dip in $J(\omega)$ and $Z_t(\omega)$ is not properly modelled. Also for higher frequencies the deviation is quite large, because of the inappropriate modelling of $H(\omega)$ as is mentioned previously (see Table 5.3).

In contrast to aluminum trays, steel trays do not easily meet the condition $\Delta y > \mu_r d/7$ given by Eq. 4.12, so the frequency above which the magnetic field dominates the electric field in the transfer impedance is given by Eq. 4.11: $\omega > \mu_r/\mu_0\sigma(\Delta y)^2$. The transfer impedance then becomes independent of the material parameters, when $H(\omega)$ is independent of the material parameters. This requires: $\omega > \mu_r/\tau_2$ (Eq. 5.5). Thus "material independence" is found when:

$$\omega > \max\left(\frac{\mu_r}{\mu_0\sigma(\Delta y)^2}, \frac{\mu_r}{\tau_2}\right) \tag{5.7}$$

For the steel trays with a measurement lead at $\Delta y = 2.5$ mm and $h/w = 0$ or $1/2$ the material independence will occur above 286 kHz, for the tray with $h/w = 2$ above 660 kHz. For all frequencies below the high-frequency limit (Eq. 5.7) the aluminum counterparts of the steel trays have the lower Z_t; this is consistent with the results found for the slotted tube.

5.3.3 Commercial trays

Commercially available cable trays are usually made of zinc plated steel. Even painted trays most often have a zinc layer underneath the paint. Therefore it is important to examine whether this zinc layer influences the Z_t. For this purpose we bought a cable tray with a half width $w = 100$ mm, a height $h = 60$ mm and a thickness $d = 1$ mm. We labeled this tray C1. Because $h/w = 0.6 \leq 0.8$, we can compare the measurements with the engineering expression for plain steel trays (Eq. 5.6). We used $\sigma = 8.5 \cdot 10^6 \ \Omega^{-1} \ \text{m}^{-1}$ and $\mu_r = 120$. Figure 5.6 shows acceptable agreement between measurement and expression. The maximum difference is 50 %. The upper edges are bent to the inside. This is not included in our model. Firstly this reduces the field inside the tray. Secondly the plate, resulting when the tray is folded open, is 13 % wider than assumed in our engineering expression. The latter also explains why the measured DC resistance is lower than calculated. An additional effect can be caused by the zinc layer at skin depths (in zinc) of the same order as its thickness[2] (19 μm). The exact geometry was modelled in a BEM

---

2. The galvanizing process used for these trays causes a deposit of 275 g/m² for both sides of a plate (tolerances according to German DVV-standards). With a specific weight of 7.1 g/cm³ for zinc we then find an average thickness of $276/(2 * 7.1 \cdot 10^5) = 19 \ \mu$m.

	h/w	h	$2w$	d	comment
		mm	mm	mm	
H1	0	0	270	1	Plain steel (St. 37), home-made
H2	1/2	45	180	1	Plain steel (St. 37), home-made
H3	2	90	90	1	Plain steel (St. 37), home-made
C1	0.6	60	200	1	Zinc plated steel tray, no perforation
C2	0.6	60	200	1	Zinc plated steel tray, side perforation and ports
C3	0.3	60	400	1	Zinc plated steel tray, side perf. and profile floor
C4	0.6	60	200	1.25	Zinc plated steel ladder, distance of rungs 200 mm
C5	0.3	60	400	1.25	Zinc plated steel ladder, distance of rungs 200 mm
C6	0.62	60	200	4.4	Basket with 10 longitudinal steel wires (od 4.4 mm)
C7	0.1	15	300	1.25	Zinc plated steel tray, transverse perforations
C8	1.36	68	100	2.5	Anodized aluminum tray, for wall mounting

Table 5.4: Description and code names of the examined cable trays. H indicates a home-made tray and C a commercially available one.

calculation where the thin zinc layer had to be omitted. At 100 kHz (for zinc: $\delta \approx 400\mu m$, $\sigma \approx 1.6 \cdot 10^7\ \Omega^{-1}\,m^{-1}$) the BEM result was 2 times higher than the measured value with the zinc layer. At 1 MHz (for zinc: $\delta \approx 125\mu m$) the difference was already reduced to within 13 %.

Often commercial trays are not completely closed, but contain perforations and ports in the floor and side walls. We compared such a tray, labeled C2, with the same dimensions as the previous tray (C1) and found only a small difference (see Fig. 5.6a); the maximum deviation is 30 %; for higher frequencies good agreement is found with the engineering expression. We also compared two shallower trays C3 and C7 to the engineering expression (see Fig. 5.6b). Tray C3 has a corrugated profile floor, however acceptable agreement is found with the engineering expression even if this corrugation is not taken into account. The engineering expression does not apply very well to tray C7, because that tray contains too many holes, so the DC resistance is much higher than calculated by our expression. For higher frequencies the engineering expression gives somewhat better results, but differences remain large. The exact dimensions of the trays are given in Table 5.4.

As an option overlapping lids can be placed on some types of trays. Measurements on C1 and C2 with a steel lid are also shown in Fig 5.6a; the resistive part of Z_t is reduced by a factor 1.3 and the inductive part by a factor 10. We also bought an anodized aluminum cable tray (C8) for our experiments. The oxide layer prevented galvanic contact between tray and lid; only the inductive part of Z_t is reduced by a factor 5. For the aluminum tray without the lid we obtain a maximum deviation of 25 % when compared to the engineering expression (Eq. 4.21), which is quite reasonable, since the inside of the tray is not flat, but contains some longitudinal rims.

Further we examined two cable ladders (C4 and C5) and a cable basket[3] (C6). The measurement results are plotted in Fig. 5.6b. These types have a rather large transfer impedance due to their open structure. We performed no further theoretical analysis. The model used by Maciel is based on parallel wires and should therefore be suited for the basket [Mac 93].

5.3.4 Cables in steel trays

When cables are placed inside the tray with the braid connected at both ends, the overall transfer impedance $Z_{t,total}$ is given by Eq. 2.25:

$$Z_{t,total} = Z_{t,cable} Z_{t,tray} / Z_{IM} \qquad (5.8)$$

Previously we have seen that the transfer impedance is influenced by the changed boundary conditions for $\mu_r > 1$ and that the calculations following the high-frequency approximations of Kaden may deviate strongly from actual measurements on steel trays up to very high frequencies. The same applies to the impedance of the IM loop formed by a cable shield and a ground plane as is shown in Appendix B.3. In general Kaden's expression for Z_{IM} (Eqs. 4.26 and 4.27), used for cables in aluminum trays in Section 4.3.2, is no longer valid and the more difficult method given by Carson [Car 26], and expanded by Wise [Wis 31] for $\mu_r \neq 1$, has to be followed.

In Fig. 5.7 measurements on the overall $Z_{t,total}$ of a steel tray with $h/w = 1/2$ are compared to calculations with Eq. 5.8 in which $Z_{t,tray}$ is obtained with the engineering expression (Eq. 5.6) and Z_{IM} with the Carson method (App. B.3). With the cable at a height of 2.5 mm the maximum difference is about 20 %. At a height of 42.5 mm the maximum difference goes up to 40 %, but this especially occurs at the intermediate frequencies (at about 1 kHz); at low and high frequencies the calculations are quite accurate. It is also important to note that the total transfer impedance measured in aluminum trays is lower than the total transfer impedance measured in identical steel trays up to quite high frequencies; $Z_{t,tray}$ obviously increases more rapidly than Z_{IM} with increasing μ_r. In practical situations the high-frequency limit is determined by $Z_{t,tray}$ and thus can be found with Eq. 5.7.

5.4   Construction elements

Often U, H, I, T or L-shaped beams are used for mechanical constructions. Safety regulations stipulate that such large metal structures must be grounded. The beams may readily be used for EMC purposes as well [Laa 93]. In machines the designers can easily use the construction elements as cable trays. But also steel

---

3. In the Netherlands cable baskets are not very common [Lag 92].
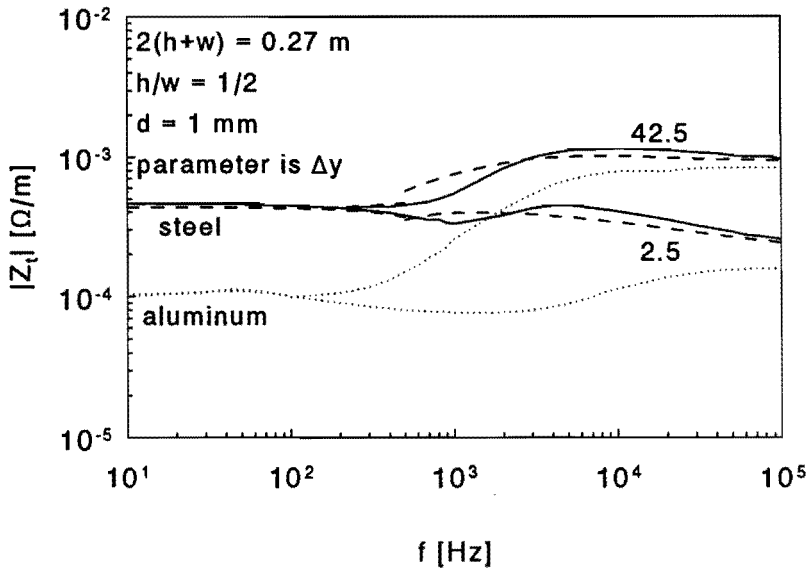
Fig. 5.7: The measured overall transfer impedance of an RG-58/U cable in a steel tray with $h/w = 1/2$. The height of the cable was varied as indicated in the plot (2.5 mm and 42.5 mm). The solid lines represent the measured total Z_t. The dashed lines are the result from the engineering expression and the analytic expressions for Z_{IM} (see App. B.3). The dotted lines show the total measured Z_t for an identical aluminum tray.

constructions used in buildings can be effectively applied, especially when already during the design of the building the electrical installation is taken into account, as is proposed by Stark in the following statement for cabling and wiring in general [Sta 91]: "Electrical installations become more and more important in buildings. Coordinated design of the construction and of the wiring may increase efficiency, building speed and lower the total cost. The economic life expectancy of the main construction is about 60 years, but only 10 years for electric wiring in general and 3 years for information technology applications. When the tie-beams are placed in two layers (e.g. separate layers for beams in north-south and east-west direction), we have the disadvantage that the total building height becomes larger, but the advantage of easier mounting of as well the beams themselves as the wiring."

We can connect the tie-beams with special grounding structures to allow the cables to change direction. Columns can be used to protect cables which connect different floors. Care should be taken when different metals are used, because direct electrical connection is not always allowed in order to prevent corrosion. For EMC this could be a disadvantage. Further one should take care that the cabling does not influence the fire retardation offered by the construction elements.

For four standard construction elements we have used the [Oersted] program to

calculate the high-frequency magnetic field at the center of the floor ($I_{CM} = 1\,\text{A}$). We also determined the DC resistance assuming $\sigma = 10^7 \Omega^{-1}\, m^{-1}$. The results are shown in Table 5.5. In the last column the results of the following equation are shown:

$$H_{HF} = \frac{2g}{\pi O} I_{CM} \tag{5.9}$$

where O stands for the total circumference of the element and g depends on the height-half width ratio (h/w) as shown in Table 4.1. For the U-shaped beam the h/w ratio is obvious. For the H and I shaped beam it is determined by assuming that they consist of two U-shaped beams back to back. The h/w ratio of these U-shaped beams should be used to determine g. Very good agreement is found between this equation and the values obtained by [Oersted]. In fact Eq. 5.9 is a more general form of Eq. 4.6, because for a tray: $O/2 = 2(h + w)$.

shape	type	R_{DC} $\mu\Omega/m$	H_{HF} (Oersted) A/m	H_{HF} (with g) A/m
L	$140 \times 140 \times 15$	25	0.09	–
⊔	UNP 220	27	0.59	0.59
I	IPE 240	26	0.62	0.57
H	HE 160-A	26	0.33	0.33

Table 5.5: The DC resistance and the high-frequency magnetic field at the floor center calculated for some construction elements. The exact dimensions of these construction elements can be found in handbooks, e.g. [MCB 77].

5.5 Conclusion

Ferromagnetic grounding structures which are completely closed have a lower transfer impedance at higher frequencies than non-magnetic GS's, because the skin effect becomes already important at low frequencies. For structures with an airgap the situation changes drastically. Not only the current distribution is altered by the gap, but also the magnetic circuit. Especially the last effect causes a larger interior magnetic field with increasing permeability.

At intermediate frequencies the skin effect is important for ferromagnetic structures with a gap. At very high frequencies the transfer impedance of GS's with an airgap depends only on the magnetic field, which, at these frequencies, is independent of the material parameters. For larger airgaps this occurs at lower frequencies; compare the slotted tubes with the trays and the tray with $h/w = 2$ with the ones with $h/w = 0$ or $1/2$. Further we found that the engineering expression derived for aluminum trays also can be used for shallow steel trays.

Chapter 6

Non-linear behavior of steel cable trays for large Common Mode currents

When large currents flow over steel grounding structures non-linear effects can occur. The description of the coupling from the outside current to the inside voltage via the transfer impedance is then no longer valid. However a first estimate of the induced voltage can be made, if we use the transfer impedance determined for low currents; in our measurements on trays the peak voltages do not exceed these estimated values by more than a factor 5 and that only rarely. Higher harmonics may occur up to high orders.

6.1 Introduction

Large currents may flow over grounding structures during earth fault situations (50 / 60 Hz currents, up to 50 kA in industrial surroundings), switching actions in substations (high-frequency currents, several kA's, see [Wig 94] and Chapter 7) and lightning strikes [Pig 90]. In buildings or large installations, where construction elements are used as trays (Section 5.4), also direct lightning strikes on grounding structures are possible. When steel grounding structures are used, non-linear effects will become important and the voltage v_{dm}, induced inside the tray, cannot be linked to the common mode current via the transfer impedance, but only via a non-linear transfer function; Eq. 2.12, which describes the contributions of the H- and the E-field to $v_{dm}(t)$, however remains valid.

These non-linear effects are caused by the non-linear relation between the B- and H-field in magnetic materials. As an example the static magnetization curve of an iron plate is given in Fig. 6.1. The magnetization curve depends on many factors, such as mechanical history (stress, microstructure [Jil 90], heating) and material composition. For heating this is illustrated in Fig. 6.1 by the difference between an iron plate with and without heat-treatment. The overall behavior of the specific curves in Fig. 6.1 is quite typical for a large range of ferromagnetics. As Fig. 6.1 shows, the relation between B and H is linear for a small H. This relation can

be described with a rather small, constant, initial relative permeability. For larger H-fields B starts to increase more rapidly. In a piecewise linear approximation, the relative permeability also increases. For even higher H-fields, magnetic materials saturate and the magnetization curve becomes almost flat. For iron and steel saturation occurs between $B = 1.6$ T [Kup 73, p.249] [Gor 73, p.17] and $B = 2.1$ T [Ram 84, p.684] [CRC 80].
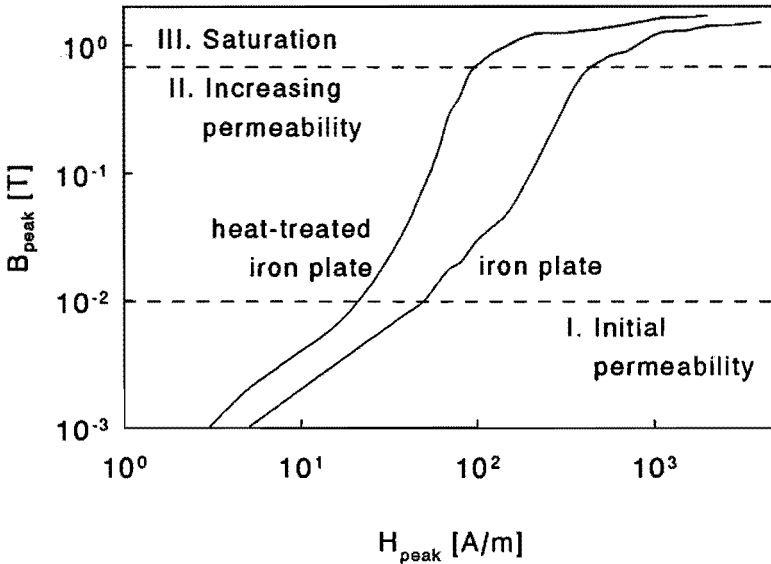
Fig. 6.1: Static magnetization curve of an iron plate, with and without heat treatment. For a small H the B-field can be described with an initial relative permeability (region I). For increasing H the effective permeability B/H increases (region II), until saturation is reached (region III). These data are taken from Küpfmüller [Kup 73, p.249].

The dynamic magnetization curve usually shows hysteresis [Ram 84]. The transfer function therefore will depend on the electrical history and thus on the wave shape of the applied current i_{cm}. We give only a qualitative phenomenological description; a thorough mathematical analysis using e.g. the Preisach theory [May 91] is beyond the purpose of this thesis.

In the literature some work on saturated ferromagnetic tubes can be found, among others Ferber [Fer 70] and Merewether [Mer 70]. Both found that saturation of the tube can reduce the transfer function. To verify this we sent a 1 kA lightning surge current through a steel tube. We used the same setup as for the experiment in Section 2.2, but all measures were taken to minimize the first peak seen in Fig. 2.4. In a control experiment the measurements were repeated on the copper tube. In the time domain it is difficult to identify effects caused by non-linearity for these measurements. Ferber measured the differences in diffusion times. We prefer to

compare a Fourier transform of the measured voltage $V_{DM}(f)$ with the product $Z_t(f)I_{CM}(f)$. This means that the measurement is compared to a calculation under the assumption of linearity. The results are shown in Fig. 6.2. The copper tube behaves linearly and the maximum difference between measurement and calculation is 20 %. The steel tube behaves non-linearly; the measured voltage v_{dm} is up to five times lower than the calculated voltage.
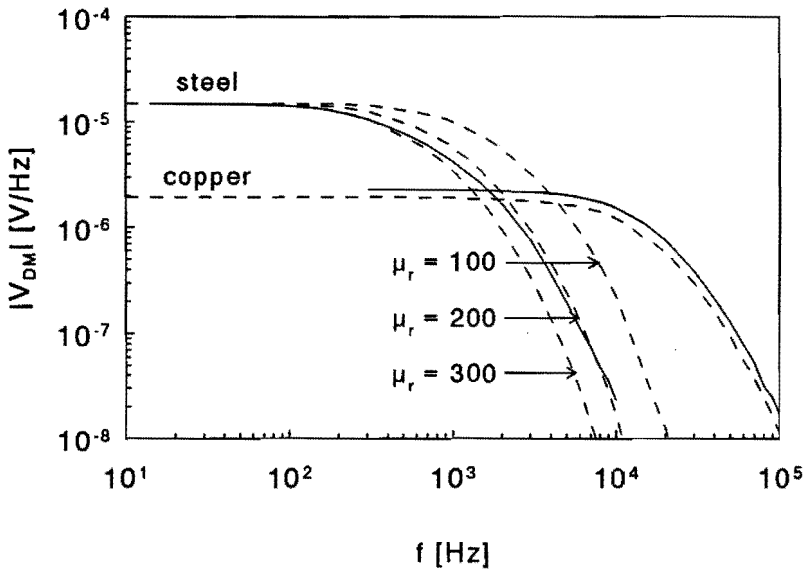
Fig. 6.2: Fourier transform of the DM voltage induced by a lightning surge, with a 1 kA peak value, over a solid copper or a steel tube. The dashed lines show the product $Z_t I_{CM}$, where Z_t is calculated with Eq. 2.18.

For small currents over the steel tube the H-field everywhere in the tube wall remains small and the relation between H and B is given by the initial permeability; for the tube used in this experiment we found $\mu_r = 120$ (see Section 5.2.1). For larger currents H and μ_r increase, until saturation is reached, at first in the outside layer. The magnetic field at the interior of the tube will always remain zero, thus even when saturation takes place on the outside of the wall, μ_r remains at its initial value at the inside of the wall. In between inside and outside there exists a region, which can be identified with a large μ_r. It is interesting to note, that, when $\mu_r = 200$ is substituted in Kaden's expression for the transfer impedance of a tube (Eq. 2.18), good agreement, within 25 %, between measurement and calculation is found. As expected at low frequencies no additional attenuation is observed. These results are consistent with the numerical calculations of Merewether [Mer 70]. Obviously the steel tube provides excellent protection, because in first order the effective μ_r increases for a large i_{cm}.

Contrary to the results of the solid wall tubes a large μ_r is not beneficial for the protection level of a cable tray, as indicated by Fig. 5.4. Effectively such a large μ_r can be expected for a large i_{cm}. The goal of the following measurements is to determine the increase in the transfer function. Trays also provide shielding against external magnetic fields, certainly when made of solid sheet metal. The effects of saturation on the magnetic shielding are not discussed here.

6.2   Experimental setup

Most experiments were carried out with our three home-made steel trays (Fig. 4.3). The results were compared to measurements on their aluminum counterparts, which show linear behavior. This ensures us that any observed non-linearity in the measurements on steel trays is indeed caused by the steel and not by the measurement setup itself. To generalize the results we repeated the experiments with some commercially available trays (see Table 5.4; in the following the addition S means steel and the addition A aluminum). The experimental setup has already been depicted in Fig. 2.7b. To accommodate the large currents and to keep the self inductance of the loop formed by the tray and the return conductor low, a 500 mm wide, 2 mm thick brass plate was placed one meter under the tray. At this distance the perturbation of the current distribution on the tray can be neglected (see Section 2.4). At one end a current source is connected between the tray and the return conductor. The other end of the tray was connected by a copper tube to an EMC-cabinet in which a digital storage oscilloscope was placed. The current i_{cm} was measured by an air-core Rogowski-coil and an active integrator (0.1 Hz - 100 MHz) [Hee 89, Hel 93]. In view of the expected dependence of the transfer function on the wave shape of the current several sources have been used (see Table 6.1).

wave shape	freq. (Hz)	$i_{cm,\text{peak}}$
sine wave, mains	50	10 A – 2 kA
sine wave	250	40 A – 2 kA
sine wave	500	30 A – 1 kA
damped sine wave	$2 \cdot 10^4$	9 kA – 40 kA
damped sine wave	10^6	500 A – 7 kA
0.8 μs/ 8.6 μs pulse		200 A – 2 kA
sine wave	$5 - 10^5$	0.2 A, 2 A, 4 A
sine wave	$10^5 - 10^7$	≤ 0.02 A

Table 6.1: Overview of the parameters of the current sources.

In our experiments a lead or coaxial cable (RG-58/U) was placed in the center of the tray at a height Δy of 2.5 mm above the floor of the tray. In some cases the

magnetic field at this position has also been measured. Two pick-up coils have been used for this purpose. First a single turn coil with a height Δy of 1.4 mm and a length of 1 m was placed at 1.1 mm above the floor. This coil has a large bandwidth, but at low frequencies, due to the differentiating behavior, a low sensitivity. In most experiments the output of the single turn coil was not measured directly, but through an active integrator, which also allows measurements at low frequencies. In addition a second coil of 50 turns, with a height Δy of approximately 2.5 mm and a length of 1 m, was placed at about 0.5 mm above the floor of the tray. The 50 turn coil can be used as a differentiating sensor up to 20 kHz.

6.3   Sinusoidal currents

The BEM calculations in Table 5.2 show that the H-field inside a deep tray ($h/w = 2$) depends on the relative permeability. For small excitations (small i_{cm}) the H-field remains small and, as Fig. 6.1 shows, the static magnetization curve of ferromagnetic materials then can be approximated by a linear curve, which can be described with the initial permeability. We measured the inside H-field with the single turn coil and integrator. For a small sinusoidal current with a peak value of $i_{cm} = 0.2$ A$_{peak}$ we found good agreement between the measured H and a BEM calculation in which we used $\mu_r = 120$, as was also found in Section 5.3, when we discussed the transfer impedance.

With an audio amplifier and a transformer with a very low output impedance we obtained larger currents of 2 A$_{peak}$ and 4 A$_{peak}$ in the frequency range from 5 Hz to 100 kHz. The H-field scaled linearly with the current. The permeability seems to remain at its initial value ($\mu_r = 120$).

At 50 Hz large sinusoidal currents, up to 2 kA$_{peak}$, have been injected by means of a current transformer. The current was regulated by a variac on the primary side of the current transformer. The variac was fed from the mains. Figure 6.3 shows a more than linear increase of the peak value of the H-field with an increase in i_{peak}. Another interesting quantity is the harmonic distortion (ξ) [Roz 94, IEC]:

$$\xi = \sqrt{\sum_{n=2}^{N} A_n^2 \Big/ \sum_{n=1}^{N} A_n^2} \tag{6.1}$$

The harmonics A_n are obtained from a discrete Fourier transform (DFT) of the measured H over an integer number of periods. The quantity N is the total number of harmonics. Summation in Eq. 6.1 was done up to the thirteenth harmonic ($N = 13$). The harmonic distortion in H is negligible ($\xi \leq 0.05$) for currents up to 71 A$_{peak}$. For larger currents the harmonic distortion becomes appreciable. The injected current was less distorted; only at an i_{cm} of 1800 A$_{peak}$, 50 Hz, the limit of $\xi = 0.05$ was reached for the current.
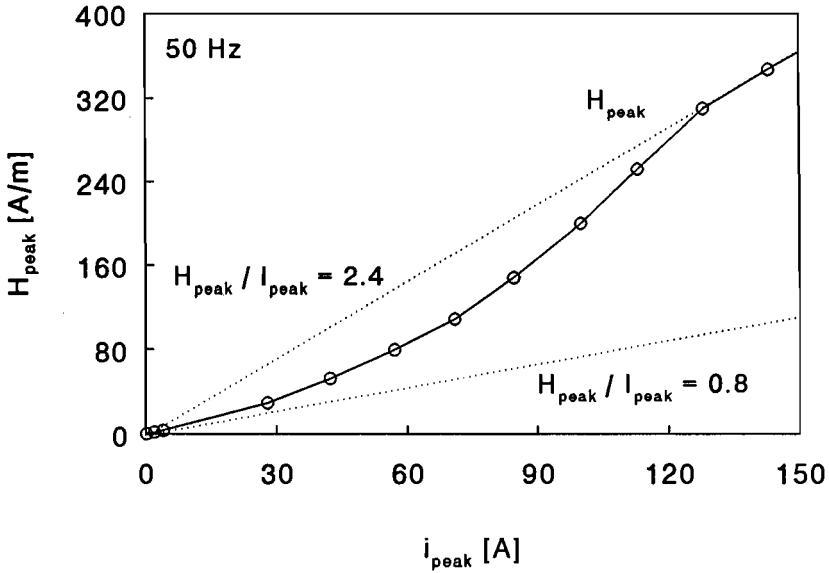
Fig. 6.3: The peak H-field as a function of the peak current i_{cm} measured in the deep steel tray H3S.
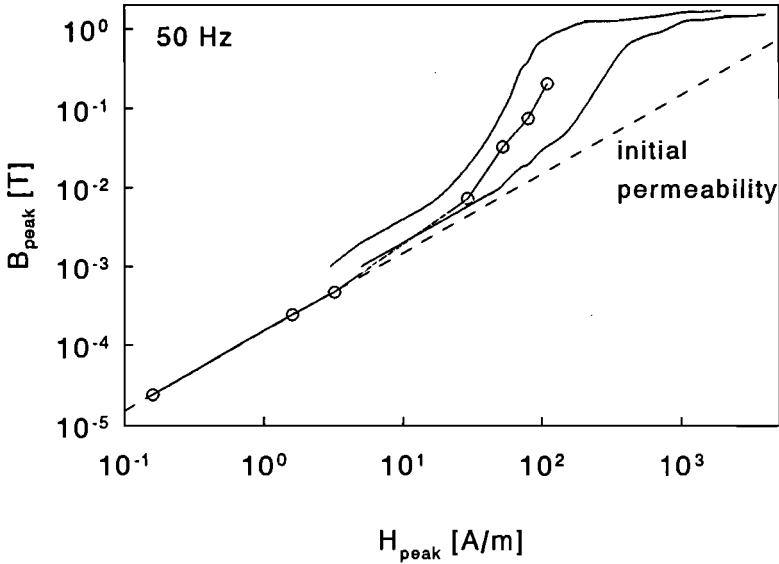
Fig. 6.4: The markers indicate the product of the measured H-field above the floor center of the deep steel tray (H3S) and the permeability used in a BEM calculation to obtain the same local H-field. This procedure generates a "magnetization curve" for the steel of the tray floor. The other lines are the static magnetization curves already presented in Fig. 6.1.

For a current of 71 A_{peak} the local H-field (peak value 109 A/m) above the floor center is still sinusoidal, but its peak value is 1.7 times larger than predicted by a linear extrapolation of the measurement at 0.2 A_{peak}. A BEM calculation delivers the measured field strength, when a value of $\mu_r = 1500$ is used instead of $\mu_r = 120$. With this value of μ_r the peak of the local B-field inside the steel at the floor center is 0.2 T. In Fig. 6.4 some more B-H-combinations, determined in this manner, are connected by a curve, which can be seen as a magnetization curve for the steel of the tray floor. Strangely enough, our local field measurements in the tray show about the same behavior as the static magnetization curves from Fig. 6.1, even while, at the edges of the tray, the fields are already much larger.

In the following we concentrate on the shallow steel tray H2S ($h/w = 1/2$), when not otherwise stated. In Fig. 6.5 two typical plots of v_{dm} are given for a large i_{cm} at 50 Hz. Comparison with H-field measurements shows that v_{dm} is completely dominated by the electric field. At this low frequency the peak voltage usually is the most interesting EMC parameter. Figure 6.6 shows a typical curve of the peak voltage as function of the peak current. In an attempt to get a clearer understanding of the non-linear phenomena, measurements were also done at 250 Hz and 500 Hz. These measurements are also shown in Fig. 6.6. In this case the variac, mentioned above, was not connected to the mains, but to a motor driven generator.
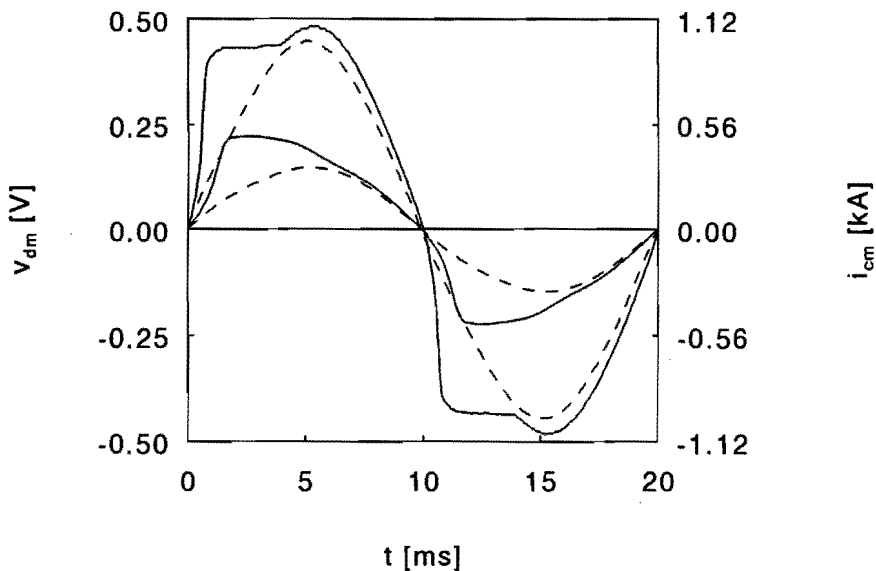
Fig. 6.5: Two typical combinations of v_{dm} (solid line), after 1 m tray, and i_{cm} (dashed lines) for two values at 50 Hz, measured for tray H2S. The left axis in V and the right axis in kA are chosen such that the v_{dm} and the i_{cm} curves coincide at low currents. For this scaling the measured $|Z_t(50\ Hz)|$ of Fig. 5.5 has been used.
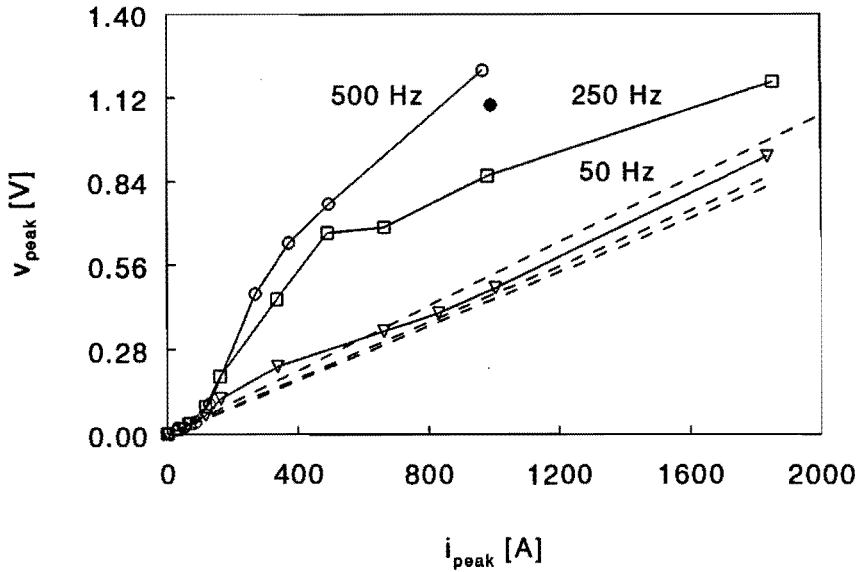
Fig. 6.6: The peak voltage v_{dm} as a function of the peak current i_{cm} measured for the steel tray H2S (see Table 5.4). The markers indicate the measurements. The dashed lines are extrapolations from Fig. 5.5. The closed marker ($\bullet$) indicates a measurement for 500 Hz, 1 kA, at 20° C; this shows that the observed effects are not of thermal nature.
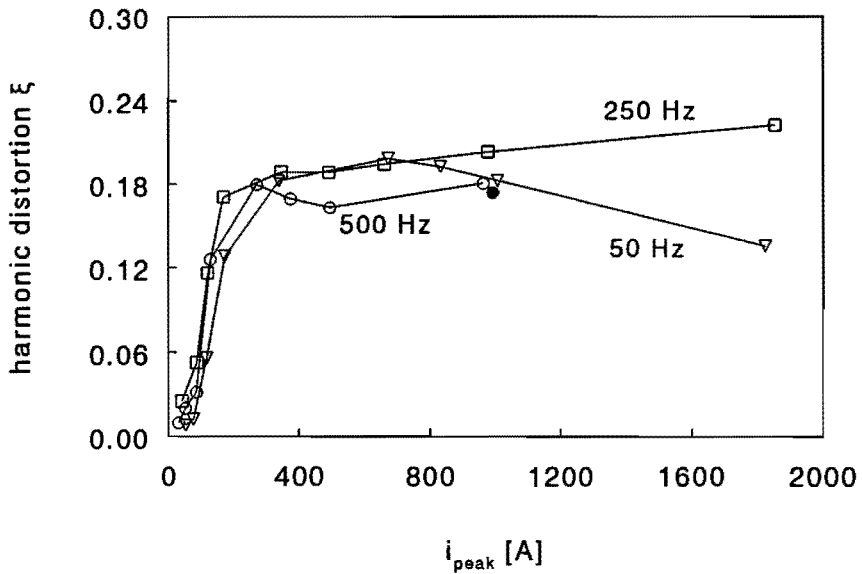
Fig. 6.7: Typical graph of the harmonic distortion ξ of the measured v_{dm} for the steel tray H2S (see Table 5.4) plotted against the peak current. The closed marker ($\bullet$) indicates a measurement for 500 Hz, 1 kA, at 20° C.

In Fig. 6.6 we see that the maximum difference between the measured peak voltage and the linear extrapolation of the measurements from Fig. 5.5 occurs at 500 Hz, at a current of 270 A_{peak}. The measured voltage then is a factor 2.9 higher. This factor decreases for lower frequencies and deeper trays. At 50 Hz this factor is less than 1.5 in all cases studied.

Figure 6.7 shows a typical curve of the harmonic distortion ξ as function of the peak current i_{cm}. For our home-made steel trays the harmonic distortion in v_{dm} becomes appreciable ($\xi > 0.05$) above 100 A_{peak}. As Fig. 6.7 shows, the harmonic distortion curve becomes flat again at 240 A_{peak}. The corresponding peak H-field in the floor center is 480 A/m. As shown in Fig. 6.4 this H-field could cause saturation. It is further interesting that the harmonic distortion of the H-field in the shallow tray has the same qualitative behavior as the distortion of v_{dm}, shown in Fig. 6.7. Quantitatively the distortion of the H-field is smaller than 0.05, except between 170 A_{peak} and 340 A_{peak} at 50 Hz. At 2 kA_{peak} the peak value of H differs only 20 % from the linear extrapolation of the measurement at 0.2 A_{peak}.

When i_{cm} is sustained for several minutes, the tray is heated, especially at 500 Hz, 980 A_{peak}, the temperature goes up to about 60°C; eddy current and hysteresis losses both increase with frequency. To check if the thermal effect is important, also a measurement has been made in which the current was only switched on for a very short time, so that the tray remained at room temperature. As Fig. 6.6 shows this reduced v_{dm} by only 10% and according to Fig. 6.7 this reduced ξ by only 3%. The heating effect does not seem to be very important.

6.4   Damped sine waves

Switching currents and lightning currents are transients with a large frequency content which makes analysis difficult. Therefore damped sine waves at higher frequencies (20 kHz and 1 MHz) are considered first. For these measurements we discharged a high voltage capacitor (C), through a spark gap, over the self inductance formed by the tray and its return conductor. At 20 kHz ($C = 31$ μF) the current was varied between 9 kA_{peak} and 40 kA_{peak} and at 1 MHz ($C = 10$ nF) between 500 A_{peak} and 7 kA_{peak}.

In Fig. 6.8 a typical plot is given of v_{dm} and i_{cm} against time t for 20 kHz. In this figure the left axis in V and the right axis in kA are chosen such that the v_{dm} and the i_{cm} curves coincide at low sinusoidal currents. For this scaling the measured $|Z_t(20 \text{ kHz})|$ of Fig. 5.5 is used. When we compare the v_{dm} measured in the tray with the product $|Z_t(20 \text{ kHz})i_{cm}|$, Fig. 6.8 shows very good agreement between the predicted and measured peak values early in time. At later times the predicted peak value becomes 5 times too low. Probably this factor 5 is more determined by the instantaneous value of i_{cm} than by the earlier peak currents; we found the

same factor for a measurement in which i_{cm} started with an initial peak of 9 kA. In both measurements the last current peak was 1 kA, after this peak the spark gap in our current source extinguished.
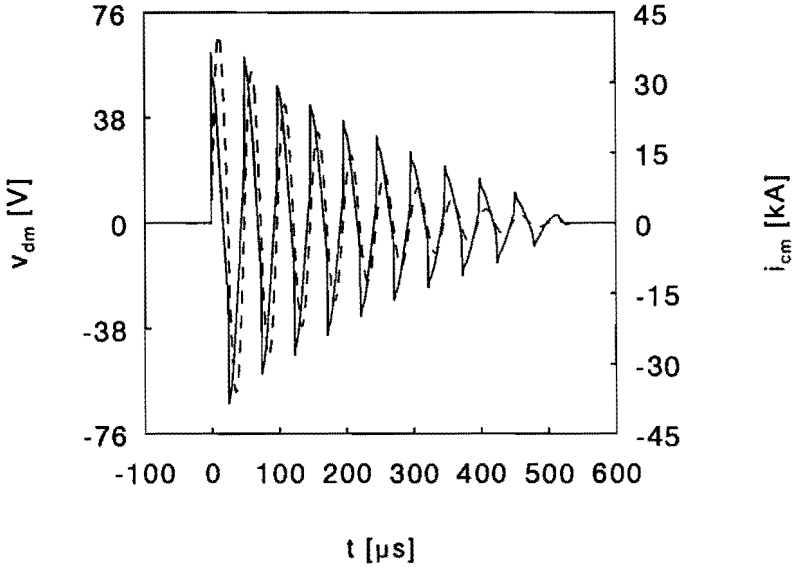

Fig. 6.8: Typical plot at 20 kHz of v_{dm} (solid line), after 1 m tray, and i_{cm} (dashed line) with a damped sine wave shape, measured for tray H2S. The left axis in V and the right axis in kA are chosen such that the amplitudes of the v_{dm} and the i_{cm} curves coincide for low sinusoidal currents. For this scaling we used the measured $|Z_t(20\ kHz)|$ of Fig. 5.5.

We tested the validity of the comparison between measured v_{dm} and calculated product $Z_t(20\ \text{kHz})i_{cm}$ via a measurement on the aluminum tray H2A at 20 kHz; for the first peak the maximum difference between measurement and prediction was 21 %, while the difference, contrary to the steel tray, decreased for longer times.

We repeated the same analysis for the steel tray at a frequency of 1 MHz. The predicted peak value is at maximum a factor 2.2 lower than the measured value. For the deeper tray H3S this factor is somewhat less.

At 20 kHz a Fast Fourier Transform (FFT) of v_{dm} showed only odd harmonics. For i_{cm} with a first peak value of 40 kA$_{peak}$ the third harmonic of v_{dm} was 17% of the first, the fifth 9.5% and the seventh 5.9%. At 1 MHz also even harmonics appear. In none of the experiments the current itself was distorted.

At both frequencies the H-field outside the tray walls seems to be linearly proportional to i_{cm}; comparison to BEM calculations indicates that μ_r keeps its low initial value. This is in sharp contrast with the measurements below 500 Hz, presented in

the previous subsection, where already below 100 A_{peak} higher values of μ_r had to be assumed. For the fixed cable position, the v_{dm} in our home-made steel trays is completely dominated by the electric field term in the right hand side of Eq. 2.12 at 20 kHz. At 1 MHz the contribution of E and H to v_{dm} are of the same order.

At 1 MHz the higher harmonics start to appear in v_{dm}, measured for the steel plate H1S and the shallow steel tray H2S, at a current of approximately 1 kA_{peak}. For the deeper steel tray H3S higher harmonics occur only above a current of about 5.9 kA_{peak}. It is interesting to note that the H-field at the floor center, corresponding to these currents, is the same for all three grounding structures $H \approx 1$ kA_{peak}/m. With a relative permeability μ_r of 120 we then find at the floor center: $B \approx 0.2$ T_{peak}. It is remarkable that the same value for B has been found in the previous section for the onset of higher harmonics at 50 Hz.

We also tested a coaxial cable, with its shield connected at both ends to the tray, instead of the single lead. A loop is formed by the surface of the tray and the cable shield. According to Section 2.5 a voltage is induced in this intermediate loop, which results in a current i_{im} over the cable shield. The coaxial cable was short-circuited at one end. The transfer impedance of the cable proper causes a voltage over its terminals at the other end. The impedance of the intermediate loop increases with frequency and successfully suppresses the higher harmonics in i_{im} and thus in the voltage over the terminals of the cable. The behavior of the fundamental however, is still non-linear with respect to i_{cm}.

6.5   Lightning pulses

Our 2.4 MV surge generator consists of a 12 stage Marx generator, which is connected to a high voltage divider via a 500 Ω resistor. The tray under test was connected to the high voltage divider via an additional 500 Ω resistor. This setup produced a 0.8 μs / 8.6 μs pulse with a peak current variable between 200 A and 2 kA; an example is given in Fig. 6.9.

The transfer function of a steel tray for a lightning pulse should, as a first test for non-linearity, be compared to the transfer impedance from Fig 5.5. This is most conveniently done by transforming the measured voltage and current to the frequency domain and calculating $Z_t(f)I_{CM}(f)$, as is shown in Fig. 6.10. For $Z_t(f)$ the measurements from Fig. 5.5 have been used, thus we assume a constant μ_r of about 120.

The dynamic range of especially the current over the frequency range from Fig. 5.5 appeared to be too large for the 8-bit ADC in our oscilloscope. Therefore two measurements have been made with the same settings of the surge generator. In one measurement both voltage and current were low-pass filtered with the transition point at 50 kHz. In the other measurement no filters were used and the output of
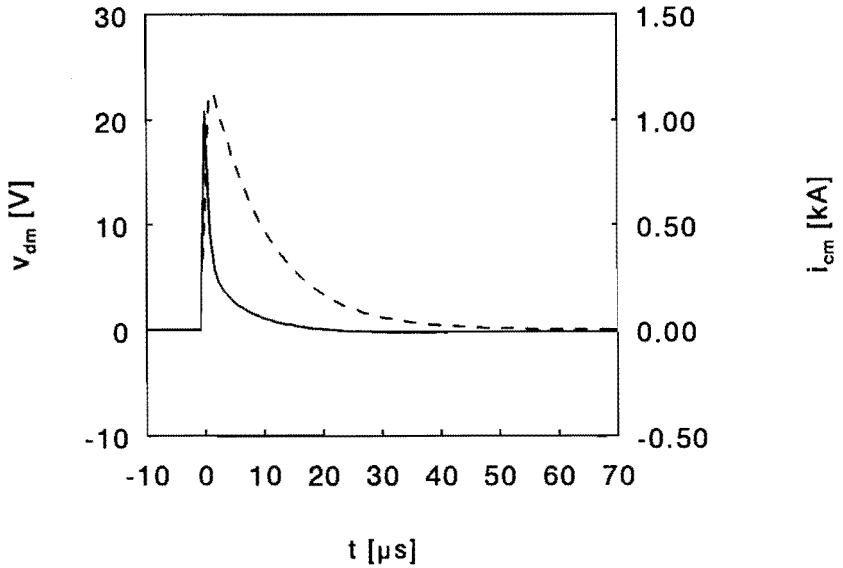
Fig. 6.9: Typical plot of a lightning pulse; v_{dm} (solid line) induced over 1 m tray length and i_{cm} (dashed line), measured for H2S.

the Rogowski-coil was directly measured with a 1:10-divider, so a signal linear to the derivative of the current was obtained, with emphasis on the higher frequencies. The total current was numerically restored. From an EMC point of view this direct measurement of the output of the Rogowski-coil is less desirable [Hel 93].

To obtain the low frequencies a lot of zero-padding to the data is necessary. However these long FFT's demand very large computer resources, therefore Sample Rate Reduction (SRR) has been applied [Sch 92]. Comparison of a long FFT and a short FFT after SRR showed good consistence between both methods. In fact SRR also has been applied to the measurement on the steel tube, presented in Fig. 6.2.

When V_{DM} and $Z_t I_{CM}$ from Fig. 6.10 are compared for the aluminum tray quite good agreement is found. When one considers the steel tray at high frequencies, good agreement is found between $Z_t I_{CM}$ and V_{DM}, but at low frequencies, $Z_t I_{CM}$ is only 30% of the measured voltage V_{DM}. Most likely, non-linear effects occur for this unipolar current pulse; these show up especially at low frequencies.

Though the applied pulse is unipolar, a really permanent magnetization of the trays is not expected, because structures with an airgap are self-resetting [Haa 91, p.X-26]. Consecutive measurements on the same tray showed indeed no significant difference. For solid wall tubes permanent magnetization could take place [Koe 91], but also here consecutive measurements showed no significant variations.
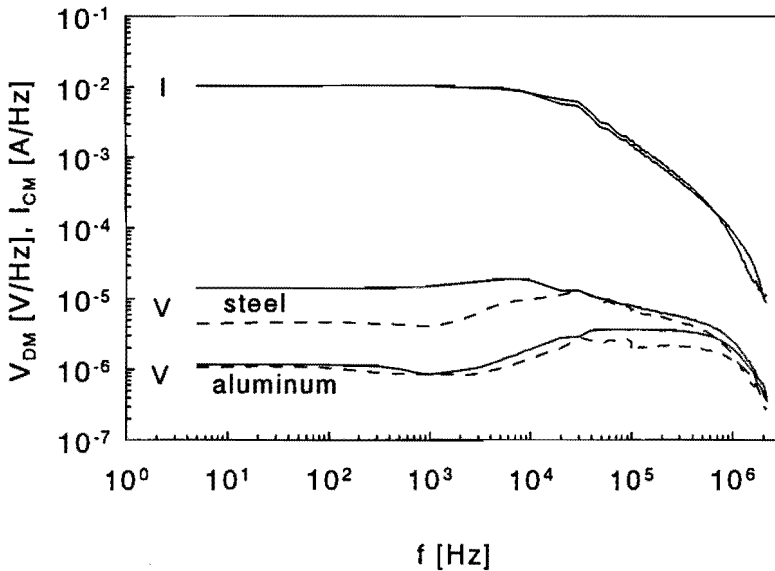
Fig. 6.10: The solid lines show the Fourier transforms of the signals from Fig. 6.9 and also from measurements on the aluminum tray H2A. The dashed lines give the products $Z_t(f)I_{CM}(f)$.

6.6   Conclusion

When large common mode currents are flowing over steel cable trays, the transfer function becomes non-linear. Even at high frequencies, up to 1 MHz non-linear effects have been observed. The harmonic distortion of the voltage v_{dm} is mainly caused by the distortion of the electric field at the floor of the tray. The magnetic field behaves much more linearly, especially at higher frequencies.

The maximum observed difference between a measured peak voltage and a prediction based on the linear extrapolation of the results for a small signal was a factor 5; in most situations this factor is less. In practical situations the exact amplitude of the disturbance current is often also not well known (e.g. lightning protection). When both uncertainties are taken into account, system design based on linear assumptions should be acceptable.

When the low frequency (≤ 500 Hz) sine waves and higher frequency (≥ 20 kHz) damped sine waves are considered, harmonics up to the thirteenth were found. For the lightning pulse a higher transfer is observed in the low frequency range, so mainly the tail is affected.

Chapter 7

Induced currents and voltages in secondary cables connected to Gas Insulated Switchgear

The transfer impedance concept gives us two possibilities to lower the differential mode voltage caused by a common mode current over a grounding structure. Firstly we can lower the transfer impedance by modifying the grounding structure. Secondly we can lower the current by rerouting the grounding structure or by adding extra grounding connections. Both methods are demonstrated in a laboratory GIS (Gas Insulated Switchgear) setup.

7.1 Introduction

In Chapter 2 we introduced the transfer impedance concept. We saw that a common mode current I_{CM} over a cable caused a differential mode voltage V_{DM} at the end of the cable due to the transfer impedance Z_t. Obviously this differential mode voltage can be reduced in two ways. We can lower the transfer impedance by using a cable with a better shield or we can reduce the common mode current over the cable. In this chapter we demonstrate both approaches to reduce interference voltages in our Gas Insulated Switchgear (GIS) laboratory setup. Note that this is only one example of the validity of this approach; many more could be given.

A GIS, used in certain types of substations, is a closed structure which surrounds high-voltage conductors and switches. Switching actions generate intense electromagnetic disturbances with fast rise times (approximately between 5 and 20 ns), which travel through the GIS, because the GIS presents an almost ideal transmission line [Fuj 82]. Inside a 380 kV system the instantaneous power in the first wavefront is on the order of several hundreds of MW. These disturbances couple to the outside of the GIS through the openings in the GIS wall, for instance at the position where a high voltage overhead line enters the closed housing. As a result of this coupling disturbance currents will flow over the cables, which connect the sensors in and around the GIS to the control equipment . Coupling from the inside to the outside also can occur at the ends of HV-cables [Wet 90, Wou 95]. In this

chapter the coupling process from the inside to the outside is not discussed; the common mode current at the outside of the GIS is considered as a given fact.

7.2 Experimental setup

The high voltage (HV) circuit is called the primary circuit, the control equipment for the HV the secondary equipment and the normal electrical installation (lighting, wall outlets) is called the tertiary circuit.

7.2.1 Primary circuit

In our experiments we used a single phase coaxial GIS system (Fig. 7.1), basically a HOLEC BISEP setup, which is designed for 380 kV AC operation [Gom 87]. The GIS is built from tubes (7 mm steel wall and 32.5 cm o.d.) of about 4 m length. The inner (high-voltage) conductor is supported by insulators (spacers), which are mounted between the tubes. The U-shaped system consists of two sections. The section between points G and H in Fig. 7.1 is the measuring section and is used for the testing of various sensors and partial discharge research. The dotted extension beyond H has been used for pulsed corona measurements [Hee 95], but during our experiments it was disconnected; the GIS was terminated characteristically with 74 Ω at point H. The other section is the charging section and is at one end connected to a DC power supply (positive voltage, 200 kV maximum); we used a charging voltage of 70 kV for all measurements. Both sections of the GIS can be interconnected by a HV-switch; we used a triggered spark gap (indicated by S in Fig. 7.1) [Hel 90].

The bushing used for control of the electric field at the entrance of the charging section is mounted vertically on top of the GIS. A long external HV-lead simulated an overhead transmission line. The outside of the GIS tube is connected over its full circumference to the conducting floor of the HV-laboratory at the U-bend by means of two large brass plates (GP near E and G). The other end of the measuring section was, via an aluminum cable tray, grounded at H as well, thus forming a short-circuited loop between H and GP parallel to the charging section. The spacers were bridged by 12 steel bolts and a copper foil around the complete circumference; therefore the only opening in the GIS was the HV-bushing.

7.2.2 Secondary circuit

Instead of the normal control equipment we used a test cable and an oscilloscope, which measured the interference voltage across a 50 Ω-terminating-resistor at the end of the cable. The 7.2 m long test cable was connected to the GIS near the bushing. There the cable was terminated into 50 Ω (see detail at B in Fig. 7.1). Over a length of 6.7 m the cable ran parallel to the GIS. Its height was varied: close
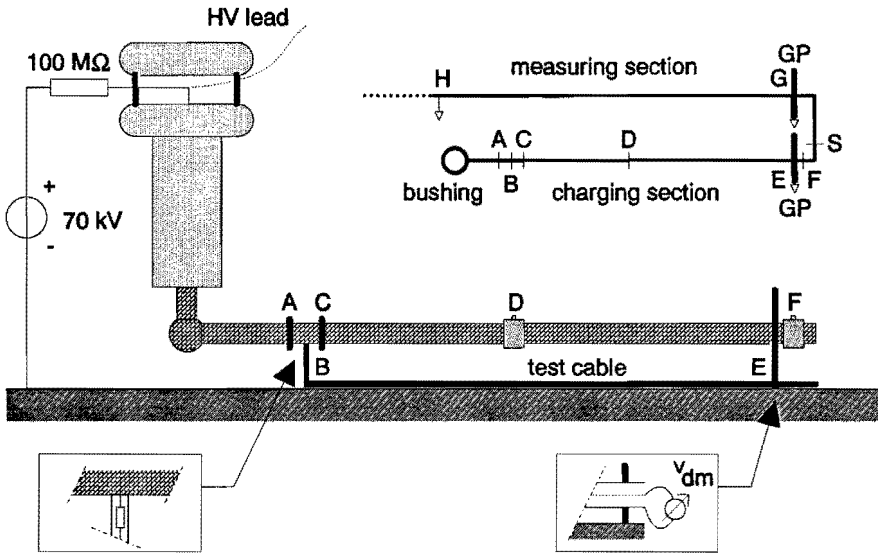
Fig. 7.1: Side view of the GIS in the High-Voltage Laboratory of Eindhoven University of Technology. The insert above shows a top view of the U-shaped installations. The inserts below illustrate the connection of the test cable (which is shown in its lowest position) [Deu 95].

to the GIS, near the floor, or halfway in between. The cable shield was properly grounded at the brass ground plate at point E (see detail at E in Fig. 7.1). We experimented with two different cables: a YMvKas cable, which is a common installation cable with a shield consisting of a limited number of woven steel wires, and an RG-214/U, a coaxial cable with a high quality braid. The shield of the first cable is designed for mechanical rather than for electrical protection. The type we used has three inside leads, which we connected in parallel at both ends of the cable.

7.3   Diagnostics and sensors

The rise time of the waves inside our GIS can be a few nanoseconds [Hou 90]. Therefore our measurement setup should have a large bandwidth and excellent EMC properties. We employed the differentiating-integrating concept [Hee 89]. Passive integrators, comparable to the types developed by van Houten [Hou 89, pp.89-92], with a time constant of about 50 ns, restored the signals from the differentiating sensors. The droop in the signals, caused by the imperfect passive integration, was numerically corrected later [Hel 91, pp.59-61].

The voltage of the wave inside the GIS was measured with capacitive sensors. Ring shaped electrodes are readily present in the spacers. These electrodes form

together with the HV-conductor of the GIS a capacitor. This capacitor together with the 50 Ω termination resistor at the end of the RG-214/U signal cable gives a signal proportional to the derivative of the voltage. The bandwidth is limited by the stray capacitance between the electrode and the GIS-tubes; to obtain sufficient bandwidth (30 MHz) we connected 12.5 Ω (four 50 Ω resistors in parallel) across the beginning of the cable.

The currents outside the GIS were measured with a shielded helical single turn Rogowski-coil [Hel 95c]; imagine a wire-wound Rogowski-coil, of which the wire makes exactly one turn around the circumference of the complete coil. This wire is deformed to a strip with considerable width, which is bent into a circle. What remains is a torus with one interruption and a helical slot. Inside the torus a return conductor is mounted. The behavior of this helical single-turn Rogowski-coil is identical to a multi-turn Rogowski-coil. Because it has only one winding, its sensitivity is small ($M = 1.0$ pH), but it has a large bandwidth (75 MHz with shield, up to 300 MHz without).

The voltage measured at the spark gap (point S in Fig 7.1) was used as time reference for the other signals. For registration we used a four channel, 500 MHz, Hewlett Packard digital oscilloscope (HP 54542A). When necessary, the differential mode voltage of the test cable was measured via an 1:200-divider.

7.4 Measurements and discussion

7.4.1 Coupling of the inside wave to the outside

When spark gap S is triggered, the charging section discharges into the measuring section. This causes a travelling wave in the measuring section and a travelling wave in the opposite direction in the charging section. At the bushing the latter wave will partly reflect and partly couple to the outside of the GIS.

Theoretically the amplitude of the internal voltage wave is half the charging voltage (70 kV / 2 = 35 kV). Figure 7.2 shows a measurement at point F (see Fig. 7.1). Some overshoot and oscillations occur at the initial wave front. For the sake of graphical representation the measured voltage signal was reversed in polarity; the DC charging voltage is not shown. This allows a direct comparison of the initial part of the internal current with the CM current on the outside; before the first internal reflection arrives at F (after 65 ns as indicated by the dashed line in Fig. 7.2) the internal current can be calculated from the measured voltage ($i(t) = v(t)/Z_0 = 70$ kV$/74$ $\Omega \approx 470$ A). After the first internal reflection both the initial and the reflected wave contribute to the measured internal voltage, which then no longer corresponds to the current at F. The amplitude of the reflected wave, measured at F, is 0.48 ± 0.04 times the original wave. The voltage polarity is the
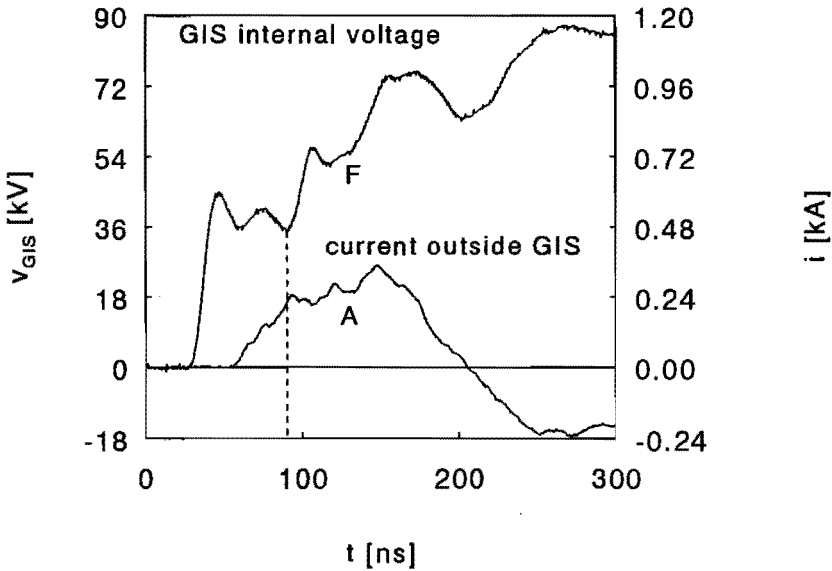
Fig. 7.2: *The internal wave measured as voltage at point F, and the CM current through the GIS measured at point A. Before 90 ns, indicated by the vertical dashed line, the internal current can be obtained from the voltage; the internal current signal then corresponds to the right axis. No test cable was present during these measurements.*

same; consequently the reflected current has the opposite polarity with respect to the initial wave.

In Fig. 7.2 the internal current has a rise time (t_r) of 10 ns and a peak of about 600 A. The capacitive properties of the bushing slow down the rate of rise of the external wave; the rise time of the CM current at point A is a factor 3 longer $(t_r \approx 30 \text{ ns})$. The peak current at A is about 250 A with no test cable present. The transmission coefficient from the inside wave to the wave over the outside GIS tube wall then is 0.42. This value compares well with the just mentioned reflection coefficient of 0.48.

When a test cable is connected to the GIS at point B, one part of the CM current will be reflected back to the bushing (the first maximum of i_A increases). The other part will divide itself over the GIS tube and the test cable. Figure 7.3 shows the current over the GIS before (i_A) and after (i_C) the cable, and the current over the cable (i_B). The algebraic sum $i_A - i_B - i_C$ of these currents is zero within the measurement accuracy, as Kirchhoff's current law requires. Though the CM current over the GIS tube is inhomogeneous [Slu 95], the currents i_A, i_B and i_C can be predicted fairly well with transmission line calculations, except for the time delay of 10 ns in i_B. For these calculations we refer to [Hor 94b, Deu 95].

The above mentioned results compare very well with the results that were already
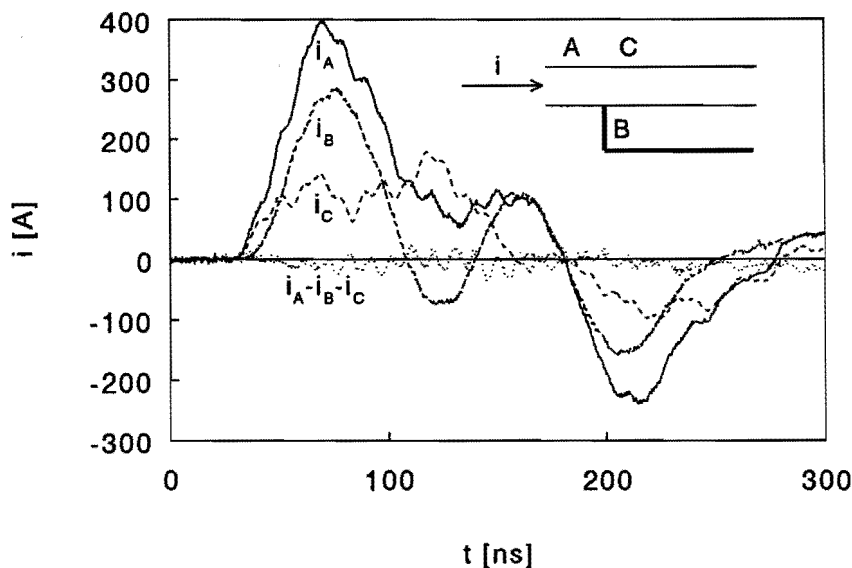
Fig. 7.3: The measured CM current through the GIS at positions A and C, and the CM current through the cable at position B. The algebraic sum ($i_A - i_B - i_C$) of these currents, indicated by the dotted line, is zero within the measurement accuracy. Positions A, B and C are indicated in the inset and correspond also to the points shown in Fig. 7.1.

reported in [Deu 95]. The first peak inside our GIS is typical for switching operations (compare e.g. with [Riq 92, Fig. 1]). The behavior of the transient for longer times depends on the exact GIS configuration (reflection points) and, when opening a switch, on possible reignition of the switch (see e.g. [Sme 93]); field experiments however have shown that usually the most intense disturbances occur within the first 150 ns [Wet 90].

The high-frequency behavior of various bushings may differ, but our results seem to be representative for other situations; Thomas et al. report from a field experiment, that currents over cables connected to a 230 kV GIS have predominant frequencies in the range of 1-20 MHz [Tho 94]. In our laboratory setup we found with a Fourier analysis 4.4 MHz to be the most dominant frequency. For further reading on the coupling through bushings we refer to the works of Miri and Binder e.g. [Bin 94].

7.4.2 Changing or adding a grounding structure

The starting point of our experiments is a situation, in which the standard control cable (YMvKas), is lying on the floor parallel to the GIS. It is connected to the GIS at point B after a vertical section (see Fig. 7.1). The voltage is measured at the other end of the cable at point E. As Fig. 7.4 shows the first DM peak is the

	$\hat{\imath}_B$ [A]	$\hat{v}$ [V]	reduction factor	$2\hat{v}/\hat{\imath}l$ [Ω/m]	$|Z_t(4.4\ \text{MHz})|$ [Ω/m]
YMvKas	211	218	1	0.29	0.16
RG-214/U	282	1.19	183	$1.2 \cdot 10^{-3}$	$1.4 \cdot 10^{-3}$
YMvKas in tray	282	1.55	141	$1.5 \cdot 10^{-3}$	$1.9 \cdot 10^{-3}$
RG-214/U in tray	282	$7.75 \cdot 10^{-3}$	$2.81 \cdot 10^4$	$7.6 \cdot 10^{-6}$	$1.6 \cdot 10^{-5}$

Table 7.1: Measured maxima of the current ($\hat{\imath}_B$) and DM voltage ($\hat{v}$) for several configurations. For the reduction ratio the DM voltage measured with the YMvKas is taken as reference. The estimated transfer impedance $2\hat{v}/\hat{\imath}l$ (see text; Eq. 7.1), given in the second column from the right, compares well to the actual transfer impedance $|Z_t|$ at 4.4 MHz, given in the last column.

largest with about 220 V_{peak}. The current over the cable (i_B) is shown in Fig. 7.5; the first peak is about 210 A_{peak}.

When we replace the YMvKas by the RG-214/U cable, which has a better shield, the current over the cable increases slightly (280 A_{peak}) as shown by Fig. 7.5, but the first peak of the voltage is a factor 180 lower; only 1.2 V_{peak} as shown by Fig. 7.4.

Figures 7.5 and 7.6 show, that about the same increase in current and decrease in voltage for the first peak are obtained, when the YMvKas is mounted in an aluminum tray, with $h/w = 2$, $2h + 2w = 0.15$ m and $d = 3$ mm (see Fig. 4.2). When the RG-214/U is mounted in the same tray, the CM current through the combination of tray and cable is not changed, but the first voltage maximum is reduced by a factor 154 to 7.75 mV_{peak} as Fig. 7.6 shows. Figure 7.6 also shows, that, at longer times, a damped oscillation occurs in the intermediate mode circuit, but that the DM voltage remains at a low value; below 12 mV_{peak} for the RG-214/U in the tray. The measured oscillation frequency is 15 MHz. The propagation time of the wave on the outside of the plastic covered, 7.2 m long, cables is 34 ns [Slu 95]. The wave velocity (c) thus is $2.1 \cdot 10^8$ m s^{-1}. Because the cable shields are short-circuited to the tray at both ends, a first resonance can occur at a wavelength (λ) of twice the length (l) of the cable: $\lambda = 2l = 14.4$ m. The corresponding frequency (c/λ) indeed is 15 MHz.

In Table 7.1 an overview is given of the first maxima in the current and the voltage for the configurations discussed above. The reduction factor is calculated with respect to the first voltage maximum of the YMvKas. We have seen that 4.4 MHz is the dominant frequency in most of our measurements. For this frequency we can estimate the overall transfer impedance ($|Z_t|$) from the first peak voltage ($\hat{v}$) and peak current ($\hat{\imath}_B$):

$$|Z_t| \approx \frac{2\hat{v}}{\hat{\imath}_B l} \tag{7.1}$$
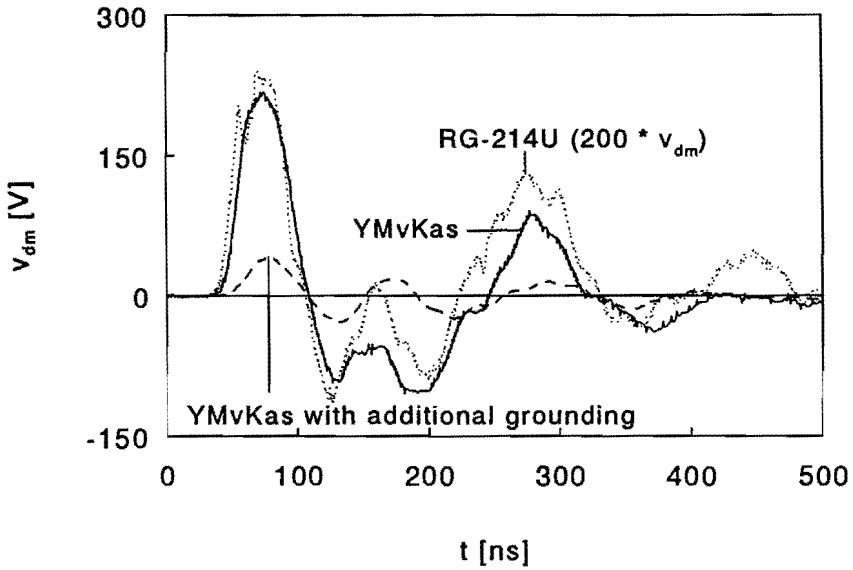
Fig. 7.4: The measured DM voltage at the end of a YMvKas (solid line) and an RG-214/U cable (dotted line, multiplied by a factor 200). The dashed line is the YMvKas with an additional grounding connection after 1 m, as will be discussed in Section 7.4.4.
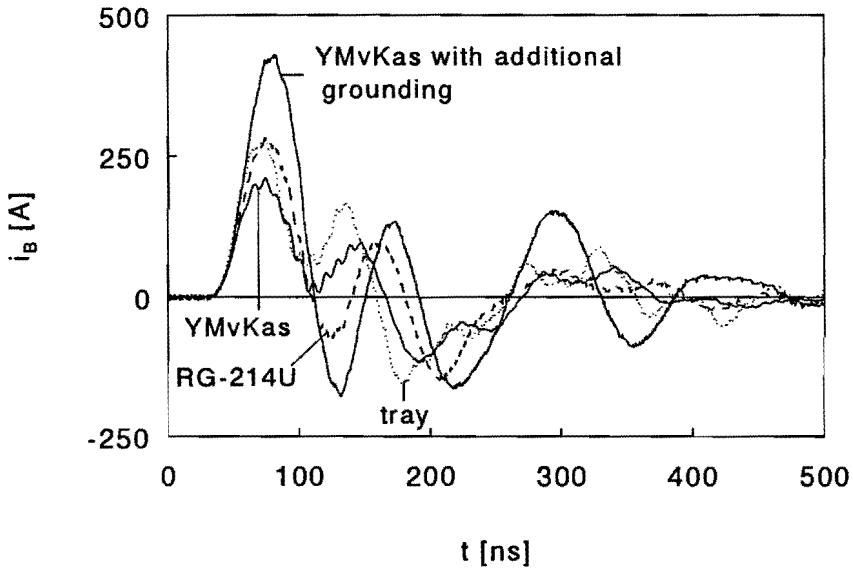
Fig. 7.5: The measured CM current (i_B) through the cables and through the combination of the cables and the cable tray. The configurations are indicated in the plot. The current through the combination of cable and tray (dotted line) is the same for both the YMvKas and the RG-214/U cable.
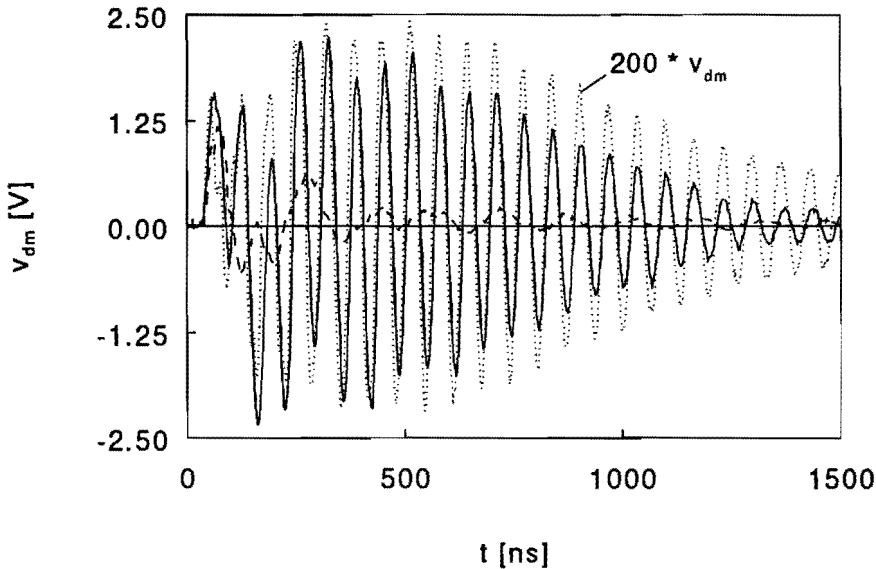
Fig. 7.6: The measured DM voltage at the end of a YMvKas (solid line) and an RG-214/U cable (dotted line, multiplied by 200) both mounted in an aluminum tray with $h/w = 2$ and $2h + 2w = 0.15$ m. For reference the DM voltage measured at the RG-214/U cable without a tray, from Fig. 7.4, also has been plotted here (dashed line, without multiplication factor).

The factor 2 in this equation takes into the account that the cable is terminated with 50 Ω-resistors at both ends. The outcome of Eq. 7.1 for the various situations is listed in the second column from the right of Table 7.1.

The actual values of the transfer impedances for the various situations are given in the last column of Table 7.1. For the cables these values are taken from Fig. 2.6. The transfer impedance of the cable and tray combination can then be calculated with Eqs. 4.13, 4.26 and 4.28. Our estimated transfer impedances are of the same order of magnitude as the actual transfer impedances; even when we neglect the transmission line properties they agree within a factor 2.

7.4.3 Influence of the cable position on the current and detected voltage

In all the experiments described above we placed the cable at the floor below the GIS. Figures 7.7 (YMvKas) and 7.8 (RG-214/U) however show clearly that it is better to place the cable close to the GIS. The voltage detected at the highest position of the cable, closest to the GIS, is a factor 10 to 15 smaller than the voltage at the lowest position. For the cable placed halfway this factor is 4.

When the cable is closer to the GIS the current over the cable decreases and con-
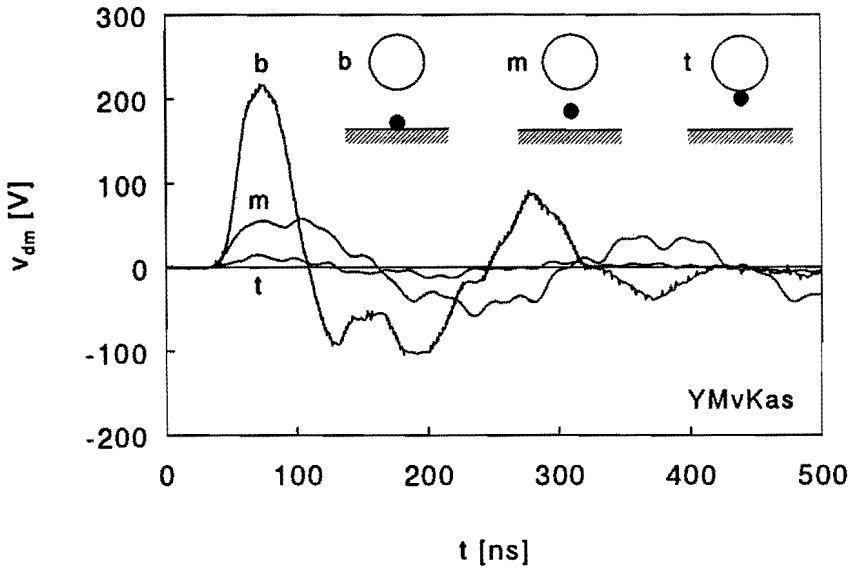
Fig. 7.7: The measured DM voltage at the end of a YMvKas cable at different heights. The interference is kept smallest with the cable close to the GIS.
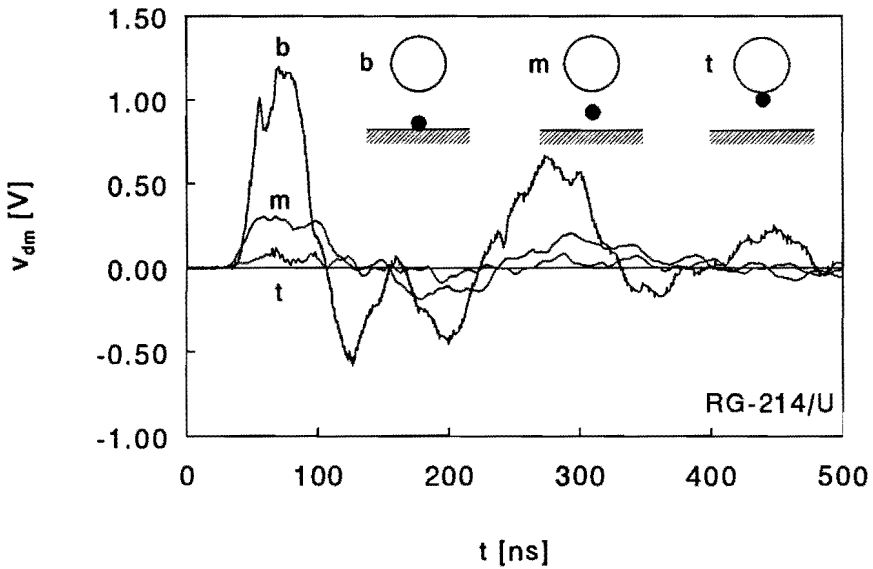
Fig. 7.8: The measured DM voltage at the end of an RG-214/U cable at different heights. The behavior of the DM voltage as function of the height of the RG-214/U is similar to the behavior of the YMvKas cable in Fig. 7.7; the DM voltage however is much lower due to the high quality shield of the RG-214/U.

sequently with $V_{DM} = Z_t I_{CM}$ the detected voltage decreases accordingly. Further less reflection from the cable connection at point B towards the bushing (point A) takes place. The transmission along the GIS towards point C increases [Deu 95].

7.4.4 Additional grounding of the cable or the GIS

Our setup shows a worst case situation, because both GIS tube and cable are only grounded far away from the bushing. We experimented with a 1 meter long strap (50 mm^2 copper braid) connected to the GIS envelope and to the ground directly below the bushing. For the RG-214/U at the lowest position this reduced the detected voltage only by a factor 1.3. Obviously grounding at the bushing should take place with large metal plates as proposed by Dick et al. [Dic 82]; they report reduction factors between 5 and 10. A factor 10 is also reported by Köhler et al. [Köh 93].

Instead of connecting the small grounding strap to the GIS it is more profitable to additionally ground the cable shield. We grounded the shield of the YMvKas, in the lowest position, directly below its connection point at the GIS. The measured current at point B, shown in Fig. 7.5, increased from 210 A$_{peak}$ to 430 A$_{peak}$, but this current now flows only over the cable for about 1 m, thereafter the CM current on the cable is very small and the detected voltage (Fig. 7.4) drops with a factor 5 to 42 V$_{peak}$.

7.5   Conclusions

Our results obtained at a charging voltage of 70 kV can be extrapolated linearly to the voltage for which the GIS was designed. For each phase in a three phase 380 kV AC system, the peak voltage with respect to ground, at which the first pole of the circuit breaker closes, is equal to $\sqrt{2/3}$ kV $\approx$ 310 kV. All currents and voltages measured in our setup should then be multiplied by 4.4 [Deu 95].

Correct routing of cables is important to keep interference voltages low. In this experiment we could reduce v_{dm} with a factor 10 to 15 by changing only the cable position from the floor towards the GIS. If this reduction is not enough or rerouting is not possible, we can use a cable with a better shield (lower Z_t) or we can install cable trays. The predictions based on the theory of the previous chapters are in good agreement with the measurement results shown here.

To allow disturbance-free measurements for other projects in the measuring section, this research resulted in an aluminum cable tray with dimensions $h/w = 2$, $2h + 2w = 0.36$ m and $d = 3$. This tray is placed directly on top of the measuring section and is connected to an EMC-cabinet. A test measurement with an 10 m long RG-214/U cable inside the tray showed only random noise and no interference; this cable was short-circuited and connected to the tray at the far end.

Chapter 8

General conclusions

At the end of each chapter the relevant conclusions have already been given. Here we only list some general conclusions.

The transfer impedance concept is very well suited for the EMC analysis of cabling and wiring. Its application is not limited to cable shields, but can also be used to analyze general grounding structures such as metallic plates or cable trays.

The transfer impedance is not a property of the grounding structure alone; it may be influenced by a nearby returning common mode current. A suitable measurement setup should resemble the actual situation: for non-symmetric cables in cable bundles the wire injection method gives better results, whereas, when the common mode current is returning far away from the cable, the triaxial method is preferred.

The common mode current over plates and cable trays returns in most practical situations through a far away conductor. Yet the triaxial method is not useful, because the current density at the edges of non-circular grounding structures is increased by the proximity of the cylindrical return. Our measurements were done with a modified wire injection method; a wide plate which was mounted 1 m away from the grounding structure under study was used as return conductor.

For non-magnetic plates and trays simple formulas ("engineering" expressions) were derived from a large number of Boundary Element Method (BEM) calculations. These formulas can also be applied to shallow ferromagnetic trays. For deep ferromagnetic trays no simple expressions have been found. All calculations agreed well with the measurements. Trays can be connected to each other without a significant increase of the overall transfer impedance; a connection with only one wire however should be avoided.

When large currents are flowing over ferromagnetic grounding structures non-linear effects occur. Harmonics up to the thirteenth were observed (for sinusoidal excitation), the highest detected differential mode voltage however remained within a factor five of the value expected from linear assumptions.

The transfer impedance concept suggests two ways to lower the differential mode

voltage. The first is to lower the transfer impedance by modifying or changing the grounding structure. The other is to lower the common mode current over the grounding structure by a change of the layout or by the addition of extra grounding connections. Experiments confirm the usefulness of both these methods.

As a recommendation for the future, the results from this thesis should be made accessible for the broader public interested in installation techniques. As a first attempt I have written an article in Dutch for an installation journal [Hel 95d], but more work in these area seems necessary.

Future research could concentrate on the reduction of the coupling between cables by means of specially designed cable trays (e.g. additional rims inside a tray) and on the reduction of the common-mode current over grounding structures, when multiple grounding connections are used. Theoretical studies could perhaps indicate, if there is an analytic method for deriving the engineering expressions. Further the exact behavior of magnetic materials is of interest, especially in view of the search for a practical grounding structure in which the magnetic circuit is closed; e.g. a tray with a well-closing lid.

Bibliography

[And 67]   Anderson, R.W., "s-Parameter techniques for faster, more accurate network design", *Hewlett-Packard Journal*, Vol. 18, No. 6, 1967.
Reprint available from Hewlett-Packard as *Application Note 95-1*.

[Bin 94]   Binder, C., A.M. Miri, "The transient field distribution near the encapsulation of GIS", *EMC'94 Roma*, Rome, Italy, 1994, pp.672-675.

[Bin 92]   Binns, K.J., P.J. Lawrenson, C.W. Trowbridge, *The analytical and numerical solution of electric and magnetic fields*, Chichester: John Wiley & Sons Ltd., 1992.

[Bla 85]   Bladel, J. van, *Electromagnetic fields*, London: Hemisphere, 1985.

[Bre 84]   Brebbia, C.A., J.C.F. Telles, L.C Wrobel, *Boundary Element Techniques: theory and applications in engineering*, Berlin: Springer, 1984.

[Bro 95]   Broek, S.P.M. van der, P.R. Bruins, M.J.A.M. van Helvoort, "Transfer function measurements with a 2-port s-parameter set", *Internal memo*, 95096, 1995.

[But 79]   Butterweck, H.J., *Elektrische netwerken* (in Dutch), Utrecht: Uitgeverij Het Spectrum, 1974.
Reprinted as lecture note, no. 5679, Eindhoven University of Technology.

[Car 26]   Carson, J.R., "Wave propagation in overhead wires with ground return", *Bell Syst. Techn. Journal*, 1926, pp.539-554.

[CRC 80]   *CRC handbook of chemistry and physics*, editors: R.C. Weast, M.J. Astle, Boca Raton, Florida: CRC Press, Inc., 60th ed., 1980.

[Cow 70]   Cowdell, R.B., "The effect of changing frequency and field intensity on the permeability of ferrous materials", *1970 IEEE Int. Symp. on EMC*, Anaheim, USA, 1970, pp.102-112.

[Def 90]   Defourney, M.M., M.A. van Houten, T.F. Buss, E.J.M. van Heesch, "Electric field computation description and examples with experimental comparison", *Proc. Int. Conf. Electrosoft 90*, Lowell, USA, 1990, p.361.

[Deg 93]   Degauque, P., J. Hamelin (editors), *Electromagnetic Compatibility*, Oxford: Oxford University Press, 1993.
Translation of: *Compatibilité Electromagnétique* (in French), Paris: Bordas, 1990.

[Deu 92]   Deursen, A.P.J. van, P.C.T. van der Laan, "EMC-course at student and post-academic level", *8th Int. Conf. on EMC*, Edinburgh, UK, 1992, p.302.

[Deu 94]   Deursen, A.P.J. van, *Internal memo*, 94091, 1994.

[Deu 95]   Deursen, A.P.J. van, F.B.M. van Horck, M.J.A.M. van Helvoort, P.C.T. van der Laan, "Induced currents and voltages in secondary cables connected to Gas Insulated Switchgear", *Proc. 9th Int. Symp. on High Voltage Engineering*, Graz, Austria, 1995, paper 6058.

[Dic 82]   Dick, E.P., N. Fujimoto, G.L. Ford, S. Harvey, "Transient ground potential rise in Gas Insulated Substations - problem identification and mitigation", *IEEE Trans. on Power Apparatus and Systems*, Vol. PAS-101, No. 10, 1982, pp.59-66.

[EEC 89]   EEC, "European Directive on EMC: 89/336/EEC of 3 May 1989", *Official EC Journal*, 23 May, 1989.

[Eic 88]   Eicher, B., Staeger C., Szentkuti, B., Fahrni, H., "Simple and accurate screening measurements on RF-cables up to 3 GHz", *Technische Mitteilungen PTT*, 4, 1988, pp.166-173.

[Ell 71]   Ellis, W.R., "Vacuum magnetic field and surface curent distributions for a slotted cylindrical shell carrying axial current", *J. Phys. D: Appl. Phys.*, Vol. 4, 1971, pp.332-337.

[Fer 70]   Ferber, R.R., F.J. Young, "Enhancement of EMP shielding by ferromagnetic saturation", *IEEE Trans. on Nuclear Science*, Vol. NS-17, 1970, pp.354-359.

[Fuj 82]   Fujimoto, N., E.P. Dick, S.A. Boggs, G.L. Ford, "Transient ground potential rise in Gas Insulated Switchgears - experimental studies", *IEEE Trans. on Power Apparatus and Systems*, Vol. PAS-101, No. 10, 1982, pp.52-58.

[Goe 92]   Goedbloed, J.J., *Electromagnetic Compatibility*, London: Prentice Hall, 1992.
             Translation of: *Electromagnetische compatibiliteit* (in Dutch), Deventer: Kluwer, 1990.

[Gom 87]   Gompel, F.M. van, "Een GIS laboratorium installatie als bron voor snelle pulsen en stoorsignalen" (in Dutch), HTS-thesis, Eindhoven University of Technology, EH.87.A.92 HTS, 1987.

[Gor 73]   Gordon, D.I. (coordinator), *Direct-Current magnetic hysteresigraphs*, American Society for Testing and Materials, 1916 Race Street, Philadelphia, Pa. 19103, 1973.

[Gri 71]   Griffith, D.E., "Surface transfer impedance of cable shields having a longitudinal seam", *IEEE Trans. on Communication Technology*, Vol. COM-19, No. 4, 1971, pp.517-522.

[Gun 86]   R. Gunn, "A common approach to signal separation", *EMC Technology*, 5, 1986, pp.53-56.

[Haa 91]   Haan, S.W.H. de, W.J. de Zeeuw, *Vermogenselektronica* (in Dutch), Eindhoven University of Technology, group EMV: lecture note, 1991.

[Hag 62]   Hague B., *The principles of electromagnetism applied to electrical machines*, New York, Dover Publications, Inc., 1962. Unabridged and unaltered republication of *Electromagnetic problems in electrical engineering*, Oxford University Press, 1929.

[Hee 89]   Heesch, E.J.M. van, A.P.J. van Deursen, M.A. van Houten, G. Jacobs, J. Kersten, P.C.T. van der Laan, "Field tests and response of the D/I H.V. measuring system", *6th Int. Symp. on High Voltage Engineering*, New Orleans, USA, 1989, paper 42.23.

[Hee 95]   Heesch, E.J.M. van, M.H.P. Dagelinckx, F.M. van Gompel, P.P.M. Blom, "Surge corona propagating along a transmission line", *Proc. 9th Int. Symp. on High Voltage Engineering*, Graz, Austria, 1995, paper 2793.

[Hel 90]   Helvoort, M.J.A.M. van, "Ontwerp van een triggering voor een tri-gatron met piëzo-elektrische kristallen" (in Dutch), training report, Eindhoven University of Technology, EH.90.S.226, 1990.

[Hel 91]   Helvoort, M.J.A.M. van, "Gepulste corona" (in Dutch), M.Sc. thesis, Eindhoven University of Technology, EH.91.A.119, 1991.

[Hel 93]   Helvoort, M.J.A.M. van, E.J.M. van Heesch, P.C.T. van der Laan, "Dynamic voltage and current measurements on substation compo-nents", *8th Int. Symp. on High Voltage Engineering*, Yokohama, Japan, 1993, pp.439-442.

[Hel 94a] Helvoort, M.J.A.M. van, A.P.J. van Deursen, P.C.T. van der Laan, "The transfer impedance of metallic cable trays", *EMC'94 Roma*, Rome, Italy, 1994, pp.263-268.

[Hel 94b] Helvoort, M.J.A.M. van, P.C.T. van der Laan, "EMC demonstrations on cabling and wiring", *ISEMC 94*, São Paulo, Brazil, 1994, pp.118-123.

[Hel 95a] Helvoort, M.J.A.M. van, P.R. Bruins, A.P.J. van Deursen, P.C.T. van der Laan, "The non-linear behaviour of steel cable trays for large com-mon mode currents", *11th Int. Symp. on EMC*, Zürich, Switzerland, 1995, pp.531-536.

[Hel 95b] Helvoort, M.J.A.M. van, A.P.J. van Deursen, P.C.T. van der Laan, "The transfer impedance of cables with a nearby return conductor and a non-central inner conductor", *IEEE Trans. on EMC*, Vol. EMC-37, No. 2, 1995, pp.301-306.

[Hel 95c] Helvoort, M.J.A.M. van, P.R. Bruins, E.J.M. van Heesch, P.C.T. van der Laan, "A helical single turn Rogowski-coil with a large aperture for HF current measurement and injection", *Submitted to Review of Scientific Instruments*, 1995.

[Hel 95d]   Helvoort, M.J.A.M. van, "Van de buis naar de goot: EMC-aspekten van kabeldraagsystemen" (in Dutch), *Submitted to Installatiejournaal*, 1995.

[Hoe 88]   Hoeft L.O., J.S. Hofstra, "Measured electromagnetic shielding performance of commonly used cables and connectors", *IEEE Trans. on EMC*, Vol. EMC-30, No. 3, 1988, pp.260-275.

[Hor 94a]   Horck, F.B.M. van, "CM-stromen en DM-spanningen bij de secundaire bekabeling van een 380 kV GIS-installatie t.g.v. schakelhandelingen: Invloed van de kabelloop; metingen en berekeningen" (in Dutch), M.Sc. thesis, Eindhoven University of Technology, EH.94.A.137, 1994.

[Hor 94b]   Horck, F.B.M. van, A.P.J. van Deursen, M.J.A.M. van Helvoort, P.C.T. van der Laan, "Bestrijden van storingen met een juiste techniek van bekabelen" (in Dutch), *Energietechniek*, Vol. 72, No. 10, 1994, pp.591-596.

[Hor 95]   Horck, F.B.M. van, private communication.

[Hou 89]   Houten, M.A., E.J.M. van Heesch, A.P.J. van Deursen, R.G. Noij, J.N.A.M. van Rooy, P.C.T. van der Laan, "General methods for protection of electronics against interference, tested in high-voltage substations", *8th Int. Symp. on EMC*, Zürich, Switzerland, 1989, pp.429-434.

[Hou 90]   Houten, M.A. van, *Electromagnetic compatibility in high-voltage engineering*, Ph.D. thesis Eindhoven University of Technology, 1990.

[IEC]   IEC document 50(551)

[Ima 89]   Iman, R.L., W.J. Conover, *Modern business statistics*, 2nd ed., New York: John Wiley & Sons Ltd., 1989.

[Jil 90]   Jiles, D.C., S. Hariharan, M.K. Devine, "Magnescope: a portable magnetic inspection system for evaluation of steel structures and components", *IEEE Trans. on Magnetics*, Vol. MAG-26, No. 5, 1990, pp.2577-2579.

[Kad 59]   Kaden, H., *Wirbelströme und Schirmung in der Nachrichten Technik*, 2. Auflage (in German), Berlin: Springer, 1959.

[Kei 84]   Keil, A., W.A. Merl, E. Vinaricky, *Elektrische Kontakte und ihre Werkstoffe* (in German), Berlin: Springer, 1984.

[Koe 91]   Koekoek, H.S., private communication, 1991.

[Köh 93]   Köhler, W., T. Dischinger, U. Schärli, "Measurement of fast transients in HV substations and their effects on secondary equipment", *10th Int. Symp. on EMC*, Zürich, Switzerland, 1993, pp.365-370.

[Kos 94]   Kost, A., *Numerische Methoden in der Berechnung elektromagnetischer Felder* (in German), Berlin: Springer, 1994.

[Kup 73]   Küpfmüller, K., *Einführung in die theoretische Elektrotechnik*, 10. Auflage (in German), Berlin: Springer, 1973.

[Laa 86]   Laan, P.C.T. van der, M.A. van Houten, "Design philosopy for ground-
            ing", *5th Int. Symp. on EMC*, York, UK, 1986, p.267.

[Laa 87]   Laan, P.C.T. van der, M.A. van Houten, A.P.J. van Deursen, "Ground-
            ing philosophy", *7th Int. Symp. on EMC*, Zürich, Switzerland, 1987,
            p.567.

[Laa 91]   Laan, P.C.T. van der, E.J.M. van Heesch, *Magnetisch gekoppelde
            ketens* (in Dutch), Eindhoven University of Technology, group EHO:
            lecture note, 1991.

[Laa 93]   Laan, P.C.T. van der, M.J.A.M. van Helvoort, A.P.J. van Deursen,
            M.A. van Houten, "New developments in grounding structures for the
            protection of micro-electronics", *10th Int. Symp. on EMC*, Zürich,
            Switzerland, 1993, p.127.

[Lag 92]   Lagendijk, N.W.,"Installateur staat aarzelend tegenover gebruik ka-
            belkorven" (in Dutch), *Installatiejournaal*, may, 1992.

[Mac 92a]   Maciel, D., L. Kone, B. Demoulin, N. Recrosio, F. Morillon, "Evalu-
            ation de l'amplitude des parasites induits sur des câbles de communi-
            cation installés sur des sites de transport et de production d'énergie
            électrique" (in French), *6ème Coll. Int. CEM*, Lyon-Ecully, France,
            1992, pp.8-13.

[Mac 92b]   Maciel, D., Private communication, 1992.

[Mac 93]   Maciel, D., "Etude et modélisation des risques électromagnétiques
            supportés par des câbles de transmission d'informations contenus dans
            des chemins métalliques installés sur des sites industriels" (in French),
            Ph.D. thesis Lille University of Science and Technology, 1993.

[May 91]   Mayergoyz, I.D., *Mathematical models of hysteresis*, New York:
            Springer, 1991.

[MCB 77]   MetaalCompagnie "Brabant" b.v., *Het MCB boek, 6de druk* (in
            Dutch), Eindhoven: Metaalcompagnie "Brabant" b.v., 1977.

[Mer 70]   Merewether, D.E., "Analysis of the shielding characteristic of sat-
            urable ferromagnetic cable shields" and "Design of shielded cables
            using saturable ferromagnetic materials", *IEEE Trans. on EMC*, Vol.
            EMC-12, No. 3, 1970, pp.134-137 and pp.138-141.

[Oersted]   "Oersted, eddy current solver", *Integrated Engineering Software inc.*,
            46-1313 Border Place, Winnipeg, Manitoba, Canada, tel. (204) 652-
            5636, fax. (204) 633-7780, 1992-1995.

[Pig 90]   F. Pigler, *EMV und Blitzschutz leittechnische Anlagen* (in German),
            Berlin, München: Siemens-Aktiengesellschaft, 1990.

[Poy 00]   Poynting J., "On the transfer of energy in the electromagnetic field",
            Phil. Trans., Part II, p.343.

[Ram 84]   Ramo S., J.R. Whinnery, T. Van Duzer, *Fields and waves in commu-
            nications electronics*, New York: John Wiley & Sons, 2nd ed., 1984.

[Riq 92]   Riquel, G., "Etude du rayonnement électromagnetique émis par les postes sous enveloppe métallique lors de la manoeuvre des sectionneurs" (in french), *6ème Coll. Int. CEM*, Lyon-Ecull, France, 1992, pp.2-7.

[Roz 94]   Rozenboom, J., "De netstroom van elektronische apparaten" (in Dutch), *Energietechniek*, Vol. 72, No. 3, March 1994, pp.159-163.

[Sal 93]   Sali, S., "A circuit-based approach for crosstalk between coaxial cables with optimum braids", *IEEE Trans. on EMC*, Vol. EMC-35, No. 2, 1993, pp.300-311.

[Sch 34]   Schelkunoff, S.A., "The electromagnetic theory of coaxial transmission lines and cylindrical sheets", *Bell Syst. Tech.*, J.13, 1934, pp.532-579.

[Sch 92]   Scheltinga, L., P.T.M. Vaessen, "Digital measurement system for high-voltage impulse tests on transformers", *European Transactions on Electrical Power Engineering*, Vol. 2, 1992, pp.111-116.

[Slu 95]   Sluijpers, W.H.A., "De stroomverdeling over een GIS mantel en de invloed van EMC maatregelen toegepast op een secundaire bekabeling: Stroom- en spanningsmetingen" (in Dutch), training report, Eindhoven University of Technology, EH.95.S.316, 1995.

[Sme 93]   Smeets, R.P.P., R.C.M. Kardos, J.P. van Oostveen, R.C.G. Dirven, H.Q. Li, E. Kaneko, "Essential parameters of vacuum interrupter and circuit related to the occurence of virtual current chopping in motor circuits", *IVth IEEE Japan Power & Energy Soc. Meeting*, Sapporo, Japan, July 1993.

[Sta 91]   Stark, J.W.B., "Staalconstructies 1" (in Dutch), lecture note, Department of Architecture, Eindhoven University of Technology, 1991.

[Str 26]   Strütt, M. "Das magnetische Feld eines rechteckigen, von Gleichstrom durchflossenen Leiters" (in German), *Archiv für Elektrotechnik*, 17, 1926, pp.533-535, and 18, 1927, p.282.

[Str 27]   Strütt, M. "Das magnetische Feld im Innern ferromagnetischer Leiter von rechteckigem, dreieckigem und elliptischem Querschnitt" (in German), *Archiv für Elektrotechnik*, 18, 1927, pp.190-194.

[Str 41]   Stratton, J.A., *Electromagnetic Theory*, New York, London, McGraw-Hill, Inc., 1941.

[Tay 75]   Taylor, J.R., "The screening performance of electrical trunking and conduit" (not for publication), *Atomic Energy Establishment, Winfrith*, AEEW - R 1013, Dorchester, Dorset, UK, 1975.

[Tho 00]   Thomson J.J., *Notes on recent researches in electricity and magnetism, intended as a sequel to professor Clerk-Maxwell's treatise on electricity and magnetism*, Oxford: Clarendon Press, 1893.
           Also published as facsimile-edition; London: Dowsons of Pall Mall, 1968.

[Tho 94]   Thomas, D.E., C.M. Wiggins, T.M. Salas, F.S. Nickel, S.E. Wright, "Induced transients in substation cables: measurements and models", *IEEE-PES winter meeting*, 94WM 143-8 PWRD, New York, USA, 1994, pp.1-7.

[Tin 93]   Tinnemans, P.A.J., "Gedrag van een éénwinding-Rogowskispoel" (in Dutch), training report Eindhoven University of Technology, EH.93.S.301, 1993.

[Tyn 76]   Tyni, M., "The transfer impedance of coaxial cables with braided outer conductors", *Electromagnetic compatibility*, Scientific papers of the institute of telecommunication and acoustics of Wroclaw Technical University, Wroclaw, Poland, 1976, pp.410-419.

[Van 75]   Vance, E.F., "Shielding effectiveness of braided-wire shields", *IEEE Trans. on EMC*, Vol. EMC-17, No. 2, 1975, pp.71-77.

[Van 78]   Vance, E.F., *Coupling to shielded cables*, New York: John Wiley & Sons, Inc., 1978.

[Van 93]   Vandenboorn, R.P.J.M., "Storingen op secundaire bekabeling t.g.v. schakelhandelingen in GIS: Stroom- en spanningsmeting" (in Dutch), M.Sc. thesis, Eindhoven University of Technology, EH.93.A.130

[Wet 90]   Wetzer, J.M., M.A. van Houten, P.C.T. van der Laan, "Preventions of breakdown due to overvoltages accross interruptions of GIS enclosures", *6th Int. Symp. on Gaseous Dielectrics*, Knoxville, USA, 1990, paper 77, pp.531-537.

[Wig 94]   Wiggins, C.M., D.E. Thomas, F.S. Nickel, S.E. Wright, "Transient electromagnetic interference in substations", *Presented at the IEEE/PES 1994 winter meeting (in print)*, New York, USA, 1994.

[Wis 31]   Wise, W.H., "Effect of ground permeability on ground return conductors", *Bell Syst. Techn. Journal*, Vol. 10, 1931, pp.472-484.

[Wou 95]   Wouters, P.A.A.F., M.J.A.M. van Helvoort, P.R. Bruins, "Fasehoekdetectie aan een 50/60 Hz 3-fasen hoogspanningssysteem" (in Dutch), *Internal report*, 95059, 1995.

Appendix A

Magnetic field penetration through tubular shields

A.1 Line-multipole expansion

Kaden describes the penetration of the magnetic field in a solid bar in a 2D-calculation [Kad 59, p.44]. The field originates from a thin line current parallel to the bar. We extend the calculation and replace the bar by a thin walled tube. The results of these calculations are used in Chapter 3 ($\mu_r = 1$) and in Chapter 5 ($\mu_r \neq 1$).

The geometry is shown in Fig. A.1, which is an adapted version of Fig. 34 in [Kad 59]. A current I in the positive z-direction is assumed through the wire at $(x, y) = (-2a, 0)$ near a tube around $(x, y) = (0, 0)$. The tube inner and outer radius are r_0 and r_1, the wall thickness is $d = r_1 - r_0$ and $d \ll r_0$. First no net current is assumed to flow in the tube. At the tube center line at $(x, y) = (0, 0)$ the magnetic field H_a due to the current I in the absence of the cylinder is in the positive y-direction; the magnitude is $H_a = I/(4\pi a)$. Outside the tube the incident H-field may be derived from the real part ψ_i of a complex scalar magnetic potential on the complex $(x + jy)$-plane ($\vec{H} = \nabla \psi_i$):

$$\psi_i(x + jy) = -\text{Re}\left\{ \frac{jI}{4\pi a} \ln(x + jy + 2a) \right\} \tag{A.1}$$

A Taylor-series of the logarithm around $x + jy = 0$ results in a line-multipole expansion of this part of $\vec{H}$. The current distribution induced in the tube by I adds a reaction H-field. According to Kaden the complete outside field contributions can be written as [Kad 59, Eq. B91]:

$$H_r = H_a \sum_{m=1}^{\infty} \left(\frac{-1}{2a}\right)^{m-1} [r^{m-1} - \frac{r_1^{2m}}{r^{m+1}} W_m] \sin(m\phi) \tag{A.2}$$

$$H_\phi = H_a \sum_{m=1}^{\infty} \left(\frac{-1}{2a}\right)^{m-1} [r^{m-1} + \frac{r_1^{2m}}{r^{m+1}} W_m] \cos(m\phi) \tag{A.3}$$
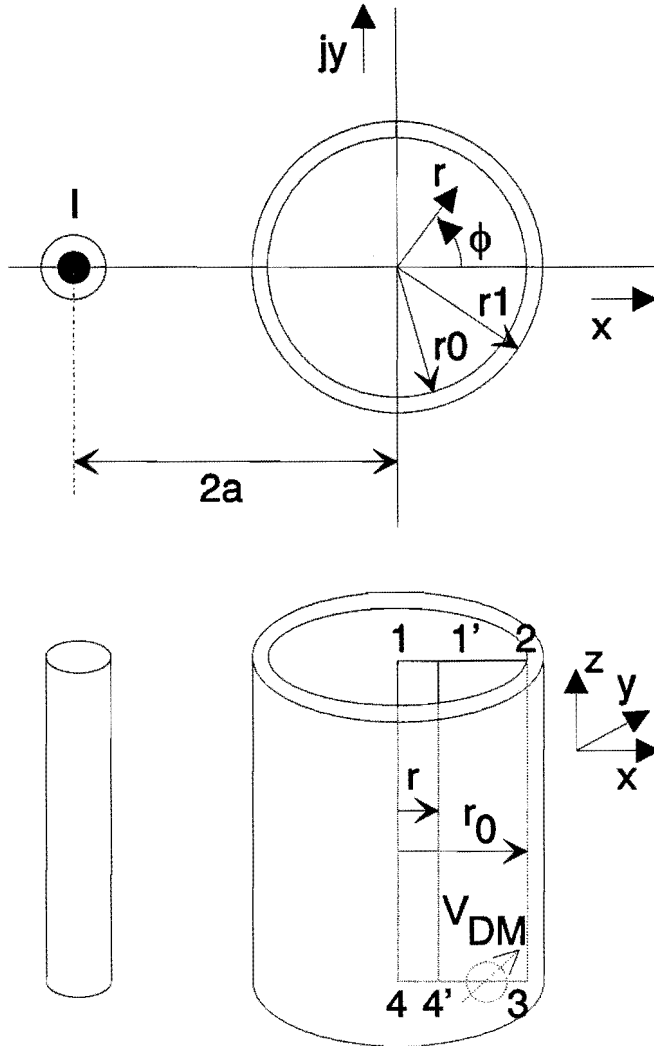
Fig. A.1: Top and side view of the tube with the wire at the distance 2a from the tube axis. The current I through the wire flows in the positive z-direction. The coordinate system used for the calculation is indicated. In the lower part some positions 1-4 and 1'-4' are shown for the measuring wire in the experiment (compare with Fig. 2.7a).

in which W_m is a dimensionless factor which describes the amplitude of the reaction multipole field of order m.

Within the thin wall of our tube E_z can be written as a sum of exponentials rather than Bessel-functions:

$$E_z = j\omega\mu_0 r_1 H_a \sum_{m=1}^{\infty} (A_m e^{kr} + B_m e^{-kr}) \cos(m\phi). \tag{A.4}$$

in which $k = (1+j)/\delta$, the skin depth $\delta = \sqrt{2/\omega\mu\sigma}$, σ is the conductivity of the tube material and $\mu = \mu_0 \mu_r$ the permeability. The corresponding magnetic field within the tube wall is obtained via Maxwell's equation $-j\omega\mu\vec{H} = \nabla \times \vec{E}$:

$$H_r = \frac{H_a r_1}{\mu_r r} \sum_{m=1}^{\infty} m(A_m e^{kr} + B_m e^{-kr}) \sin(m\phi) \tag{A.5}$$

$$H_\phi = \frac{H_a k r_1}{\mu_r} \sum_{m=1}^{\infty} (A_m e^{kr} - B_m e^{-kr}) \cos(m\phi) \tag{A.6}$$

Inside the tube the magnetic field can again be written as a multipole expansion:

$$H_r = H_a \sum_{m=1}^{\infty} \left(\frac{r}{-2a}\right)^{m-1} Q_m \sin(m\phi) \tag{A.7}$$

$$H_\phi = H_a \sum_{m=1}^{\infty} \left(\frac{r}{-2a}\right)^{m-1} Q_m \cos(m\phi) \tag{A.8}$$

in which Q_m is an amplitude factor. From the continuity of the tangential component H_ϕ and the normal component μH_r at the tube walls $r = r_0$ and $r = r_1$, one obtains for the coefficients Q_m, W_m, A_m and B_m:

$$Q_m D_m = 4m k_r r_0 \left(\frac{r_1}{r_0}\right)^m \tag{A.9}$$

$$W_m D_m = e^{kd}(k_r r_1 - m)(k_r r_0 + m) - e^{-kd}(k_r r_1 + m)(k_r r_0 - m) \tag{A.10}$$

$$A_m D_m e^{kr_0} = -\frac{4a(k_r r_0 + m)}{r_1} \left(\frac{r_1}{-2a}\right)^m \tag{A.11}$$

$$B_m D_m e^{-kr_0} = -\frac{4a(k_r r_0 - m)}{r_1} \left(\frac{r_1}{-2a}\right)^m \tag{A.12}$$

in which the common factor D_m is given by:

$$D_m = e^{kd}(k_r r_1 + m)(k_r r_0 + m) - e^{-kd}(k_r r_1 - m)(k_r r_0 - m) \tag{A.13}$$

and $k_r = k/\mu_r$. The magnetic flux $\Phi(r', \phi)$ per unit length between the axis and position (r', ϕ), with $r' < r_0$, is given by:

$$\Phi(r', \phi) = \mu_0 \int_0^{r'} H_\phi dr = \mu_0 H_a \sum_{m=1}^{\infty} \frac{-2a}{m} \left(\frac{r'}{-2a}\right)^m Q_m \cos(m\phi) \tag{A.14}$$

This flux (Eq. A.14), if calculated between the axis and a point on the tube wall (now $r' = r_0$), turns out to be related to the E-field (Eq. A.4) on the inner wall surface. For each multipole order m and each ϕ one infers that:

$$j\omega\Phi(r_0, \phi) = E_z(r_0, \phi) \qquad (A.15)$$

In order to compare the calculated fields with the measurements, we consider an inner wire at three positions inside the shield: a) central at $(r, \phi) = (0, 0)$ along the line 1-4 in Fig. A.1, b) against the inside wall (r_0, ϕ), but insulated with respect to the wall, and c) at arbitrary (r, ϕ) in between, e.g. along the line 1'-4'. The wire is always connected to the wall (2) at one end (1 or 1'). The relevant DM voltage V_{DM} is found between the other end of the wire (4 or 4') and the wall (3), see Fig. A.1 (compare with Fig. 2.7a):

$$V_{DM} = -lE_z(r_0, \phi) + j\omega l\{\Phi(r_0, \phi) - \Phi(r, \phi)\} \qquad (A.16)$$

where l is the length of the wire. The term between brackets describes the flux between the wire 1'-4' and the wall. From Eq. A.15 we learn that for the central inner wire the contribution to V_{DM} from $E_z(r_0, \phi)$ is exactly compensated by $j\omega\Phi$; V_{DM} is zero. For the wire against the wall, the term between brackets is zero and $V_{DM} = -lE_z(r_0, \phi)$. For the wire at a general position (r, ϕ), the DM voltage is given by:

$$V_{DM} = -j\omega l\Phi(r, \phi) \qquad (A.17)$$

again because of Eq. A.15.

In the experiment we send a net current I through the tube in the negative z-direction. The corresponding homogeneous E_z must now be included. Therefore at a general position (r, ϕ), we find:

$$\boxed{V_{DM} = lZ_{Kaden}I - j\omega l\Phi(r, \phi)} \qquad (A.18)$$

in which Z_{Kaden} is the Z_t given by Eq. 2.18.

A.2 Coupling through a longitudinal slot

Kaden has calculated the coupling from an outside magnetic field to a coaxial cable with longitudinal slots [Kad 59, p. 216, 302]. Along the same lines we will calculate the transfer impedance of a cable with one thin slot and arbitrary positions of the inner and return conductor. Figure A.2 is an adapted version of Fig. 114 in [Kad 59].

At high frequencies (wall thickness $d >$ skin depth δ) the inside magnetic field, far away from the slot, can be described as if it is generated by a magnetic line
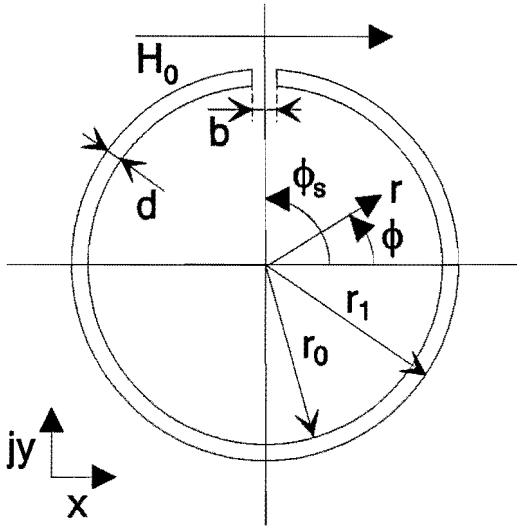
Fig. A.2: Top view of the tube with the longitudinal slot.

dipole in the slot, provided that the field above the slot (H_0) is homogeneous and is perpendicular to the slot. In Fig. A.1 the total geometry is shown without the slot; the slot can be at an arbitrary position (r_1, ϕ) in the $(x + jy)$-plane. Now we rotate the $(x + jy)$-plane to a $(u + jv)$-plane such that the position of the slot is $(r_1, \pi/2)$ (in Fig. A.2 both planes coincide). In the $(u + jv)$-plane the cylindrical coordinates are (r, θ). The complex scalar magnetic potential X_s inside the tube on the complex $(u + jv)$-plane then is given by:

$$X_s(u + jv) = \frac{CH_0}{u + j(v - r_0)} \tag{A.19}$$

For a thin slot, with a width b smaller than two times the thickness d of the tube $(b \leq 2d)$, a simple expression for C is [Kad 59]:

$$C = \left(\frac{2b}{\pi}\right)^2 e^{(-\pi d/b - 2)} \left\{ 1 + (1 - j)\frac{\delta}{b}\left(2 + \pi + \pi\frac{d}{b}\right) \right\} \tag{A.20}$$

·The magnetic flux $\Phi_s(r, \theta)$ per unit length between the inner conductor at position (r, θ) and the tube wall can be calculated from the real part ψ_s from X_s:

$$\Phi_s(r, \theta) = \mu_0 \int_{r_0}^{r} \left(\frac{\partial \psi_s}{r'\partial\theta'}\right)_{\theta'=\theta} dr' = \mu_0 CH_0 \frac{r^2 - r_0^2}{2r_0(r_0^2 + r^2 - 2r_0 r \sin(\theta))} \tag{A.21}$$

Now consider the situation with a nearby return wire and without the slot as sketched in section A.1. For high frequencies the reaction factor W_m becomes

equal to 1 (see Eqs. A.10 and A.13):

$$\lim_{\omega \to \infty} W_m = 1 \tag{A.22}$$

and the reaction field can be described by two line currents [Kad 59]. One image current $(-I)$ is located at $(x, y) = (-r_0^2/(2a), 0)$, the other current $(+I)$ is located at $(x, y) = (0, 0)$. The latter however is canceled by the current $(-I)$ through the tube and the total outside field can be described by two line currents. Outside the tube the H-field then can be derived from the real part ψ_o of a complex scalar magnetic potential on the complex $(x + jy)$-plane:

$$\psi_o = \text{Re}\left\{ \frac{jI}{2\pi} \left[\ln(x + \frac{r_1^2}{2a} + jy) - \ln(x + 2a + jy) \right] \right\} \tag{A.23}$$

With $\vec{H} = \nabla \psi_o$ and the substitution of cylindrical coordinates, we find that:

$$H_0(\phi_s) = -H_\phi(r_1, \phi_s) = \frac{I}{2\pi r_1} \frac{4a^2 - r_1^2}{4ar_1 \cos(\phi_s) + 4a^2 + r_1^2} \tag{A.24}$$

For a far away conductor $(2a \to \infty)$ $H_0(\phi_s)$ reduces to $I/(2\pi r_1)$. We can also verify, that, for any a, $H_r(r_1, \phi) = 0$ as prescribed by Eq. A.2 for $W_m = 1$.

Now we take the influence of the slot into account again. Its contribution to the DM voltage can be written as $-j\omega l \Phi_s(r, \theta)$. If we neglect the other contributions to V_{DM}, this can be written as:

$$V_{DM} = j\omega l M_{slot}(r, \theta) I \tag{A.25}$$

We would like to find an expression for M_{slot} as a function of r and ϕ. The $(u + jv)$-plane coincides with the $(x + jy)$-plane, when it is rotated over $\pi - \theta_r$; θ_r is the angle of the return wire in the $(u + jv)$-plane. When the angle of the position of the slot in the $(x + jy)$-plane is taken to be ϕ_s, then θ_r can expressed as $3\pi/2 - \phi_s$, thus $\theta = \phi - \phi_s + \pi/2$. Substitution of θ and $H_0(\phi_s)$ of Eq. A.24 in Eq. A.21 leads to the following expression for $M_{slot}(r, \phi)$:

$$M_{slot}(r, \phi) = \frac{\mu_0 C (4a^2 - r_1^2)(r_0^2 - r^2)}{4\pi r_0 r_1 (4ar_1 \cos(\phi_s) + 4a^2 + r_1^2)(-2r_0 r \cos(\phi - \phi_s) + r_0^2 + r^2)} \tag{A.26}$$

For very high frequencies M_{slot} approaches an asymptotic value, which is independent of the material parameters; the factor C is then:

$$\lim_{\delta \to 0} C = \left(\frac{2b}{\pi}\right)^2 e^{(-\pi d/b - 2)} \tag{A.27}$$

The total DM voltage between an inner conductor at position (r, ϕ) and the tube wall is given by the combination of Eqs. A.18 and A.25:

$$V_{DM} = lZ_{Kaden}I - j\omega l\Phi(r, \phi) + j\omega l M_{slot}(r, \phi) I \qquad (A.28)$$

The first term in this equation is the regular transfer impedance for a closed tubular shield (Eq. 2.18). The second term is an induction term, which takes into account the nearby return conductor. The third term is the leaking of the magnetic field through the slot; it also takes into account the position of the return wire with reference to the slot.

These results are used in Chapter 3 for the case $\mu_r = 1$. In Chapter 5, where μ_r is large, the above given calculations are only valid at very high frequencies $(\delta \ll d)$.

Appendix B

Derivation of analytic expressions for cable trays

B.1 DC approximation for non-magnetic metals

At low frequencies the current distribution in a tray is homogeneous. For non-magnetic trays ($\mu_r = 1$) the magnetic field then can be calculated with a superposition of the vector potential ($\vec{B} = \nabla \times \vec{A}$) contributions from an infinite number of line currents i [Str 26, Bin 92]. If an infinitely long tray is considered over which a current in the z-direction is flowing the problem to be solved reduces to two dimensions; $\vec{A}$ has only a z-component. For each line current i we obtain:

$$A_z = \frac{\mu_0}{2\pi} i \ln(r) \tag{B.1}$$

We can further simplify our calculations, because the trays we consider are thin compared to their width (see Chapters 4 and 5), so the current through the tray can be approximated by a sheet current. With a total current I through the tray the small line current dI through a narrow strip with width dx' (or dy', see Fig. B.1)
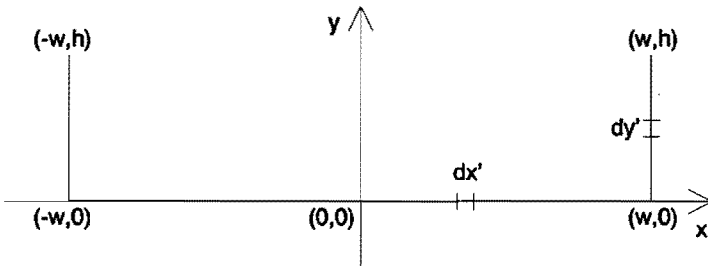

Fig. B.1: *Definition of the geometrical parameters of interest for the calculation of the magnetic field inside a cable tray.*

is:

$$dI = \begin{cases} \dfrac{I}{2(h+w)} \, dx' & \text{in the bottom} \\ \dfrac{I}{2(h+w)} \, dy' & \text{in the side walls} \end{cases} \tag{B.2}$$

With the geometrical parameters given in Fig. B.1, the vector potential in point (x, y) then can be calculated:

$$
\begin{aligned}
A_z(x, y) \;=\; & \frac{\mu_0 I}{8\pi(h+w)} \left\{ \int_{-w}^{w} \ln((x'-x)^2 + y^2) \, dx' \right. \\
& + \int_{0}^{h} \ln((-w-x)^2 + (y'-y)^2) \, dy' \\
& \left. + \int_{0}^{h} \ln((w-x)^2 + (y'-y)^2) \, dy' \right\}
\end{aligned}
\tag{B.3}
$$

The integrals in this equation can be found in standard integral tables or can be solved analytically by an algebraic computer program. The magnetic field can be derived from A_z. For the x-component we find:

$$
\begin{aligned}
H_x(x, y) \;=\; & \frac{1}{\mu_0} \frac{\partial A_z}{\partial y} = \frac{I}{8\pi(h+w)} \left\{ 2 \arctan\left(\frac{x+w}{y} \right) \right. \\
& - 2 \arctan\left(\frac{x-w}{y} \right) \\
& - \ln\left(\frac{(x+w)^2 + (y-h)^2}{(x+w)^2 + y^2} \right) \\
& \left. - \ln\left(\frac{(x-w)^2 + (y-h)^2}{(x-w)^2 + y^2} \right) \right\}
\end{aligned}
\tag{B.4}
$$

To calculate the H_x-field at $(0,0)$, just above the metal, we substitute $x = 0$ and calculate $\lim_{y \downarrow 0} H_x$:

$$H_x(0,0) = \frac{I}{4(h+w)} + \frac{I}{4\pi(h+w)} \ln\left(\frac{w^2}{w^2 + h^2} \right) \tag{B.5}$$

The flux through a loop formed by a conductor above the central line of the tray at a height Δy is given by:

$$\Phi = \mu_0 \lim_{a \downarrow 0} \int_{a}^{\Delta y} H_x(0, y') \, dy' \approx \mu_0 H_x(0,0) \Delta y \tag{B.6}$$

For trays with $h/w \leq 2$ the latter approximation is valid to within 10 % for $\Delta y \leq (h+w)/10$.

B.2 High-frequency approximation

B.2.1 Magnetic field

At high frequencies ($\delta \ll d$) it is sufficient to assume surface currents; the magnetic field outside metallic regions then can be calculated by solving a scalar Laplace equation:

$$\nabla^2 \psi = \frac{\partial^2 \psi}{\partial x^2} + \frac{\partial^2 \psi}{\partial y^2} = 0 \qquad \text{(B.7)}$$

with ψ the scalar magnetic potential; $\vec{H} = \nabla \psi$. For the rectangular inner area of a cable tray (Fig. B.1) the solution of this equation can be obtained by a separation of variables. The general solution is [Bin 92, Eq. 3.70]:

$$\psi(x,y) = \sum_{m=1}^{\infty} (c_m \sin(mx) + d_m \cos(mx))(g_m \sinh(my) + h_m \cosh(my)) \qquad \text{(B.8)}$$

The coefficients c_m, d_m, g_m and h_m are determined by imposing the boundary conditions on the edges of the rectangular area. At the floor ($y = 0$) of the tray we have $H_y = 0$, which means $d\psi/dy|_{y=0} = 0$, thus $g_m = 0$. At the side walls ($x = -w, x = w$) of the tray we have $H_x = 0$, which means $d\psi/dx|_{x=-w,w} = 0$, thus $d_m = 0$ and:

$$m = \frac{\pi(2n-1)}{2w} \text{ , with n = 1,2,...} \qquad \text{(B.9)}$$

Equation B.8 then reduces to:

$$\psi(x,y) = \sum_{n=1}^{\infty} C_n \cosh\left(\frac{\pi(2n-1)}{2w}y\right) \sin\left(\frac{\pi(2n-1)}{2w}x\right) \qquad \text{(B.10)}$$

with $C_n = c_m h_m$. Because the boundary condition at the fourth edge ($y = h$) is a priori unknown, it is difficult to determine C_n. In deep trays we may assume, that ψ varies mainly according to the lowest order $n = 1$. For H_x we then find:

$$H_x(x,y) = \frac{\pi C_1}{2w} \cosh\left(\frac{\pi y}{2w}\right) \cos\left(\frac{\pi x}{2w}\right) \qquad \text{(B.11)}$$

In Fig. B.2 we have plotted $H_x(0,y)$ obtained with a BEM calculation for a tray with $h/w = 2$. In the same figure we have plotted Eq. B.11 after substituting $x = 0$ and $\pi C_1/2w = H_x(0,0)$, where $H_x(0,0)$ was obtained with the BEM calculation. Both curves agree well for:

$$y \leq y_c = h - 0.8w \qquad \text{(B.12)}$$

This result is analogous to the solution of the magnetic field penetration through a thin slot in a plate [Kad 59, p.210]. There the edge effects can be neglected, if the thickness (h) of the plate is larger than 0.4 times the width ($2w$) of the slot. This suggests that Eq. B.12 is not limited to the tray with $h/w = 2$, but is valid for all

deep trays ($h \geq 0.8w$), which was confirmed by additional BEM calculations on trays for which we varied h/w between 1 and 3 in steps of $1/4$.

In the example given above we determined the coefficient C_1 from the numerically calculated magnetic field at the floor of the tray, but as Fig. B.2 shows, we could have determined the field at any given point inside the tray where it is known, as long as $y \leq y_c$. In Section 4.2.2 we used this fact to determine the g-factor for very deep trays ($h/w > 3$). For these trays the magnetic field at the floor cannot accurately be calculated by the BEM program. Therefore we numerically calculate the field at $(x, y) = (0, y_c)$, determine C_1 and calculate $H_x(0,0)$ with the aid of Eq. B.11.
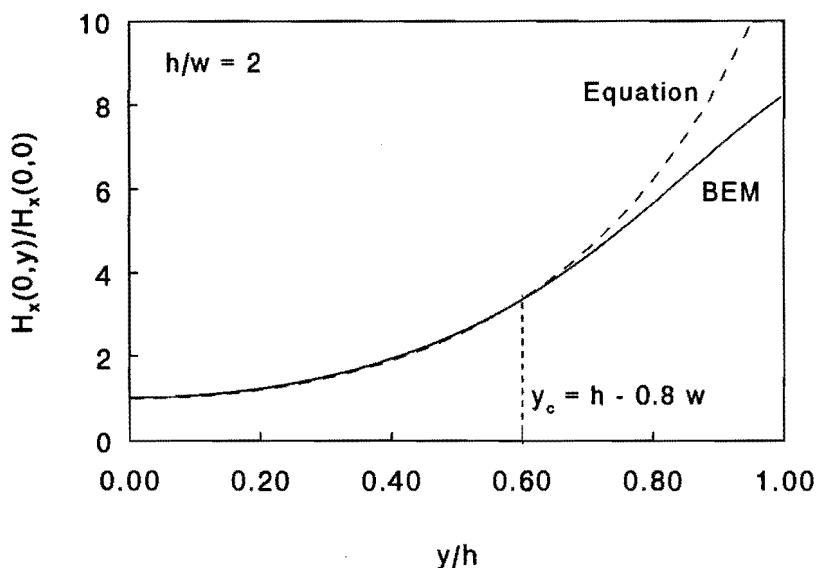

Fig. B.2: Comparison of $H_x(0, y)$, divided by $H_x(0,0)$, found by a BEM calculation at 4.41 MHz and by Eq. B.11 (with $\pi C_1/2w = 1$). Below $y \leq h - 0.8w$ (Eq. B.12) both curves agree very well. This specific tray was identical to the tray in Fig. 4.1.

B.2.2 Current density

In this section we want to explain the dip in J_z observed in Fig. 4.7b for the tray with $h/w = 2$. In the high-frequency approximation the magnetic field is calculated assuming surface currents, which means assuming an ideal conductivity. In a second step we can include finite conductivity and calculate the current density pattern in the center of the tray floor. For this we have to assume that the local interior and exterior H-fields, above and under the tray floor, are not modified by the introduction of the finite conduction; this will be the case for $f > f_2$ (see Fig. 4.1 and Eq. 5.5) and $d > \delta$ or $f > f_3$ (see Fig. 4.1).
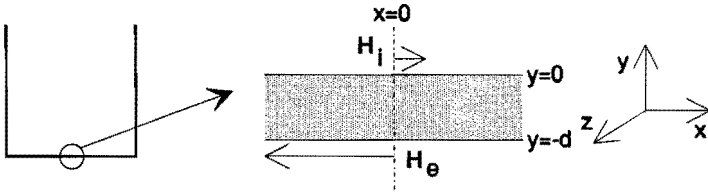
Fig. B.3: The penetration of the interior (H_i) and exterior (H_e) magnetic field into the tray floor at the center is described by the penetration of the field into an infinitely extended plate with thickness d.

For this calculation we replace the tray by a plate, which is extended infinitely in the x- and z-direction and has a finite thickness d (see Fig. B.3). The magnetic fields above and under the plate are in parallel with the plate in the x-direction. The H-field above the plate is taken equal to the interior H-field in the tray at the central line and is labeled H_i. The H-field under the plate is taken equal to the exterior field at the central line of the tray and is labeled H_e. In this case we have to solve a one-dimensional differential equation inside the plate [Kad 59, Eq. A.25]:

$$\frac{d^2 H_x}{dy^2} = k^2 H_x \tag{B.13}$$

with the general solution [Kad 59, Eq. A.26]:

$$H_x(y) = Ae^{ky} + Be^{-ky} \tag{B.14}$$

with k the eddy current constant; $k = (1+j)/\delta$. The factors A and B can be determined from the boundary conditions imposed on both surfaces of the plate:

$$H_x(y = 0) = H_i \tag{B.15}$$
$$H_x(y = -d) = -H_e \tag{B.16}$$

Substitution of the boundary conditions (Eqs. B.15 and B.16) in the differential equation (Eq. B.14) leads, after some straightforward algebraic manipulation, to:

$$A = H_i - B \tag{B.17}$$

$$B = -\frac{H_e - H_i e^{-kd}}{e^{kd} - e^{-kd}} \tag{B.18}$$

Thus inside the plate we have:

$$H_x(y) = \left(H_i + \frac{H_e - H_i e^{-kd}}{e^{kd} - e^{-kd}} \right) e^{ky} - \frac{H_e - H_i e^{-kd}}{e^{kd} - e^{-kd}} e^{-ky} \tag{B.19}$$

The current density in the plate can be obtained from $\nabla \times \vec{H} = \vec{J}$:

$$J_z(y) = (\nabla \times \vec{H})_z = \frac{dH_x}{dy} = k \left\{ \left(H_i + \frac{H_e - H_i e^{-kd}}{e^{kd} - e^{-kd}} \right) e^{ky} + \frac{H_e - H_i e^{-kd}}{e^{kd} - e^{-kd}} e^{-ky} \right\}$$
$$\tag{B.20}$$

The current density at $y = 0$ then is:

$$J_z(0) = kH_i + 2k \left(\frac{H_e - H_i e^{-kd}}{e^{kd} - e^{-kd}} \right) \tag{B.21}$$

For the deep aluminum tray with $h/w = 2$ and $2h + 2w = 0.27$ m we obtained from BEM calculations that, at high frequencies, $H_i = 0.15$ A/m and $H_e = 2.2$ A/m ($I_{CM} = 1$ A). Figure B.4 shows the current density given by Eq. B.21 for $f > f_3$ after substitution of these values. This figure shows very good agreement between Eq. B.21 and the BEM calculations from Fig. 4.1.
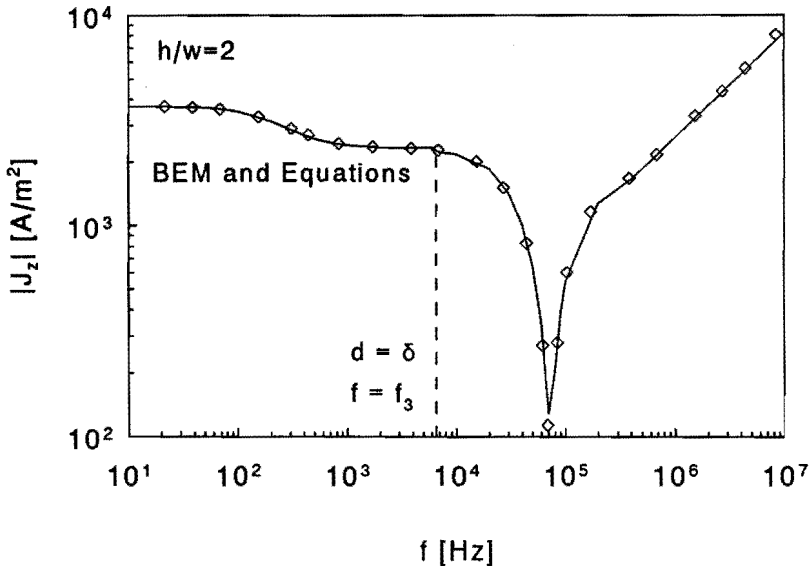
Fig. B.4: *The current density at the central line of the tray floor as function of the frequency. The markers indicate BEM calculations for which the data were obtained from from Fig. 4.1. For $f < f_3$ the solid line is calculated with Eq. 4.18 and above $f > f_3$ with Eq. B.21. Very good agreement between these equations and the BEM calculations is found over the complete frequency range.*

The eddy current constant k increases with frequency and above a certain frequency f_4 the second term of the right-hand side of Eq. B.21 becomes negligible, when compared to the first term: $J_z = kH_x$ (Eqs. 4.8 and 4.20). From Eq. B.21 can be seen easily that the frequency f_4 in principle depends on the shape of the tray, because the ratio of H_e and H_i depends on the height-width ratio of the tray. A practical value for f_4, which can be used when H_e is not known, however seems to be $f_4 = 25f_3$.

B.3   Impedance of the intermediate mode loop

From Section 2.5 we learn that we can describe the overall transfer impedance of a cable in a tray with $Z_{t,total} = Z_{t,cable} Z_{t,tray}/Z_{IM}$. The transfer impedance of the cable and tray can be calculated or measured separately as we have seen in previous chapters. In this appendix we will derive analytic approximations for the impedance of the intermediate loop which can be used for all μ_r.
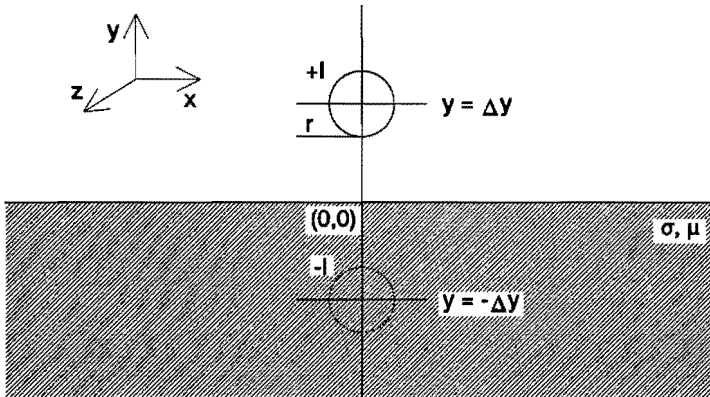

Fig. B.5: Wire above a conducting half space

Let us start with a circular wire in a tray, while both have ideal conduction; this is a good approximation for very high frequencies. When the wire is not too close to the side walls we can replace the tray by a metallic half space (see Fig. B.5). Using the image concept we can calculate the magnetic field ($\vec{H}$) above the half space.

$$
\begin{aligned}
H_x &= \frac{I}{2\pi} \frac{\Delta y - y}{x^2 + (y - \Delta y)^2} U(x^2 + (y - \Delta y)^2 - r^2) \\
&+ \frac{I}{2\pi} \frac{\Delta y + y}{x^2 + (y + \Delta y)^2} && \text{(B.22)} \\
H_y &= \frac{I}{2\pi} \frac{x}{x^2 + (y - \Delta y)^2} U(x^2 + (y - \Delta y)^2 - r^2) \\
&+ \frac{I}{2\pi} \frac{x}{x^2 + (y + \Delta y)^2} && \text{(B.23)}
\end{aligned}
$$

where $U(x^2 + (y - \Delta y)^2 - r^2)$ is Heaviside's step function. The first term on the right hand side is the field caused by the current I through the wire (radius r) at a height $y = \Delta y$ above $x = 0$. The second term is the field caused by the image current $-I$ at $y = -\Delta y$. This image current replaces the actual surface current distribution in the $y = 0$ plane for the calculation of H_x and H_y above that plane. The external self impedance of the intermediate loop, per unit length,

now becomes:

$$L_e = \mu_0 \int\limits_0^{\Delta y} H_x dy = \frac{\mu_0}{2\pi} \ln \left(\frac{2\Delta y}{r} \right) \qquad (B.24)$$

In this appendix we neglect proximity effects in the wire, because we used a braid in our measurements; as we have seen in Section 3.3.3 no eddy currents are induced over the braid. Equation 4.23 gives the expression for L_e when proximity effects are included.

In a second step Kaden takes into account the limited conductivity σ of the half space by assuming that the modification of the magnetic field is very small compared to the field found by assuming infinite conductivity, when the skin depth is small $\delta \ll \Delta y, d$. The electric field at the surface of the half space can be calculated with Eq. 4.8. The integral of the Poynting vector ($\vec{E} \times \vec{H} = E_z H_x$) over the surface of the half space gives the power flowing into the half space per unit length [Poy 00]. From this the internal impedance per unit length Z_i is calculated [Kad 59, p.69]:

$$Z_i = \frac{1+j}{2\pi\delta\sigma\Delta y} \qquad (B.25)$$

When we studied the transfer impedance of a slotted steel tube (Subsection 5.2.2), we already found that the change in the magnetic field is not negligibly small, if a finite conductivity is considered, because of the changed boundary conditions for the normal component of $\vec{H}$. The second step, described above, then cannot be applied. Therefore we will calculate Z_{IM} by following the lines given by Carson [Car 26] and expanded by Wise [Wis 31] for $\mu_r \neq 1$. The image current $-I$, used for Eq. B.24, is now replaced by a distributed current below $y = 0$. The H- and E-field are corrected for the influence of μ_r. For the now dominant TM-mode we start with the electric field inside the metallic half space, symmetric with respect to $x = 0$ (see [Car 26] for details):

$$E_z = - \int_0^\infty F(\alpha) \cos(\alpha x) e^{y\sqrt{\alpha^2+j\omega\mu\sigma}} \, d\alpha \, , \quad \text{for } y < 0 \qquad (B.26)$$

The time dependence $e^{j\omega t}$ is implicitly assumed. From $\nabla \times \vec{E} = -\partial\vec{B}/\partial t$ we find for the magnetic field in the metal:

$$H_x = \frac{1}{j\omega\mu_0\mu_r} \int_0^\infty F(\alpha)\sqrt{\alpha^2 + j\omega\mu\sigma} \cos(\alpha x) e^{y\sqrt{\alpha^2+j\omega\mu\sigma}} \, d\alpha \qquad (B.27)$$

$$H_y = \frac{1}{j\omega\mu_0\mu_r} \int_0^\infty F(\alpha)\alpha \cos(\alpha x) e^{y\sqrt{\alpha^2+j\omega\mu\sigma}} \, d\alpha \qquad (B.28)$$

The magnetic field above the half space ($y \geq 0$) can be split in two contributions. One term $\vec{H}^{(1)}$ is caused by the current through the wire the other $\vec{H}^{(2)}$ by the

current in the metallic half space. The field $\vec{H}^{(2)}$ can be written as a field caused by the (high-frequency) image current in the half space and a correction field to take into account the penetration of the outside field into the half space; we choose to separate both contributions to $\vec{H}^{(2)}$ at the start and not afterwards as Carson does.

The field $\vec{H}^{(1)}$ can be expressed in the same way as Eqs. B.28 and B.28 by writing its components as Fourier integrals, see e.g. [CRC 80, p. A-95, Eqs. 672 and 673]:

$$H_x^{(1)} = \frac{I}{2\pi} \frac{\Delta y - y}{x^2 + (y - \Delta y)^2} = \frac{I}{2\pi} \int_0^\infty \cos(\alpha x) e^{-\alpha(\Delta y - y)} \, d\alpha \qquad \text{(B.29)}$$

$$H_y^{(1)} = \frac{I}{2\pi} \frac{x}{x^2 + (y - \Delta y)^2} = \frac{I}{2\pi} \int_0^\infty \sin(\alpha x) e^{-\alpha(\Delta y - y)} \, d\alpha \qquad \text{(B.30)}$$

These Fourier integrals are valid for:

$$y < \Delta y \qquad \text{(B.31)}$$

The contribution $\vec{H}^{(2)'}$ of the image current to $\vec{H}^{(2)}$ can be written in a similar manner:

$$H_x^{(2)'} = \frac{I}{2\pi} \frac{\Delta y + y}{x^2 + (y + \Delta y)^2} = \frac{I}{2\pi} \int_0^\infty \cos(\alpha x) e^{-\alpha(\Delta y + y)} \, d\alpha \qquad \text{(B.32)}$$

$$H_y^{(2)'} = \frac{I}{2\pi} \frac{x}{x^2 + (y + \Delta y)^2} = \frac{I}{2\pi} \int_0^\infty \sin(\alpha x) e^{-\alpha(\Delta y + y)} \, d\alpha \qquad \text{(B.33)}$$

These Fourier integrals are valid for:

$$y > -\Delta y \qquad \text{(B.34)}$$

The correction term $\vec{H}^{(2)''}$ in $\vec{H}^{(2)}$ due to the distributed current also can be expressed as an Fourier integral:

$$H_x^{(2)''} = -\int_0^\infty \phi(\alpha) \cos(\alpha x) e^{-\alpha y} \, d\alpha \qquad \text{(B.35)}$$

$$H_y^{(2)''} = +\int_0^\infty \phi(\alpha) \sin(\alpha x) e^{-\alpha y} \, d\alpha \qquad \text{(B.36)}$$

By enforcing the boundary conditions that μH_y and H_x are continuous on $y = 0$ for every α, we find:

$$F(\alpha) = \frac{I}{\pi} e^{-\alpha \Delta y} \frac{j\omega\mu_0\mu_r}{\sqrt{\alpha^2 + j\omega\mu_0\mu_r\sigma} + \mu_r\alpha} \qquad \text{(B.37)}$$

in correspondence with Eq. 11 given by Carson [Car 26]. For $\phi(\alpha)$ we obtain:

$$\phi(\alpha) = \frac{\alpha}{j\omega\mu_0}F(\alpha) = \frac{I}{\pi}e^{-\alpha\Delta y}\frac{\mu_r\alpha}{\sqrt{\alpha^2 + j\omega\mu_0\mu_r\sigma} + \mu_r\alpha} \tag{B.38}$$

When the contribution of the image current $(e^{-\alpha\Delta y}I/2\pi)$ is added, the above expression is identical to Eq. 12 from Carson. After substitution of Eq. B.37 and $y = 0$ in Eq. B.26 we find for the electric field at the surface of the metallic half space:

$$E_z(x,0) = -\frac{I}{\pi}\int_0^\infty \cos(\alpha x)e^{-\alpha\Delta y}\frac{j\omega\mu_0\mu_r}{\sqrt{\alpha^2 + j\omega\mu_0\mu_r\sigma} + \mu_r\alpha}\,d\alpha \tag{B.39}$$

The impedance, per unit length, of the loop formed by the wire and the metallic half space can be determined from $\oint \vec{E}\cdot d\vec{l}$, as is shown in Section 2.5. When the wire and its connections to the half space are ideally conducting we find:

$$Z_{IM} = \left(E_z(0,0) + j\omega\mu_0\int_0^{\Delta y} H_x(0,y)\,dy\right)/I_{IM} \tag{B.40}$$

which can be written as a combination of an impedance $Z_s = E_z(0,0)/I_{IM}$ and a self inductance $L_e - L_c$, where L_e is the self inductance of the loop, shown in Fig. B.5, with an ideal conducting half space and L_c a correction term, because of the field penetration due to the non-ideal conduction:

$$Z_{IM} = Z_s + j\omega(L_e - L_c) \tag{B.41}$$

The impedance Z_s (or $E_z(0,0)$) is calculated numerically. However in the high-frequency limit, when $\sqrt{j\omega\mu_0\mu_r\sigma} \gg \mu_r\alpha$, we can express it analytically:

$$\lim_{\omega\to\infty} Z_s = \lim_{\omega\to\infty} -\int_0^\infty \frac{e^{-\alpha\Delta y}}{\pi}\frac{j\omega\mu_0\mu_r}{\sqrt{\alpha^2 + j\omega\mu_0\mu_r\sigma} + \mu_r\alpha}\,d\alpha = \frac{1}{\pi\Delta y}\frac{j\omega\mu_0\mu_r}{\sqrt{j\omega\mu_0\mu_r\sigma}} = \frac{1+j}{\pi\delta\sigma\Delta y} \tag{B.42}$$

which is equal to $kH_x(0,0)/\sigma I$ (Eq. 4.8), when $H_x(0,0)$ is obtained from its high-frequency value (Eq. B.22). Note that this is twice the impedance given by Eq. B.25. We continue now by looking at the flux through the loop. The inductance L_e is already given by Eq. B.24. The correction term L_c can be calculated by integrating $H_x^{(2)''}$ (Eq. B.35) between $y = 0$ and $y = \Delta y$ for $x = 0$:

$$L_c = -\frac{\mu_0}{I}\int_0^{\Delta y} H_x^{(2)''}|_{x=0}\,dy = \frac{\mu_0}{\pi}\int_0^\infty e^{-\alpha\Delta y}(1 - e^{-\alpha\Delta y})\frac{\mu_r}{\sqrt{\alpha^2 + j\omega\mu_0\mu_r\sigma} + \mu_r\alpha}\,d\alpha \tag{B.43}$$

For high frequencies we find the following limit for $j\omega L_c$:

$$\lim_{\omega\to\infty} j\omega L_c = \frac{1}{2\pi\Delta y}\frac{j\omega\mu_0\mu_r}{\sqrt{j\omega\mu_0\mu_r\sigma}} = \frac{1+j}{2\pi\delta\sigma\Delta y} = \frac{1}{2}\lim_{\omega\to\infty} Z_s \qquad (B.44)$$

For the correction term $j\omega L_c$ we find in the high-frequency limit that it is exactly half the impedance Z_s. The total loop impedance (still assuming the wire to be ideally conductive) becomes:

$$\boxed{\lim_{\omega\to\infty} Z_{IM} = \frac{1+j}{2\pi\delta\sigma\Delta y} + j\omega L_e} \qquad (B.45)$$

which is the same expression as found by Kaden. The maximum difference over the entire frequency range between the equations of Carson and Kaden is given in Table B.1 for several Δy and μ_r. We see that the difference becomes larger for increasing μ_r and decreasing Δy. When $\mu_r = 1$ the results of Carson and Kaden agree very well for every practical Δy; the simpler approach of Kaden can then be used to calculate Z_{IM}. Figure B.6b clearly shows a large difference for $\Delta y = 2.5$ mm and $\mu_r = 120$. The maximum difference is a factor 2.6. The impedance obtained from Kaden is too large, thus:

$$|Z_i| \geq |Z_s - j\omega L_c| \qquad (B.46)$$

with Z_i given by Eq. B.25. This implies that the cross-over frequency above which Z_{IM} becomes independent of the material parameters can be found from the condition $\omega L_e = |Z_i|$:

$$\omega = \frac{\mu_r}{\mu_0\sigma\Delta y^2 \ln^2(2\Delta y/r)} \qquad (B.47)$$

This cross-over frequency increases linearly with μ_r, which is consistent with the results for Z_t (Eq. 5.5). It is also interesting to note, that $H_x^{(2)\prime\prime}$ is a function of the product $\omega\sigma$, which is consistent with the first scaling law obtained for Z_t on page 73 of this thesis.

Of course we want to compare the expressions for Z_{IM} to values obtained from measurements. We did not measure Z_{IM} directly, because we can easily obtain it from the already measured values of the transfer impedance of the tray of the cable and of the overall transfer impedance:

$$Z_{IM} = Z_{t,cable} Z_{t,tray}/Z_{t,total} \qquad (B.48)$$

For an aluminum and a steel tray with $h/w = 2$ the indirectly measured Z_{IM} is shown in Fig. B.6 (indicated with markers). The impedance found in this manner also includes the impedance of the connection of the tray to the EMC cabinet; we estimate from the length of the interconnection (30 cm) and the length of the tray
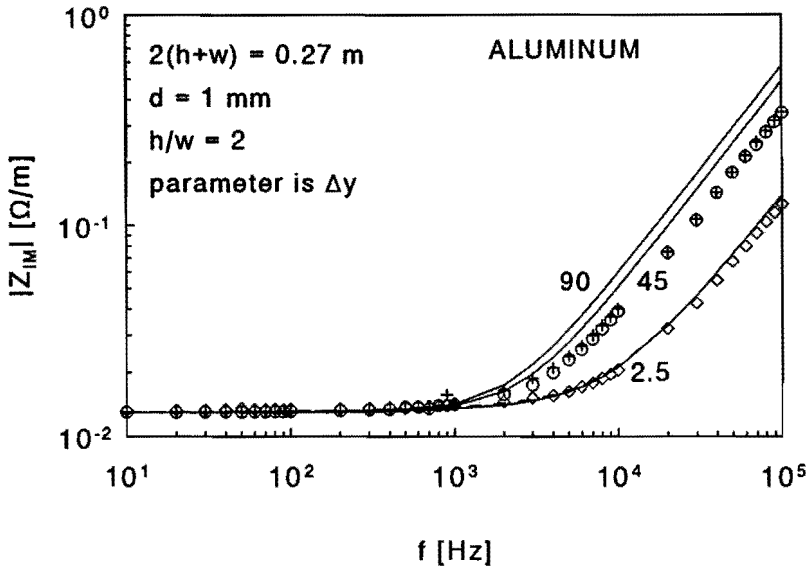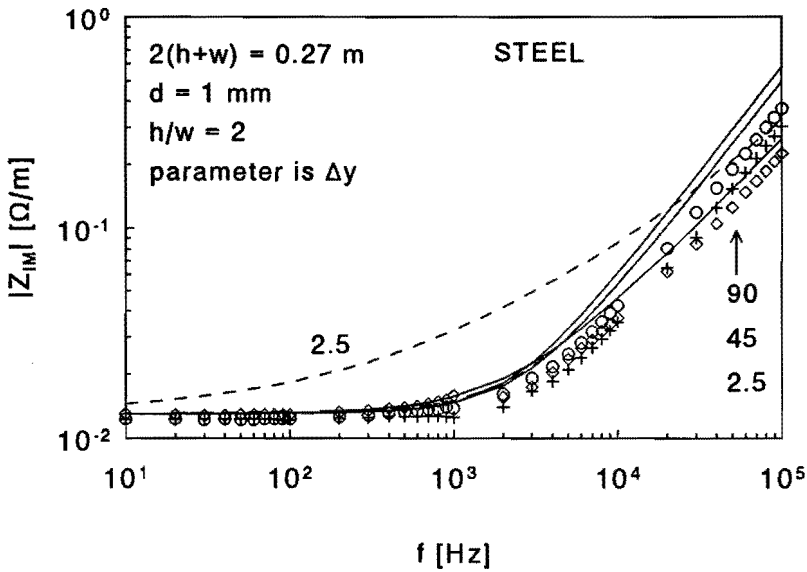
Fig. B.6: The impedance Z_{IM} of the loop formed by the cable screen of an RG-58/U·
cable in an aluminum (a) and steel (b) tray with $h/w = 2$. The height of the cable in
the tray was varied as indicated in the plot. The markers indicate values derived from
measurements (see text); $\diamond$: $\Delta y = 2.5$ mm, $+$: $\Delta y = 45$ mm and $\circ$: $\Delta y = 90$ mm. The
solid lines represent calculations along the lines given by Carson. The dashed lines are
obtained with the Kaden expressions; only the line for $\Delta y = 2.5$ mm in the steel tray
does not coincide with the solid line.

Δy (mm)	max. difference (%)		
	$\mu_r = 1$	$\mu_r = 120$	$\mu_r = 1000$
2.5	6.31	54.31	77.41
5	1.99	34.48	62.23
10	0.58	17.62	42.92
15	0.27	10.69	31.49
20	0.16	7.29	24.12
25	0.10	5.37	19.13
30	0.07	4.13	15.74
35	0.05	3.28	13.22
40	0.04	2.67	11.29
45	0.03	2.22	9.76
90	0.01	0.70	3.75

Table B.1: The maximum difference between calculations of Z_{IM} along the lines given by Carson and given by Kaden for various μ_r and Δy.

(2 m) that Z_{IM} might be 15 % to large. The length of the cable is also 15 % longer than assumed in the calculations.

In the same graph the calculations along the lines of Kaden and Carson are shown. For the aluminum tray (Fig. B.6a) measurement and calculations agree within 11 % for $\Delta y = 2.5$ mm. For the higher positions the difference becomes larger; 29 % for $\Delta y = 45$ mm and 40 % for $\Delta y = 90$ mm. In this case the approximation with the half space is no longer valid, because the inner conductor is too close to the side walls of the tray; Z_{IM} is about the same for both heights. For the tray with $h/w = 1/2$ and $\Delta y = 42.5$ mm the maximum difference is 35 %. For the steel tray (Fig. B.6b) the Carson formulation agrees with the measurements within 30 % for $\Delta y = 2.5$ mm, 68 % for $\Delta y = 45$ mm and 56 % for $\Delta y = 90$ mm. It is interesting to observe that Z_{IM} is of the same order in both steel and aluminum trays and certainly does not differ by a factor $\sqrt{\mu_r}$ as would be obtained from Eq. B.25.

Appendix C

List of symbols

The symbols, which are used in the appendices only, are excluded from this list.

γ :   constant similar to shape factor g

δ :   skin depth; $\sqrt{2/\omega\mu\sigma}$ [m]

Δy :   distance between measurement lead and grounding structure [m]

ϕ :   cylindrical coordinate [rad]

ϕ_s :   angular position of a slot in a tube [rad]

λ :   wavelength [m]

μ :   total permeability; $\mu_0\mu_r$ [H m^{-1}]

μ_0 :   permeability of vacuum; $4\pi \cdot 10^{-7}$ [H m^{-1}]

μ_r :   relative permeability

ξ :   harmonic distortion

ρ :   resistivity [Ω m]

σ :   conductivity [Ω^{-1} m^{-1}]

τ_0, τ_1, τ_2 :   time constants (Eq. 4.15, 4.19 and 4.16) [s]

ω :   angular frequency [s^{-1}]

a :   half of the distance between tube center and return lead [m]

A_n	:	n'th harmonic of a signal, obtained from a discrete Fourier transform
$\vec{B}$	:	magnetic flux density [T]
B_x, B_y, B_z	:	components of $\vec{B}$ [T]
B_r, B_ϕ	:	components of $\vec{B}$ [T]
$c(h/w)$	:	shape factor (Eq. 4.17)
C	:	capacitance [F]
d	:	wall thickness [m]
$\vec{D}$	:	electric flux density [C m^{-2}]
D	:	distance between grounding structure and ground lead [m]
$\vec{E}$	:	electric field strength [V m^{-1}]
E_x, E_y, E_z	:	components of $\vec{E}$ [V m^{-1}]
E_r, E_ϕ	:	components of $\vec{E}$ [V m^{-1}]
E	:	electric field strength at the central line of a tray [V m^{-1}]
f	:	frequency [Hz]
f_0, f_1, f_2, f_3, f_4	:	cross-over frequencies (Fig. 4.1) [Hz]
$g(h/w)$	:	shape factor (Eq. 4.6)
h	:	height of a cable tray [m]
$\vec{H}$	:	magnetic field strength [A m^{-1}]
H_x, H_y, H_z	:	components of $\vec{H}$ [A m^{-1}]
H_r, H_ϕ	:	components of $\vec{H}$ [A m^{-1}]
H	:	magnetic field strength at the central line of a tray [A m^{-1}]
H_{DC}	:	DC magnetic field strength at the central line of a tray [A m^{-1}]
H_{HF}	:	HF magnetic field strength at the central line of a tray [A m^{-1}]
H_0	:	magnetic field strength above a slot [A m^{-1}]
i_1, i_2, i_3, i_g	:	currents through leads (1), (2), (3) and (g) respectively, time domain [A]
i_A, i_B, i_C	:	currents around a GIS (Fig. 7.1) [A]
I	:	current [A]
i_{cm}	:	common mode (CM) current, time domain [A]
I_{CM}	:	common mode (CM) current, frequency domain [A]
i_{dm}	:	differential mode (DM) current, time domain [A]
I_{DM}	:	differential mode (DM) current, frequency domain [A]
i_{im}	:	intermediate mode (IM) current, time domain [A]
I_{IM}	:	intermediate mode (IM) current, frequency domain [A]
$\vec{J}$	:	material current density [A m^{-2}]
J_x, J_y, J_z	:	components of $\vec{J}$ [A m^{-2}]
J	:	current density at the central line of a tray [A m^{-2}]
J_{DC}	:	DC current density at the central line of a tray [A m^{-2}]

$J_{z,s}$	:	axially symmetric current density $[\mathrm{A\,m^{-2}}]$
$J_{z,ind}$	:	induced current density $[\mathrm{A\,m^{-2}}]$
k	:	eddy current constant; $k = (1+j)/\delta$ $[\mathrm{m^{-1}}]$
l	:	length $[\mathrm{m}]$
L_e	:	external part of the self inductance per unit length $[\mathrm{H\,m^{-1}}]$
m	:	index
M	:	mutual inductance; total $[\mathrm{H}]$, or per unit length $[\mathrm{H\,m^{-1}}]$
M_{slot}	:	mutual inductance per unit length, caused by field coupling through a slot $[\mathrm{H\,m^{-1}}]$
n	:	index
O	:	total circumference of a grounding structure $[\mathrm{m}]$
r	:	cylindrical coordinate $[\mathrm{m}]$
r_0, r_1	:	inner and outer radii of a tube $[\mathrm{m}]$
r_1, r_2, r_3, r_g	:	radii of leads $[\mathrm{m}]$
r_w	:	radius of a wire $[\mathrm{m}]$
R_0	:	DC resistance per unit length $[\Omega\,\mathrm{m^{-1}}]$
R_l	:	load resistor $[\Omega]$
S	:	surface area $[\mathrm{m^2}]$
t	:	time $[\mathrm{s}]$
t_r	:	rise time $[\mathrm{s}]$
V_1, V_2	:	voltages in a transmission line description $[\mathrm{V}]$
v_{dm}	:	differential mode (DM) voltage, time domain $[\mathrm{V}]$
V_{dm}	:	differential mode (DM) voltage, frequency domain $[\mathrm{V}]$
v_l	:	voltage over a load $[\mathrm{V}]$
v_s	:	signal source voltage, time domain $[\mathrm{V}]$
w	:	half-width of a cable tray $[\mathrm{m}]$
x	:	Cartesian coordinate $[\mathrm{m}]$
y	:	Cartesian coordinate $[\mathrm{m}]$
y_c	:	critical height of a lead in a tray (Eq. B.12) $[\mathrm{m}]$
$Y_{11}, Y_{12}, Y_{21}, Y_{22}$	:	transmission line parameters $[\Omega^{-1}\,\mathrm{m^{-1}}]$
Y_t	:	transfer admittance; total $[\Omega^{-1}]$, or per unit length $[\Omega^{-1}\,\mathrm{m^{-1}}]$
Y_t'	:	transfer admittance per unit length $[\Omega^{-1}\,\mathrm{m^{-1}}]$
z	:	Cartesian coordinate $[\mathrm{m}]$
$Z_{11}, Z_{12}, Z_{21}, Z_{22}$	:	transmission line parameters $[\Omega\,\mathrm{m^{-1}}]$
Z_0	:	characteristic impedance of a transmission line $[\Omega]$
Z_i	:	internal impedance $[\Omega\,\mathrm{m^{-1}}]$
Z_{IM}	:	impedance of the intermediate mode (IM) loop per unit length $[\Omega\,\mathrm{m^{-1}}]$
Z_s	:	impedance per unit length; E_z/I_{CM} $[\Omega\,\mathrm{m^{-}1}]$
Z_t	:	transfer impedance; total $[\Omega]$, or per unit length $[\Omega\,\mathrm{m^{-1}}]$
Z_t'	:	transfer impedance per unit length $[\Omega\,\mathrm{m^{-1}}]$

$Z_{t,tray}$: transfer impedance of a cable tray; total $[\Omega]$,
              or per unit length $[\Omega\,m^{-1}]$

$Z_{t,cable}$: transfer impedance of a cable; total $[\Omega]$,
              or per unit length $[\Omega\,m^{-1}]$

$Z_{t,total}$: overall transfer impedance of nested grounding structures;
              total $[\Omega]$, or per unit length $[\Omega\,m^{-1}]$

Z_w : internal impedance of a wire per unit length $[\Omega\,m^{-1}]$

Acknowledgement

Curriculum vitae

Mark van Helvoort was born on September 13, 1968 in 's Hertogenbosch. From 1974 to 1980 he went to the primary school "De Wegwijzer" in Den Dungen. The next six years he spent at "Gymnasium Beekvliet" in St. Michielsgestel. In 1986 he started at Eindhoven University of Technology, were he studied electrical engineering for five years and in parallel technology and society for three years. This combination led to a practical training project at the Institute of Control Science in Moscow in 1990. In October 1991 he received his master of science degree in electrical engineering from Prof.dr.ir. P.C.T. van der Laan for a project on pulsed corona. In the same year he started his Ph.D. research on EMC in installations in the High-Voltage and Electromagnetic Compatibility group of Prof.dr.ir. P.C.T. van der Laan, which work led to this thesis. In September 1994 he started Tovary; a small company specialised in import-export with Russia. Since October 1995 he is working as Electromagnetic Technology Modelling Expert at the European Development Centre of AMP inc. in 's Hertogenbosch.

STELLINGEN
behorende bij het proefschrift

GROUNDING STRUCTURES

FOR THE EMC-PROTECTION OF

CABLING AND WIRING

door

M.J.A.M. van Helvoort

29 november 1995

1. The transfer impedance of grounding structures, including cable shields, is not a property of the grounding structure itself, but depends also on the internal and external circuits.

   > This thesis, Chapters 2, 3 and 4.
   > Houten, M.A. van (1990), Stelling IV with the Ph.D. thesis *Electromagnetic compatibility in high-voltage engineering*, Eindhoven University of Technology.

2. The magnetic shielding efficiency of braids is usually zero; this means that a tube with holes is not a correct model to calculate the transfer impedance of a braid.

   > Kaden, H. (1959), *Wirbelströme und Schirmung in der Nachrichtentechnik*, Berlin: Springer, p.307.
   > This thesis, Chapter 3.

3. The transfer impedance of a non-magnetic tray can be described by a simple "engineering" expression. This expression can also be used for shallow steel trays.

   > This thesis, Chapters 4 and 5.

4. From the EMC point of view an airgap in a ferromagnetic grounding structure is worse than in a non-magnetic structure.

   > This thesis, Chapter 5.

5. A helical single-turn Rogowski-coil shows a behavior similar to that of a multi-turn Rogowski-coil. Its bandwidth however is much higher.

   > This thesis, Chapter 7.

6. Although the number of thunderstorm days in the Netherlands is not very large, the number of lightning strikes to our tallest communication tower in Lopik is still large enough to make it interesting to install a lightning measurement system. Such a system is not expensive, if appropriate grounding structures are used.

7. It is hard to believe that C. Baum had Möbius and Euler in mind, when he called his low-frequency grounding topology a Baumkugel.

    Baum, C.E. (1983), *Electromagnetics 3*, Hemisphere Publishing Corporation, pp.145-157: especially the following quotation: "Noting the historical German influence on topology (e.g., well-known connections to Möbius and Euler), let us name such a sub-shield as a: Baumkugel ≡ tree-sphere"

8. Abbot describes in his romance of many dimensions, that Square is lifted out of his two dimensional world and sees his house from above. Unfortunately this perception is not possible, because Square's field of vision is only planar; he will only distinguish dots and lines at the interception line of his field of vision with his own world. He cannot grasp his pentagonal house with one view.

    Abbot, E.A. (1884), *Flatland, a romance of many dimensions*, re-publication, New York: Dover, 1992, Chapter 18.

9. If an institution does not hold to the principle of Wilhelm von Humboldt, "Lehrfreiheit, Lernfreiheit", it should not call itself "University".

    Wilhelm von Humboldt is the founder of the University of Berlin.

10. The small space between the cabinets in the central book storage of our university prohibits an extensive literature search.

11. The combination of a quotation of Goedbloed: "A life free of interference can only be achieved when none of us gives another cause for annoyance and when each of us is tolerant of our fellows." and a quotation of Voltaire: "Et qu'excepte le souper, qui est assez gai, et où il paraît assez d'union, tout le reste du temps se passe en querelles impertinentes." gives some food for thought.

    Goedbloed, J.J. (1992), *Electromagnetic Compatibility*, London: Prentice Hall, p.xiv.
    Voltaire (1759), *Candide*, Paris: Bordas, p.140.

12. A good alternative title for this thesis, reflecting the historical development of grounding structures in our group, is: "From the tube to the gutter".